

Washington University in St. Louis

Washington University Open Scholarship

All Theses and Dissertations (ETDs)

5-24-2012

Whispering Gallery Mode Microresonators for Lasing and Single Nanoparticle Detection

Lina He

Washington University in St. Louis

Follow this and additional works at: <https://openscholarship.wustl.edu/etd>

Recommended Citation

He, Lina, "Whispering Gallery Mode Microresonators for Lasing and Single Nanoparticle Detection" (2012). *All Theses and Dissertations (ETDs)*. 697.
<https://openscholarship.wustl.edu/etd/697>

This Dissertation is brought to you for free and open access by Washington University Open Scholarship. It has been accepted for inclusion in All Theses and Dissertations (ETDs) by an authorized administrator of Washington University Open Scholarship. For more information, please contact digital@wumail.wustl.edu.

WASHINGTON UNIVERSITY IN ST. LOUIS
School of Engineering and Applied Science
Department of Electrical and Systems Engineering

Dissertation Examination Committee:

Lan Yang, Chair
Daren Chen
Arye Nehorai
Barry Spielman
Yinjie Tang
Lihong Wang

Whispering Gallery Mode Microresonators for Lasing and Single Nanoparticle Detection

by

Lina He

A dissertation presented to the Graduate School of Arts and Sciences
of Washington University in partial fulfillment of the
requirements for the degree of

DOCTOR OF PHILOSOPHY

May 2012
Saint Louis, Missouri

copyright by

Lina He

2012

ABSTRACT OF THE DISSERTATION

WHISPERING GALLERY MODE MICRORESONATORS FOR LASING AND
SINGLE NANOPARTICLE DETECTION

by

Lina He

Doctor of Philosophy in Electrical Engineering

Washington University in St. Louis, 2012

Research Advisor: Professor Lan Yang

Whispering gallery mode (WGM) microresonators have attracted great interests due to the significantly enhanced light-matter interactions originating from their high quality factors and small mode volumes. They are suitable for a wide range of applications including sensing, lasing, nonlinear optics, and so forth. However, temperature fluctuations as one of the most common environmental noises disturb the cavity resonances and thus degrade the device stability and sensitivity. We introduce a wetting technique to coat the silica resonator with a thin layer of polymer which has the negative thermo-optic coefficient to compensate for the thermal effect in silica, and demonstrate complete thermal compensation.

WGM microresonators have shown great promise for ultra-sensitive and label-free chemical and biological sensing by probing the surroundings with evanescent waves leaking out of the resonator. Sensing is achieved by monitoring the shift or splitting of a resonant frequency. The detection limit is determined by the linewidth of the resonant mode which is ultimately

limited by material absorption induced loss. To surpass the limit of passive resonators, we report real-time single nanoparticle detection using on-chip WGM microcavity lasers. The ultra-low threshold microlasers are prepared by doping WGM resonators with rare-earth ions through the sol-gel method, and their linewidths are much narrower than the passive counterparts. The detection approach relies on measuring changes in the heterodyne beat note of two split modes originating from splitting of a narrow emission line in the microlaser induced by nanoscale objects. We demonstrate detection of polystyrene and gold nanoparticles as small as 15 nm and 10 nm in radius, respectively, and Influenza A virions by monitoring changes in the beat note of the split lasing modes. The self-heterodyne interferometric method achieved in the on-chip microlaser provides a self-referencing scheme with extraordinary sensitivity, and paves the way for detection and spectroscopy of nano-scale objects using micro/nano lasers.

Acknowledgments

Looking back through my five years' study and work in Dr. Yang's Micro/Nano Photonics Lab at WashU, it has always been a pleasant and fruitful experience which will be a piece of precious treasure not only in my future career but also in my entire life. It has been a long journey and I owe my gratitude to many people for the completion of this dissertation.

First and foremost I would like to thank my advisor Dr. Lan Yang who supports me through my time at WashU. You are the one who turned me from an unrefined student to someone who can define a problem, view it with a top-down perspective, and solve it individually. You are a remarkable mentor who taught me how to view and how to think. By your own action, you defined not only how to do good research but also how to be a good person. I will always envy your attitude to research and life. Thank you for always being there whenever I need advice. I will never forget your wisdom and steady guidance and advices. I appreciate and deeply value all the helps you have ever provided.

The past few years in Yang's Lab have been very stimulating and I am grateful for the numerous discussions with all the current and former members: Dr. Sahin Kaya Ozdemir, Dr. Jiangang Zhu, Woosung Kim, Monifi Faraz, Bo Peng, Zhangdi Huang, Dr. Yunfeng Xiao, Dr. Chunhua Dong, and Venkat Gaddam. I want to especially thank Sahin for his guidance and tremendous discussions in most of my projects. His in-depth analysis and suggestions are always helpful in making my experiment design more solid. Many thanks go to Jiangang for helping me with the experiments. I would like to thank Yunfeng for the theoretical support and fruitful discussions.

I would like to acknowledge Prof. Daren Chen for providing us the aerosol instrument without which many of our exciting experiments would not have been performed. I also want to thank my committee members for reading and correcting my dissertation.

I have had support from many friends during these years. There are far too many to list but some of those that I spent most time with are: Minchao Jin, Yang Lu, Yunfei Shi, Chi Zhang, Yunjing Xu, and Lei Qin. For those friends reading this that are not on the list, you know this is not an attempt to slight you and you know how thankful I am. Thank you for having been there and I really enjoyed the great time we had.

I would like to give my special thanks to Jie Wen. Thank you for your help with the LabVIEW programming and electronics design. Thank you for cheering with me and for sharing my life. It is your love and support make this long journal filled with joyful moments.

Finally, I want to thank my parents. Their love has been limitless since I was a child. They are always doing everything they can to support my own choices unconditionally. Without their love and support, I will be nowhere near the person that I am now.

Lina He

Washington University in St. Louis

May 2012

Contents

Abstract.....	ii
Acknowledgments.....	iv
List of Tables.....	ix
List of Figures.....	x
1 Introduction.....	1
1.1 Background.....	1
1.2 Dissertation Outline.....	2
2 WGM Resonators.....	4
2.1 Introduction.....	4
2.2 Coupling Methods.....	7
2.3 Resonator Measurements.....	8
2.3.1 Q factor and Loss.....	8
2.3.2 Photon Lifetime.....	9
2.3.3 Free Spectral Range.....	10
2.3.4 Mode Volume.....	10
2.4 Coupling Equation.....	11
2.5 Microtoroidal Resonators.....	14
2.5.1 Fabrication.....	15
2.5.2 Mode Distribution.....	16
3 Polymer-Silica Hybrid Resonators.....	17
3.1 Thermal Effect in WGM Resonators.....	17
3.2 Compensation of Thermal Effect.....	19
3.2.1 PDMS Coating.....	20
3.2.2 Theoretical Simulation.....	21
3.2.3 Experimental Results.....	23
3.3 Thermal Oscillation.....	26
3.3.1 Introduction.....	27
3.3.2 Theoretical Model.....	29
3.3.3 Experimental Results.....	32
3.4 Applications of Polymer Coated Resonators.....	39
4 Microcavity Lasers.....	41
4.1 Introduction.....	41
4.2 Er-Doped Microtoroid Lasers.....	42

4.2.1	Sol-gel Fabrication of Er-Doped Silica Microtoroids	43
4.2.2	Laser Characterization	46
4.2.3	Time Domain Laser Operation	47
4.2.4	Maximum Laser Power Output.....	54
4.2.5	Lasing Threshold	55
4.2.6	Upconversion.....	57
4.3	Yb-Doped Microtoroid Lasers.....	57
5	Mode Splitting in Passive Resonators for Nanoparticle Sensing	60
5.1	Introduction of Mode Splitting.....	61
5.1.1	Coupling Equations.....	61
5.1.2	Measurements	64
5.2	Mode Splitting for Single Nanoparticle Detection	66
5.2.1	Single-Particle induced Mode Splitting.....	66
5.2.2	Multiple-Particle induced Mode Splitting	67
5.3	Self-Reference of Mode Splitting.....	70
5.3.1	Temperature Response in Silica Microtoroids	70
5.3.2	Temperature Response in PDMS Coated Microtoroids.....	71
5.4	Detection Limit	75
6	Mode Splitting in Active Resonators.....	77
6.1	Below the Lasing Threshold.....	78
6.1.1	Active Microresonators without Mode Splitting.....	78
6.1.2	Active Microresonators with Mode Splitting	80
6.1.3	Experiments	88
6.2	Above the Lasing Threshold	92
6.2.1	Single-Mode Lasing.....	92
6.2.2	Multi-Mode Lasing.....	95
6.2.3	Influence of Thermal Effect	97
6.2.4	Sensing	99
7	Microlasers for Single Nanoparticle Detection.....	101
7.1	Experimental Setup.....	101
7.1.1	Measurements in Air	102
7.1.2	Measurements in Water	104
7.2	Single Nanoparticle Detection Results.....	105
7.3	Ensemble Measurement of Particle Size.....	108
7.3.1	Theory	108
7.3.2	Experiments	114
7.4	Detection using Multiple-Wavelength Microlasers	118
7.5	Maximum Detectable Particle Number	119
7.6	Sensitivity and Detection Limit.....	121
7.6.1	Effects of the Resonator Size on the Detection Sensitivity	122
7.6.2	Theoretical Detection Limit.....	125
7.6.3	Noise Level	126
7.7	Conclusions and Outlook	129

References	130
Vita	143

List of Tables

Table 3.1	Parameters used in the numerical simulations.	31
Table 5.1	Resonance frequencies and linewidths of the split modes.....	73
Table 6.1	Conditions of optical attenuation, amplification, and lasing for ASM and SM modes.	82

List of Figures

Figure 1.1	Illustration of a Fabry-Perot resonator.	1
Figure 2.1	(a) Ray optics description of light propagation in a microsphere resonator. (b) Field distribution in the equatorial plane of the microsphere. (c) Two-dimensional cross section mode distribution of the fundamental WGM along the radial and polar directions. (d) Field distribution along the radial direction. The red dashed line denotes the microsphere boundary.....	5
Figure 2.2	Illustrations of various resonator geometries: microsphere, microdisk, microtoroid, microring, microcapillary, and microbottle.	6
Figure 2.3	Schemes showing evanescent field coupling of light to a resonator using a prism, fiber taper or integrated waveguide, and angle polished fiber.....	7
Figure 2.4	Schematic of a waveguide coupled WGM resonator.....	11
Figure 2.5	Calculated transmission T_r and buildup factor B versus κ_{ex}/κ_0 for a resonator with $n = 1.45$, $R = 15 \mu\text{m}$, and $Q = 10^8$ at $\lambda = 1550 \text{ nm}$	13
Figure 2.6	Fabrication flow for silica microtoroids on a silicon substrate.	15
Figure 2.7	Top and side view of a fiber taper coupled microtoroid. The major (D) and minor (d) diameters of the microtoroid are marked in the plot.	15
Figure 2.8	Cross section distribution of the electric energy density of WGMs along the radial and polar directions in a silica microtoroid (a) and microsphere (b). The toroid has major and minor diameters of $40 \mu\text{m}$ and $5 \mu\text{m}$, and the sphere has a diameter of $40 \mu\text{m}$	16
Figure 3.1	Transmission spectra during wavelength up scan at different input powers showing thermal drift of the resonant mode in a silica microtoroid. The input light powers marked in the plot have unit of mW. The microtoroid has major (minor) diameter of 32 (5) μm . The Q factor of the measured resonant mode is 3×10^6	19
Figure 3.2	Illustration of PDMS coating on a silica microtoroid by wetting technique. (a) A PDMS droplet on a fiber taper adjacent to a microtoroidal resonator. (b) The resonator is partially wetted by PDMS. (c) Liquid PDMS spreads along the resonator surface forming a thin coating layer. (d) SEM image of a PDMS coated microtoroid.....	20
Figure 3.3	(a) Two-dimensional cross section field distribution of the TE polarized fundamental mode in a PDMS coated silica microtoroid. (b) Normalized field distribution along the radial direction as marked by the white dashed line in (a). The silica microtoroid has major (minor) diameter of 78 (6) μm . The thickness of the PDMS layer is $0.5 \mu\text{m}$ as denoted by the red dashed lines in (b).	21
Figure 3.4	Simulation results showing the light fraction in the PDMS layer η_2 and the total Q factor of the fundamental mode as a function of the PDMS coating thickness t_p . The major and minor diameters of the microtoroid used in the	

	simulation are D (d) = 78 (6) μm . Inset: Two-dimensional field distribution of the resonant mode for $t_p = 0.2, 0.4,$ and $0.6 \mu\text{m}$23
Figure 3.5	Schematics of the experiment setup.24
Figure 3.6	Resonance shift as a function of input optical power for four different WGMs in the same PDMS coated microtoroid ($t_p = 0.31 \mu\text{m}$). The dashed line indicates the curve without thermal effect. Inset: Two resonant modes (black line) during up and down wavelength scan of the pump laser (blue line). It is clearly seen in the transmission spectrum that the high Q mode ($\sim 2 \times 10^6$) shows a resonance red shift (i.e., linewidth broadening occurs in the wavelength up scan), while the low Q mode ($\sim 10^5$) shows a blue shift (i.e., linewidth broadening occurs in the wavelength down scan).25
Figure 3.7	Resonance shift of the fundamental WGM versus input optical power for various PDMS coating thickness. The data is measured near the wavelength of 1550 nm.26
Figure 3.8	Transmission spectra of a resonant mode in a PDMS coated silica microtoroid at input powers of 0.7 mW (a) and 3.1 mW (b). The wavelength scanning speed is 40 nm/s. Insets: Transmission spectra corresponding to the same resonant modes for wavelength up and down scans (blue line: triangle wave from the function generator).....28
Figure 3.9	Thermally induced oscillations in the transmission spectrum of a PDMS coated silica microtoroid. (a) Measured and calculated transmission spectrum. (b) Calculated temperature changes in silica and PDMS. (c) Calculated resonance wavelength λ_s , scanning wavelength λ_p , and the detuning $\Delta\lambda \equiv \lambda_s - \lambda_c$. (d)-(f) Zoom-in plots of (a)-(c) for the first oscillation cycle marked by the dotted oval in (a). The oscillation cycle is divided into four regions (I-IV) marked by different colors. The black dot-dashed line in (f) represents zero detuning.....32
Figure 3.10	Experimental (black solid lines) and numerical simulation (red dashed lines) results of the transmission spectra at input powers of 1.11 mW (a), 1.98 mW (b), 3.15 mW (c), and 4.04 mW (d), respectively. The wavelength scanning speed is 40 nm/s. Insets: Simulation results of scanning wavelength λ_s (orange dashed lines) and resonance wavelength λ_c (green solid lines).36
Figure 3.11	Experimental (black solid lines) and numerical simulation (red dashed lines) results of the transmission spectra for taper-cavity gap of 0.8 μm (a), 0.4 μm (b), 0.2 μm (c), and 0 (d), respectively. The transmission is measured at an input power of 3.91 mW and wavelength scanning speed of 40 nm/s. Insets: Calculated λ_s (orange dashed lines) and λ_c (green solid lines).....37
Figure 3.12	Experimental (black solid lines) and numerical simulation (red dashed lines) results of the transmission spectra at wavelength scanning speed of 40 nm/s (a), 80 nm/s (b), and 120 nm/s (c), respectively. The input power is 3.91 mW. Insets: Calculated λ_s (orange dashed lines) and λ_c (green solid lines).38
Figure 3.13	Power oscillations of the transmitted light with time from a PDMS coated silica microtoroid.39

Figure 4.1	Fabrication flow of Er-doped microtoroids through sol-gel process and photolithography technique. The right two columns show the illustrations and optical micrographs of the microdisk, under-cut microdisk, and microtoroid.	44
Figure 4.2	SEM image of silica sol-gel film coated on a silicon substrate. The coating was repeated three times to obtain the film thickness around 1.5 μm .	45
Figure 4.3	Measured Q factors of Er-doped microtoroids for different dopant concentrations. Inset: SEM image of a doped microtoroid.	45
Figure 4.4	Schematic of experimental setup. PC: polarization controller, OSA: optical spectrum analyzer, WDM: wavelength division multiplexer, PD: photodetector.	46
Figure 4.5	Lasing characterization of an Er-doped microtoroid. (a) Lasing spectrum showing pump at 1445 nm and lasing at 1560 nm. (b) Measurement of laser output versus input pump power. Lasing spectra for 980 nm band pumping showing single-mode (c) and two-mode (d) lasing.	47
Figure 4.6	Laser output in time domain from Er-doped microtoroids. (a) Continuous-wave operation measured from a microlaser with Er^{3+} concentration of $\sim 5 \times 10^{18} \text{ cm}^{-3}$. The laser power fluctuation at frequency 6.7 MHz is attributed to the beating of the split laser modes [104]. (b) SP operation with pulse width ~ 130 ns and pulse repetition rate ~ 680 kHz measured from a microtoroid laser with Er^{3+} concentration of $2 \times 10^{19} \text{ cm}^{-3}$.	48
Figure 4.7	Laser power output at different taper-cavity coupling conditions with the same input pump power. The concentration of Er^{3+} ions is 10^{19} cm^{-3} . (a) For a large taper-cavity gap, continuous-wave lasing is obtained (red curves). When reducing the gap, self-pulsing laser emission occurs (blue curves). (b) Close-up of the laser emission in (a). The laser power fluctuations are due to laser mode splitting.	49
Figure 4.8	(a) Self-pulsing laser operation in the presence of mode splitting in the laser cavity. (b) Close-up of (a) for a single pulse. The pulse is modulated at frequency 62 MHz.	50
Figure 4.9	(a) Transmission spectra of the pump and laser light when the pump wavelength is scanned at a speed of 42 nm/s. The black triangle denotes wavelength up scan and down scan. The broadened resonant mode during wavelength up scan is attributed to thermal effect in the cavity. (b) Zoom-in plot of (a).	50
Figure 4.10	(a) Observed laser pulse train from an Er-doped microtoroid when the pump is fixed at the resonance wavelength. (b) Gaussian fitting (red dashed curve) of a single laser pulse.	51
Figure 4.11	Dependence of pulse repetition time (a) and pulse width (b) on the input pump power. Pump ratio denotes the input pump power normalized by the threshold pump power. Data points and error bars represent the mean and standard deviation of multiple measurements.	53
Figure 4.12	Dependence of pulse period (a) and pulse width (b) on the taper-cavity gap. Blue triangles are cavity loading curve for the pump mode, i.e., pump transmission versus gap. Data points and error bars denote the mean and standard deviation of multiple measurements.	53

Figure 4.13	Laser power output versus taper-cavity gap for continuous-wave (a) and self-pulsing (b) laser operations. The circles denote the laser power output, and the triangles represent the normalized transmission for the pump light. The laser power in (b) is the peak power of the pulses.54	54
Figure 4.14	Simulation results in a microtoroid showing the mode area (a) and the radiation loss induced Q factor (b) versus major diameter of the toroid at minor diameters of 6, 5, and 4 μm56	56
Figure 4.15	Upconversion of Er^{3+} ions. (a) Energy level diagrams of Er^{3+} in silica glass and the associated electron transition processes for generating green upconversion emission under excitation at 980 nm and 1480 nm. (b) Top and side view of green upconversion from an Er-doped silica microtoroid with Er^{3+} concentration of $2 \times 10^{19} \text{ cm}^{-3}$57	57
Figure 4.16	Absorption (solid) and emission (dotted) cross sections of Yb^{3+} in germanosilicate glass [122].58	58
Figure 4.17	Measurement of Q factor from the transmission spectrum of an Yb-doped microtoroid at 965 nm (a) and 1446 nm (b). Red curves are Lorentzian fitting.58	58
Figure 4.18	(a) Typical lasing spectrum of an Yb-doped microtoroid laser. (b) Lasing threshold measurement.59	59
Figure 5.1	Schematic of a waveguide coupled resonator with scatterer induced mode splitting. CW: clockwise, CCW: counter-clockwise, κ_0 : intrinsic resonator loss, κ_{ex} : taper-resonator coupling loss, g : coupling coefficient of CW and CCW modes, and Γ : linewidth broadening due to the scatterer (green circle).62	62
Figure 5.2	Power transmission (red) and reflection (blue) spectra of mode splitting in a passive silica microtoroid at different taper-cavity coupling conditions: (a) experimental measurements and (b) numerical calculations. From top to bottom panels, the taper-cavity gap gradually decreases with a total change of 0.5 μm . Parameters for the simulation in (b) are $\kappa_0 = 1.0 \times 10^8 \text{ Hz}$, $\Gamma = 0.3\kappa_0$, and $g = -1.9\kappa_0$. From top to bottom panels, κ_{ex} equals to $0.16\kappa_0$, $0.35\kappa_0$, $0.65\kappa_0$, $1.2\kappa_0$, $3.0\kappa_0$, $9.0\kappa_0$, and $12.0\kappa_0$, respectively. In (b), the reflection coefficients are multiplied by 3 for visibility.65	65
Figure 5.3	Mode distributions of two SWMs in a microtoroid in response to one single particle (a) and two particles (b) on the resonator surface. Black curves denote the resonator boundary and black dots represent particles.66	66
Figure 5.4	(a) Recorded frequency splitting with time as PS particles of radius 50 nm are deposited on a microtoroid continuously and one by one. (b) Illustration showing the possible shifts of the two split modes with the binding of a PS particle which leads to a decreased frequency splitting.69	69
Figure 5.5	Dependence of mode splitting in a silica microtoroid on environment temperature. (a) Resonance frequency shifts of the split modes as a function of temperature. The red dots and black squares denote the higher-frequency and lower-frequency modes in the transmission spectrum, respectively, as marked in the inset. Inset: Splitting spectrum excited at around 1437.8 nm with doublet splitting of $\sim 40 \text{ MHz}$. (b) Intensity graph of mode splitting spectrum as	

	temperature increases. (c) Transmission spectra measured at different frames. Increasing frame number in (b) and (c) corresponds to increasing time.71	71
Figure 5.6	Field distributions of the symmetric and asymmetric modes with a particle deposited on the PDMS surface (a) and doped inside the PDMS layer (b).72	72
Figure 5.7	(a) Micrographs showing a fiber tip approaching a microtoroid. The right panel indicates a larger tip size interacting with the WGM field. Transmission spectra of WGMs at 1437.8 nm (b) and 1428.2 nm (c) in response to increasing tip size from top to bottom. From Lorentzian fitting, the linewidth of the resonant dip in I of (b) is 80.1 MHz corresponding to a Q of 2.6×10^6 , and the initial frequency splitting in I of (c) is 33.9 MHz.....73	73
Figure 5.8	(a) Intensity graph of the splitting spectrum from a PDMS coated microtoroid. Inset: The WGM is excited at around 1536.5 nm with a frequency splitting of 950 MHz induced by a fiber tip. (b) Transmission spectra at different frames. Histograms of the frequency splitting (c) and linewidths (d) of the doublet modes for spectra in (a).74	74
Figure 6.1	Simulation results showing the transmission spectrum at different gain values ξ . Parameters used for the calculations are: $\lambda_c = 1550$ nm, $\kappa_0 = 4.0 \times 10^7$ Hz ($Q_0 = 3.0 \times 10^7$), and $\kappa_{ex} = 0.7 \kappa_0$ ($Q_{ex} = 4.3 \times 10^7$).79	79
Figure 6.2	Schematic diagram showing mode splitting in a fiber taper coupled active resonator.80	80
Figure 6.3	(a) Calculated power transmission spectra as a function of frequency detuning for various taper-cavity coupling condition κ_{ex} and additional damping rate Γ . Parameters used in the simulation are $\kappa_0 = 4.0 \times 10^7$ Hz, $g = -0.5 \kappa_0$, and $\lambda_c = 1550$ nm. In each plot, transmission spectrum is obtained at different ξ85	85
Figure 6.4	Experimental setup. PD: Photodetector, PC: Polarization controller, OSA: Optical spectrum analyzer, WDM: Wavelength division multiplexer.88	88
Figure 6.5	Transmission spectra of the probe light measured in the under coupling (a) and over coupling (b) regimes with increasing pump power (from top (pump power is 0) to bottom). γ denotes the resonance linewidth. Red dashed lines in (a) are Lorentzian fitting and in (b) are the best fitting in the least-squares sense using the theoretical model in Sec. 6.1.2. (c) Beat note signal from the split lasing modes.89	89
Figure 6.6	Experimental measurements (a) and numerical simulations (b) of the transmission and reflection spectra of mode splitting at different taper-cavity gap. Red curves represent the transmission and blue curves denote the reflection.91	91
Figure 6.7	(a) Typical lasing spectrum of an Er-doped microtoroid. (b) Transmission spectra of the pump and laser light when the pump wavelength is scanned at a speed of 42.4 nm/s. The black triangle denotes pump wavelength up scan and down scan. Power output of the laser emission (c) and the transmitted pump light (d) when the pump wavelength is fixed. Red dashed line in (c) shows a cosine fitting. Transmission spectra of the probe light when the probe wavelength is scanned and the pump laser is turned off (e) and on (f). Red lines	

	in (e) and (f) are Lorentzian fittings. γ : resonance linewidth; δ : doublet splitting.	93
Figure 6.8	(a) Lasing spectrum. (b) Laser power fluctuations in time domain. (c) Evolution of the transmission spectrum of the probe mode as the pump power increases.	95
Figure 6.9	(a) Lasing spectrum. (b) Transmission spectrum of the probe light at the lasing wavelength when the pump laser is off. (c) Laser power output. (d) FFT spectrum of the laser signal in (c). (e-f) Zoom-in of the two resonant modes in (b). (g-h) Transmission spectra of the two resonant modes in (b) when the pump laser is turned on.	96
Figure 6.10	Effects of power P_s (a) and wavelength scanning speed v_s (b) of the probe laser on the mode splitting. In (a), the scan speed is $v_s = 42.4$ nm/s, and in (b), the power is $P_s = 48$ μ W.	98
Figure 6.11	Effects of pump power (a) and taper-cavity gap (b) on FFT spectrum of the beat note signal from the split lasing modes.	99
Figure 6.12	(a) Effect of an intentionally introduced scatterer (fiber tip) on the mode splitting in an active microcavity. Inset: Micrograph showing a fiber tip approaching a microtoroid surface. (b) FFT of the beat note signal at different tip positions (scatterer size).	99
Figure 7.1	Schematic of the experimental setup. The pump light and the split lasing modes are separated using a wavelength division multiplexer (WDM). Split lasing modes are mixed in a photodetector (PD) leading to a heterodyne beat note signal. A nozzle continuously delivers nanoparticles onto the microtoroid laser, which translates changes in polarizability into changes in frequency splitting.	103
Figure 7.2	Illustration showing the detection of nanoparticles using mode splitting in a microcavity laser.	104
Figure 7.3	(a) Recorded real-time beat frequency when gold nanoparticles (radius $R = 50$ nm) are continuously deposited onto a microlaser. Lower panel of (a) shows the frequency difference of the beat note between two consecutive detected data points. Five particle binding events marked with red circles are clearly observed from the discrete jumps. (b) Beat note signals corresponding to each time segment in (a). (c) FFT spectra of the first and second beat notes from top in (b) as marked by black arrows. Obvious shift of the FFT frequency is observed corresponding to the first particle binding event in (a).	105
Figure 7.4	Beat frequency with time in response to the arrival of InfA virions (a) and gold nanoparticles of $R = 100$ nm (c) onto a Er-microlaser continuously. Red circles denote individual particle binding events. The major (minor) diameter of the microtoroid laser is 47 (3.7) μ m for InfA measurement and 47 (4) μ m for Au particle measurement. The SEM images show InfA (b) and gold particles (d) attached on the microlaser surface.	106
Figure 7.5	Recorded beat frequency with time when PS nanoparticles of radius 15 nm (a) and Au nanoparticles of radius 10 nm (b) are deposited on the microlaser surface continuously. Red lines are drawn at mean of the measured beat	

	<p>frequencies for each binding event. The major diameter of the Er-doped microtoroid is 27 μm, and the minor diameter is in the range of 3.5~4 μm. 107</p>
Figure 7.6	<p>Nanoparticle detection in water. (a) Lasing spectrum of an Yb-doped microtoroid laser in water. (b) Changes in beat frequency with time after PS nanoparticle suspension ($R = 30 \text{ nm}$) is injected into the chamber. The major (minor) diameter of the microlaser is 105 (4.5) μm. (c) Top view of the microlaser in water with a particle attached on its ring. The particle becomes visible due to scattering of red light coupled into the microlaser. The white light at the top is due to the illuminating light from the microscope. The white dotted lines are drawn to denote the boundary of the microlaser and the fiber taper. The red arrows show the direction of light propagation in the fiber taper. 107</p>
Figure 7.7	<p>Recorded beat frequency with time when InfA virions are injected into the water chamber. The major (minor) diameter of the microlaser is 100 (8) μm. 108</p>
Figure 7.8	<p>(a) Upper panel: Illustration of a microtoroid and cross-sectional electric field distribution of the fundamental WGM. Lower panel: Normalized distribution of the field magnitude f along resonator surface as a function of the polar angle θ. (b) Simulation results from Eq. (5.45) show the frequency splitting as PS nanoparticles are continuously deposited on the microtoroid. The upper and lower panels are obtained for two sets of simulations with nanoparticles placed at random positions on the resonator. Parameters used in simulations are: PS particles with radius $R = 50 \text{ nm}$ and refractive index $n_p = 1.59$, resonance wavelength $\lambda_c = 1550 \text{ nm}$, surrounding medium with refractive index $n_m = 1.0$, and mode volume $V = 300 \mu\text{m}^3$ 109</p>
Figure 7.9	<p>Recorded frequency splitting with time as gold nanoparticles of radius 30 nm are continuously deposited onto two microtoroid lasers (a) and (b). There are about 200 particles detected in each plot. Insets of (a) and (b) present close-up plots of frequency splitting in a short time period. Axes of the insets are the same as those of the main plots. 110</p>
Figure 7.10	<p>Definition of change in frequency splitting corresponding to a particle binding event. 110</p>
Figure 7.11	<p>Calculated histograms of splitting changes induced by consecutive deposition of PS particles onto a microtoroid. Here $R = 50 \text{ nm}$ in (a) and $N = 200$ in (b). Particle radii labeled in (b) have unit of nanometer. Each histogram corresponds to one set of trial: continuously deposit N particles of radius R on the resonator, record the corresponding changes in frequency splitting, and create the histogram of those changes. Mean and standard deviation of the histograms are listed in the form of mean/deviation with unit of MHz: (a) 0.706/16.795, 0.847/18.243, 0.447/17.407 from top to bottom; (b) 0.242/3.372, 1.091/8.592, 1.659/17.545 from top to bottom. 111</p>
Figure 7.12	<p>Expectations of ΔS^{max} (black triangles) and ΔS^{σ} (blue circles) as a function of R for PS nanoparticles. The number of particle binding events is $N = 200$. The data points and error bars denote the mean and standard deviation of 10000</p>

	times repeated calculations. Red solid curves are polynomial fittings that scale with R^3	112
Figure 7.13	Distributions of ΔS^σ (a) and ΔS^{\max} (b) from 10000 times repeated simulations for PS particle ($R = 50$ nm) deposition with different N . Solid red lines in (a) are Gaussian fittings. (c) Mean (data points) and standard deviation (error bars) of ΔS^{\max} (black triangles) and ΔS^σ (blue circles) as a function of N . The results are obtained from 10000 times repeated simulations.	113
Figure 7.14	Estimating particle size with ensemble measurement. Real time records of beat frequency when Au nanoparticles of radius $R_1 = 15$ nm (a) and $R_2 = 25$ nm (b) are deposited one by one onto a microlaser randomly. Red lines represent mean values of the measured beat frequencies for each binding event. (c) Histograms of the beat frequency changes for two particle sizes. Black solid curves are Gaussian fittings. The total numbers of detected binding events are 397 for R_1 and 419 for R_2 . The mean and standard deviation of the histograms are presented in the plot with unit MHz. (d) Weighted standard deviation μ of splitting changes versus threshold δ for R_1 (red circles) and R_2 (blue stars). Inset: The same curves are plotted after multiplying the x-axis of the curve for R_2 with a correction term $\delta_1/\delta_2 = 0.22$, which is close to the ratio $(R_1/R_2)^3 = 0.23$	115
Figure 7.15	Distribution of size estimation using bootstrap method of 1000 resamples. Red curve is a Gaussian fitting with mean value of 14.97 nm.....	116
Figure 7.16	Size estimation of Au nanoparticles as a function of detected particle number for reference and measured particles. Blue circles and red crosses are the mean and 95% confidence interval of the size estimation obtained from the bootstrap method of 1000 resampling.	117
Figure 7.17	Simultaneous multi-wavelength detection of nanoparticles using a single microlaser. (a) Typical spectrum of a two-mode microtoroid laser. The pump is located at $\lambda_p = 1443$ nm, and the two lasing lines are at $\lambda_{s1} = 1549$ nm and $\lambda_{s2} = 1562$ nm. (b) A typical beat note signal and its FFT spectrum for the two-mode microlaser. The two peaks in the FFT spectrum correspond to frequency splitting of the lasing modes at λ_{s1} and λ_{s2} , separately. (c) Intensity graph of the FFT spectrum when Au particles of $R = 50$ nm are continuously deposited onto the microlaser surface. The side bar denotes magnitude of the FFT spectrum in dB. For the same particle binding events, the heights of discrete changes in the two beat frequencies are different. (d) Close-up of the black rectangle in (c). Red circles mark the particle binding event that is clearly detected by one laser mode, but undetected by the other mode.....	119
Figure 7.18	Calculation results of the frequency splitting $2g$ (a) and linewidth difference 2Γ (b) induced by a single PS nanoparticle as a function of the particle radius for different WGM parameters: mode volume V and field function f . Simulation results of the resonance frequency shift (c) and linewidth broadening (d) of the two split modes as PS particles of radius 30 nm are consecutively deposited on the resonator randomly. Parameters used in the calculations of (c) and (d) are: maximum field $f = 0.3$, $V = 400 \mu\text{m}^3$, and $\lambda_c = 1550$ nm.....	120

Figure 7.19	Dependence of a single PS nanoparticle induced frequency splitting $2g$ on the particle radius R for various values of normalized field maximum f and mode volume V . Simulations are performed at $\lambda_c = 1550$ nm.	121
Figure 7.20	(a) Illustration showing the major (D) and minor (d) diameters of a microtoroid. Simulation results of the maximum field f (b), mode volume V (c), and splitting coefficient (d) as a function of D for $d = 6, 5, 4,$ and 3 μm . The plots are for TE-polarized fundamental WGM. Splitting coefficient in (d) is defined as $f^2 \omega_i / V$ for $\lambda_c = 1550$ nm. The data legends in (c) and (d) are the same as those in (b).	123
Figure 7.21	Field distributions of TE-polarized fundamental resonant modes in microtoroids of different major and minor diameters. Size of the microtoroid is denoted in a pair of parentheses as (major diameter, minor diameter) with unit of micrometer. (a)-(e) depict the results for different major diameters and the same minor diameter. (f)-(j) show the distributions for the same major diameter and different minor diameters. (a)-(c) and (f)-(h) present the cross-sectional field distributions. (d) and (i) present the normalized field distribution along the outer boundary of the microtoroid. (e) and (j) show the normalized field distribution along the radial direction as marked by the red dotted line in the horizontal direction in (a). In (e) and (j), the point $x = 0$ represents the boundary of the microtoroid.	124
Figure 7.22	Histograms of measured discrete changes in the laser beat frequency as PS nanoparticles of $R = 50$ nm are deposited on Er-doped microtoroids of diameters 42 μm (a) and 30 μm (b). The total number of detected particles is 40 in (a) and 21 in (b). Red solid lines are Gaussian fittings. Mean and standard deviation of the histograms are shown in each plot with unit MHz.	125
Figure 7.23	Simulation results of a single PS nanoparticle induced frequency splitting as a function of the particle radius R for different f and V at $\lambda_c = 1550$ nm.	126
Figure 7.24	(a) Beat frequency fluctuation in air: noise is within ± 100 kHz. This noise level sets the limit for the smallest detectable particle size in our experiments. (b) Histogram showing the beat frequency distribution. The histogram is constructed from a total of 7000 measurement points. Red solid line is a Gaussian fitting with mean 5.06 MHz and standard deviation 25 kHz.	127
Figure 7.25	(a) Beat frequency fluctuation in water: noise is within ± 4 MHz. (b) Histogram showing the distribution of the beat frequency noise. The histogram is constructed from a total of 621 measurement points. Red solid line is a Gaussian fitting with mean 5.3 kHz and standard deviation 1.2 MHz.	128
Figure 7.26	Recorded beat frequency with time when PS particles of $R = 100$ nm are injected into the water chamber.	128

Chapter 1

Introduction

1.1 Background

Optical resonators play an important role in modern optics. They are generally used for laser devices, optical filtering, nonlinear optics, etc [1-3]. A conventional optical cavity or resonator consists of two or more mirrors arranged in such a way that light bounces back and forth in a closed path for multiple times (Figure 1.1). When the round trip optical path length is equal to an integer number of the light wavelength, constructive interference of light takes place inside the cavity, enabling light reinforcement and confinement in a small space for a long time. This is known as resonant condition, which is related to the resonator geometry and dielectric properties.

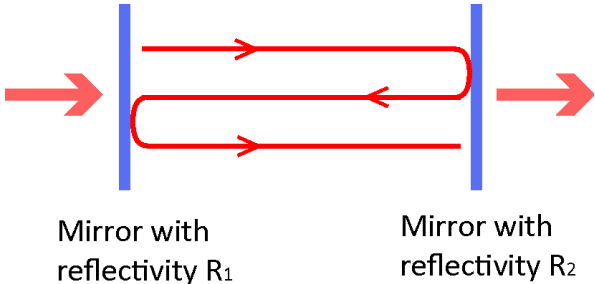


Figure 1.1 Illustration of a Fabry-Perot resonator.

In order to achieve high light intensity in a cavity, one needs to decrease the cavity size allowing strong light confinement and to increase the reflectivity of the mirrors reducing optical losses. Achieving these requirements is technically challenging and expensive for mirror based cavity constructions. In addition, mirror based cavities suffer from the alignment and stability issues. Most of those problems can be overcome by a particular class of monolithic dielectric resonators with circular shapes, referred to as whispering

gallery mode (WGM) resonators. In these resonators, light propagates along the resonator-surrounding interface via total internal reflection (TIR) with the guided modes known as whispering gallery modes. Due to their easy fabrications, miniature structures, and small losses, WGM resonators have attracted intense interests in the past two decades, and have found applications in a wide range of areas such as optical sensing, lasing, nonlinear optics, and optical communications [4-8].

This dissertation will study the microtoroidal resonators and their applications in single-mode lasing and sensing. Polymer coating on the resonator surface can be used not only to control the thermal effect in the resonator, but also to conduct versatile sensing mechanisms. WGM microcavity lasers are proposed as sensing elements to detect and size single nanoparticles and viruses, giving rise to improved detection limit due to their ultra-narrow spectral widths.

1.2 Dissertation Outline

In chapter 2, the basic theory and characteristics of microresonators are introduced. Different resonator geometries and materials are reviewed. Coupling equations are introduced to describe the waveguide coupled resonator system, which is important to study the transmission properties of the resonator. This dissertation focuses on the study of silica microtoroidal resonators because of their unique advantages over other types of resonators. The fabrication of microtoroids and their mode distributions are described in chapter 2.

Chapter 3 investigates the properties of polymer-silica hybrid resonators. Thermal effect in a silica microtoroid is eliminated by coating the toroid with a thin layer of PDMS through wetting technique. Transmission oscillation in such hybrid resonators is observed as a result of the competition between the thermal effects in silica and PDMS. A detailed theoretical and experimental analysis is presented to explain the observed phenomena.

Chapter 4 introduces the preparation of sol-gel silica thin films, based on which active microtoroids are fabricated. Laser emission from the active resonator is characterized. Time domain laser operation, maximum laser power output, lasing threshold, and upconversion in the microtoroidal lasers are discussed in detail.

Chapter 5 reviews the basic principle of mode splitting in a passive microresonator, and introduces its application in single nanoparticle detection. A theoretical model is described to characterize the multiple-particle induced mode splitting. Self-referencing property is demonstrated experimentally by studying the temperature response of mode splitting in silica microtoroids and PDMS coated silica microtoroids.

Chapter 6 studies mode splitting in active microresonators operated below and above the lasing threshold. Mode splitting spectrum, i.e., various transmission profiles, in an active resonator below the lasing threshold are analyzed theoretically and experimentally. Mode splitting in microcavity lasers manifests itself as a beat note signal of the split lasing modes, which can be detected from the laser power output and be used to monitor the mode splitting with ultra-high sensitivity.

Chapter 7 provides the results of label-free single nanoparticle detection using mode splitting in microcavity lasers. Ensemble measurements are explained to estimate the size of nanoparticles. The maximum detectable particle number, sensitivity, and detection limit are analyzed in detail. Using mode splitting in a microlaser, the nanoparticle detection limit is significantly improved without increasing the system complexity.

Chapter 2

WGM Resonators

Due to the reduced reflection losses and the possible low material absorption, WGM resonators have exceptionally high quality (Q) factors, leading to high light energy, narrow resonance linewidth, and long photon lifetime in the resonators. Because of these properties, microresonators have found applications in high resolution spectroscopy, optical filters, frequency stabilization, and all-optical switching [9-11]. The ability to confine light in a small volume leads to an extraordinarily strong light intensity inside the resonator cavity, which enables strong interactions between the light field and the objects placed in the cavity mode volume. This enables a number of applications such as microlasers, detection and sensing, nonlinear optics study, and cavity QED investigation [12-15]. In this chapter, we introduce the basic concept of WGM resonators including the characterizations, various cavity configurations and coupling methods.

2.1 Introduction

Historically, WGMs were first observed in the gallery of St Paul's Cathedral in London. The refocusing effect of WGM was studied by Lord Rayleigh for sound travelling along the gallery [16]. The first observation of WGMs in optics was reported in 1961, where laser action was studied in Sm:CaF₂ crystalline resonators [17]. As shown in Figure 2.1(a), the WGM in a microsphere resonator can be represented by an optical ray propagating along a zig-zag path around the resonator surface due to total internal reflection. Figure 2.1(b) presents the electric field distribution of the resonant mode in the equatorial plane calculated with COMSOL. Resonant condition of a WGM

resonator can be approximated as $2\pi n_{\text{eff}}R = m\lambda$, where n_{eff} is the effective refractive index of the resonant mode, R is the resonator radius, λ is the light wavelength in vacuum, and m is an integer giving the number of wavelengths in a round trip of the resonator. Figure 2.1(c) and (d) show the cross-sectional field distributions along the radial and polar directions. Light field trapped inside the cavity has an exponentially decaying evanescent tail extending into the surrounding medium with the decay length of a few hundred nanometers (Figure 2.1(d)).

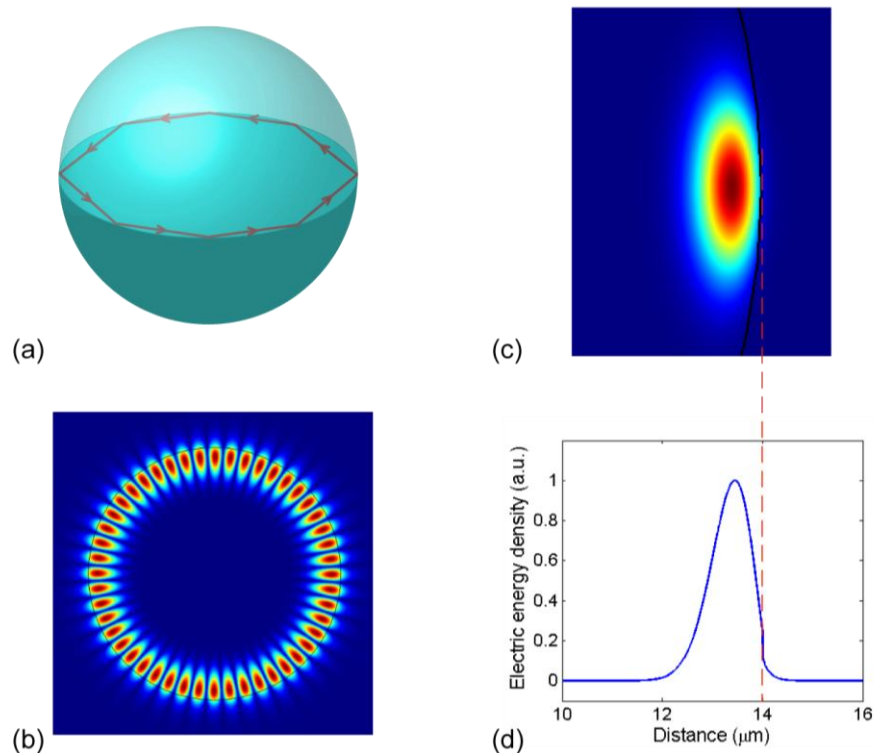


Figure 2.1 (a) Ray optics description of light propagation in a microsphere resonator. (b) Field distribution in the equatorial plane of the microsphere. (c) Two-dimensional cross section mode distribution of the fundamental WGM along the radial and polar directions. (d) Field distribution along the radial direction. The red dashed line denotes the microsphere boundary.

Developments in fabrication technologies have made it possible to fabricate microscale WGM resonators with a variety of materials and shapes [18]. Resonators made from different materials such as liquid droplet, silica, semiconductor, polymer, etc. have been reported [19-24]. Various resonator geometries (Figure 2.2), including microspheres, disks, rings, toroids, cylinders, and bottles, have been demonstrated [25-31].

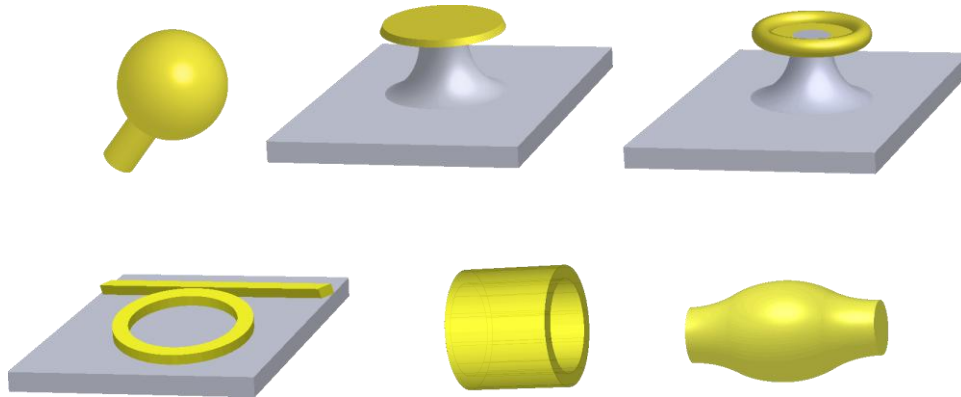


Figure 2.2 Illustrations of various resonator geometries: microsphere, microdisk, microtoroid, microring, microcapillary, and microbottle.

Liquid droplets as optical resonators were first introduced in 1977 by Ashkin and Dziedzic [19]. Liquid droplet resonators are formed by strong surface tension in liquid systems, which results in very smooth boundaries. Although liquid droplet resonators have flexible size tunability, experiments with them suffer from difficulties in manipulation, short lifetime due to the evaporation of droplets, and mechanical instabilities.

The first reported microscale solid WGM resonators were microspheres with diameters of 40~400 μm fabricated from fused quartz with measured Q factors above 10^8 [21]. Initial results with glass spheres indicated that Q values in excess of 10^9 were possible [25]. Microdisks and microrings fabricated from silica glass and semiconductors have been used as on-chip WGM resonators [11,26,32]. Quality factors above 10^6 have been achieved. One big challenge in fabricating such resonators is to reduce the surface roughness, which could induce scattering losses and thus limit the Q factors. In 2003, Armani *et al.* reported on-chip silica microtoroidal resonators with Q factors above 10^8 [27]. The high Q factors are contributed to the minimized scattering losses from the smooth resonator surface created by surface tension during a laser reflow process. Another class of widely used WGM cavities is cylindrical microresonators, which employ microscale glass capillaries with wall thickness of tens to hundreds of microns [29]. Light propagates along the circular cross section of the capillary. Such structures

naturally integrate ring resonators with microfluidic channels, providing a promising platform for applications in biochemical sensing and lasing. Other resonators like microbubbles [33] and microbottles [30,34] are also demonstrated with Q factors above 10^7 for applications such as add-drop filters.

Due to the easy processing, structural flexibility, versatile properties, and low cost, polymer resonators are becoming increasingly competitive to devices made of other materials. A variety of techniques have been reported to fabricate polymer resonators, including molding from a master structure [23,35], direct laser writing using two-photon absorption induced polymerization [36], direct lithographic patterning [9], mechanical turning and polishing [37], and surface-tension based approach [38].

2.2 Coupling Methods

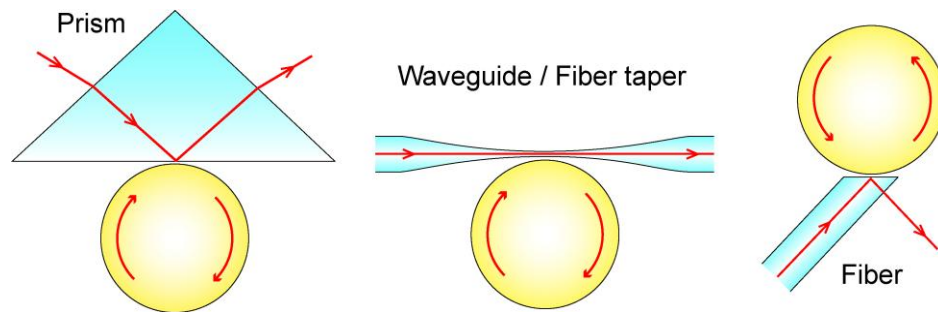


Figure 2.3 Schemes showing evanescent field coupling of light to a resonator using a prism, fiber taper or integrated waveguide, and angle polished fiber.

Near field evanescent coupling has been demonstrated to be able to efficiently couple light into and out of a WGM resonator. It requires an overlap of the WGM evanescent field with the coupler [39]. When phase matching conditions are satisfied, resonant modes can be excited effectively [40]. Several coupling methods have been reported, such as prism coupling [41], tapered fiber [40], integrated waveguide [42], half block [43], and angle polished fiber [44] (Figure 2.3). Among these methods, strip waveguide and fiber taper coupling schemes have emerged as the choices in many applications. Fiber tapers have been generally accepted for the coupling process, and a coupling efficiency

above 99% has been reported [45]. In this study, we use a fiber taper, fabricated by heating and pulling a standard optical fiber, to couple light into and out of the resonator. The phase matching condition can be controlled by the thickness of the taper and the gap between the fiber taper and the resonator [40].

2.3 Resonator Measurements

In this section, we review some parameters commonly used to characterize a microresonator. The quality factor and photon lifetime depend on the losses of the resonator. Free spectral range denotes the periodical property of the resonant modes. Mode volume defines the spatial confinement of the resonant mode.

2.3.1 Q factor and Loss

The Q factor is a measurement of optical losses in a resonator. It is defined as the ratio of the energy stored in the cavity to the energy dissipated per cycle. From Fourier transform, Q factor can be measured spectrally according to

$$Q = \frac{\omega}{\delta\omega} = \frac{\lambda}{\delta\lambda} \quad (2.1)$$

where $\omega(\lambda)$ is the resonance frequency (wavelength), and $\delta\omega$ ($\delta\lambda$) is the linewidth (full width at half maximum, FWHM) of the resonant mode. Therefore, Q factor can be easily calculated by measuring the transmission spectrum of the resonant mode when the wavelength of the injected light is scanned cross the mode resonance.

The total losses of a waveguide coupled resonator consist of material absorption loss, scattering loss, radiation loss, and external coupling loss. The sum of the first three loss mechanisms is referred to as the intrinsic loss of the resonator. The overall quality factor is determined by the individual loss terms according to [21,39,46]

$$\frac{1}{Q} = \frac{1}{Q_{mat}} + \frac{1}{Q_{ss}} + \frac{1}{Q_{rad}} + \frac{1}{Q_{ex}} \quad (2.2)$$

where Q_{mat} is associated with light absorption of the material constituting the resonator, Q_{ss} denotes scattering loss due to surface inhomogeneities and contaminants, Q_{rad} is related to the radiation loss, i.e., escape of light energy through the curvature surface, and Q_{ex} corresponds to the loss induced by the waveguide coupling. Scattering loss can be decreased by improving the fabrication process to reduce the resonator surface roughness. Radiation loss directly depends on the size of the resonator, and can be reduced by increasing the size. When the resonator size is larger than some certain value, which is determined by the resonator geometry, radiation loss becomes negligible compared to other loss mechanisms [43,47].

Denoting α as the propagation loss of light in the resonator, Q factor can be expressed as

$$Q = \frac{2\pi n}{\alpha\lambda}. \quad (2.3)$$

For $n = 1.45$ and $\lambda = 1550$ nm, Q factor of 10^8 corresponds to propagation loss of 0.0588 m^{-1} , which is 0.256 dB/m . If α is the material absorption loss, Eq. (2.3) can be used to estimate Q_{mat} .

2.3.2 Photon Lifetime

Photon lifetime τ_{lifetime} is the time required for the light energy in the resonator to decay to $1/e$ of its original value, and can be calculated by

$$\tau_{\text{lifetime}} = \frac{Q}{\omega}. \quad (2.4)$$

The higher the cavity Q , the longer the photon lifetime. It means that photons are able to circulate the resonator for multiple trips to build up the intracavity power before exiting the resonator by loss mechanism. For example, Q factor of 10^8 corresponds to photon lifetime of 82 ns at wavelength 1550 nm . The round-trip time τ_r of photons is calculated by $\tau_r = 2\pi nR/c$ with c denoting the speed of light in vacuum. For a silica resonator of radius $20 \text{ }\mu\text{m}$, τ_r is around 0.607 ps . Thus the photon lifetime corresponds

to 1.35×10^5 cycles. Light-matter interaction in high- Q resonators is significantly enhanced because of the photon trapping effect.

2.3.3 Free Spectral Range

The free spectral range (FSR) is defined as the frequency spacing Δf_{FSR} or wavelength spacing $\Delta \lambda_{FSR}$ of two adjacent modes in a resonator, and is given by the expression

$$\Delta f_{FSR} \approx \frac{c}{2\pi nR} \quad (2.5)$$

$$\Delta \lambda_{FSR} \approx \frac{\lambda^2}{2\pi nR}. \quad (2.6)$$

It is seen that the FSR increases as the resonator size shrinks. A large FSR allows the development of single-mode lasing and a large sensing range for resonator-based sensors.

2.3.4 Mode Volume

Mode volume V is defined as the equivalent volume that the resonant mode occupies if the energy density is distributed homogeneously throughout the mode volume at the peak value. It is expressed as [48]

$$V = \frac{\int n^2(\mathbf{r}) |\vec{E}(\mathbf{r})|^2 d^3r}{\max\left(n^2(\mathbf{r}) |\vec{E}(\mathbf{r})|^2\right)} \quad (2.7)$$

where $\vec{E}(\mathbf{r})$ is the electric field. The integral is evaluated over all space. The importance of mode volume is that it affects the light intensity inside the resonator, and therefore determines the light-matter interaction strength. Generally, in smaller cavities, the optical mode is more confined, resulting in a smaller mode volume and a higher light intensity [47].

2.4 Coupling Equation

Figure 2.4 represents the schematic of a waveguide and resonator coupling system. The total round-trip losses are determined by the intrinsic loss of the resonator (described by the intrinsic energy decay rate κ_0) and the waveguide-resonator coupling loss (described by the external coupling energy decay rate κ_{ex}).

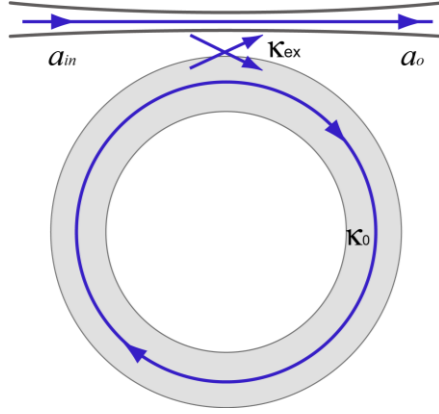


Figure 2.4 Schematic of a waveguide coupled WGM resonator.

Using coupled-mode theory and slowly varying envelope approximation, time evolution of the electric field a inside the resonator can be described by [39,49]

$$\frac{da}{dt} = -\left(i\omega_c + \frac{\kappa_0}{2} + \frac{\kappa_{ex}}{2}\right)a - \sqrt{\kappa_{ex}}a_{in} \quad (2.8)$$

where ω_c is the resonance frequency, $\kappa_0 = \omega_c / Q_0$ is the intrinsic damping rate with Q_0 denoting the intrinsic quality factor of the cavity, $\kappa_{ex} = \omega_c / Q_{ex}$ is the coupling rate with Q_{ex} describing the coupling quality factor, and a_{in} is the input field. The total quality factor $Q = 1/(1/Q_0 + 1/Q_{ex})$ is also referred to as the loaded Q factor. The square magnitude of a is normalized to the stored optical energy in the resonator, and the square magnitude of a_{in} is normalized to the input optical power. Therefore, the input power P_{in} of the waveguide and the intracavity circulating power P_C in the resonator are written as

$$P_{in} = h\nu |a_{in}|^2 \quad (2.9)$$

and

$$P_c = h\nu |a|^2 / \tau_r \quad (2.10)$$

where $h\nu$ is the photon energy with h representing the Planck's constant and ν denoting the photon frequency, and τ_r is the round-trip time. The output through the waveguide consists of the interference between the amount of optical field not coupled into the resonator and the amount coupled out of the resonator, which is expressed as

$$a_o = a_m + \sqrt{\kappa_{ex}} \cdot a. \quad (2.11)$$

The power transmission can be calculated from $T_r = |a_o|^2 / |a_m|^2$.

To obtain the steady-state solution, we apply Fourier transform on Eq. (2.8) and obtain

$$\left(i\Delta\omega - \frac{\kappa_0}{2} - \frac{\kappa_{ex}}{2} \right) a - \sqrt{\kappa_{ex}} a_m = 0 \quad (2.12)$$

where $\Delta\omega = \omega - \omega_c$ is the detuning between the excitation frequency ω and the resonance frequency ω_c . From Eq. (2.12), the intracavity field can be derived as

$$a = \frac{\sqrt{\kappa_{ex}}}{i\Delta\omega - \frac{\kappa_0 + \kappa_{ex}}{2}} a_m. \quad (2.13)$$

By applying Eqs. (2.11) and (2.13), the transmission T_r yields

$$T_r(\Delta\omega) = \left| 1 + \frac{\kappa_{ex}}{i\Delta\omega - \frac{\kappa_0 + \kappa_{ex}}{2}} \right|^2 = \frac{\Delta\omega^2 + \left(\frac{\kappa_0 - \kappa_{ex}}{2} \right)^2}{\Delta\omega^2 + \left(\frac{\kappa_0 + \kappa_{ex}}{2} \right)^2} = 1 - \frac{\kappa_0 \kappa_{ex}}{\Delta\omega^2 + \left(\frac{\kappa_0 + \kappa_{ex}}{2} \right)^2}. \quad (2.14)$$

The waveguide coupling allows light intensity to build up in the resonator. The buildup factor B is defined as the ratio of the circulating power inside the resonator to the incident power, which is

$$B = \frac{P_c}{P_{in}} = \frac{1}{\tau_r} \left| \frac{a}{a_m} \right|^2 = \frac{1}{\tau_r} \frac{\kappa_{ex}}{\Delta\omega^2 + \left(\frac{\kappa_0 + \kappa_{ex}}{2} \right)^2}. \quad (2.15)$$

Obviously, the transmission and buildup factor are functions of the frequency detuning $\Delta\omega$, the intrinsic decay rate κ_0 , and the coupling decay rate κ_{ex} . Figure 2.5 shows the calculated T_r and B as a function κ_{ex} for different $\Delta\omega$.

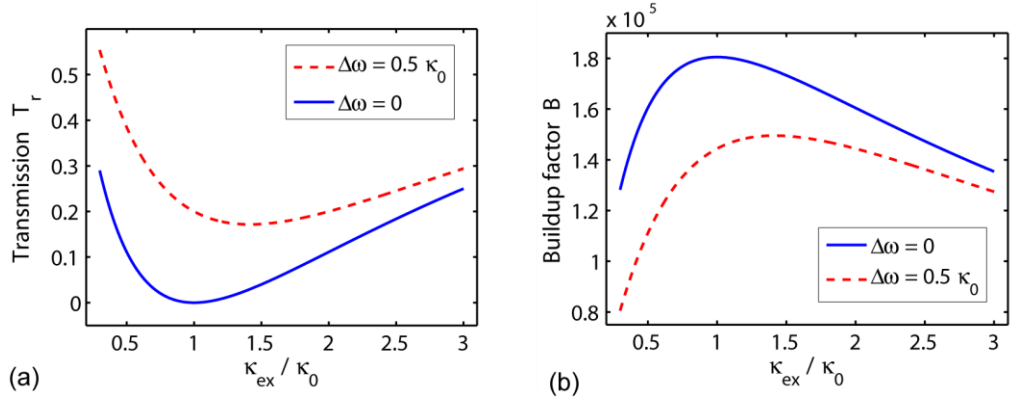


Figure 2.5 Calculated transmission T_r and buildup factor B versus κ_{ex}/κ_0 for a resonator with $n = 1.45$, $R = 15 \mu\text{m}$, and $Q = 10^8$ at $\lambda = 1550 \text{ nm}$.

If the excitation frequency is on resonance with the resonant mode, i.e., $\Delta\omega = 0$, we have the below expressions:

$$\text{Intracavity field: } a = \frac{2\sqrt{\kappa_{ex}}}{-\kappa_0 - \kappa_{ex}} a_{in}$$

$$\text{Circulating power: } P_C = \frac{4\kappa_{ex}}{\tau_r(\kappa_0 + \kappa_{ex})^2} P_{in}$$

$$\text{Output field: } a_o = \frac{\kappa_0 - \kappa_{ex}}{\kappa_0 + \kappa_{ex}} a_{in}$$

$$\text{Transmission: } T_r = \left(\frac{\kappa_0 - \kappa_{ex}}{\kappa_0 + \kappa_{ex}} \right)^2$$

$$\text{Buildup factor: } B = \frac{P_C}{P_{in}} = \frac{1}{\tau_r} \frac{4\kappa_{ex}}{(\kappa_0 + \kappa_{ex})^2}.$$

Depending on the relation between κ_0 and κ_{ex} , there are three coupling regimes to characterize the transmission profile. A large waveguide-resonator gap indicates a small coupling loss.

- (i) Under coupling: $\kappa_0 > \kappa_{ex}$, the coupling loss is less than the intrinsic cavity loss. Phase shift of the transmitted light is zero.
- (ii) Critical coupling: $\kappa_0 = \kappa_{ex}$, the waveguide coupling balances the intrinsic cavity loss. Power transmission at the resonance frequency is zero, and the circulating

power is maximized. All the input power is coupled into the resonator and dissipated out. The loaded quality factor is half of the intrinsic quality factor.

(iii) Over coupling: $\kappa_0 < \kappa_{\text{ex}}$, the coupling loss is larger than the intrinsic cavity loss.

The phase of the transmitted light undergoes a π phase shift.

In the case of resonant excitation ($\Delta\omega=0$), at the critical coupling point ($\kappa_0=\kappa_{\text{ex}}$), the intracavity circulating power becomes

$$P_c = \frac{1}{\tau_r \kappa_0} P_{in} = \frac{\lambda Q_0}{4\pi^2 n R} P_{in} \quad (2.16)$$

and the light intensity inside the cavity is expressed as

$$I = \frac{P_c}{A} = \frac{\lambda Q_0}{2\pi n \cdot 2\pi R \cdot A} P_{in} \approx \frac{\lambda Q_0}{2\pi n V} P_{in} \quad (2.17)$$

where A is the mode area of the resonant mode and V is the mode volume.

For example, for a silica microsphere of $R=15 \mu\text{m}$, $n=1.45$, and $Q_0=10^8$, at resonance wavelength 1550 nm, the volume of the fundamental mode is $283 \mu\text{m}^3$. An input power $P_{in}=1 \text{ mW}$ coupled into the cavity will build up a circulating power as high as 180 W corresponding to a buildup factor $B \sim 1.8 \times 10^5$. The circulating power is concentrated in an effective mode area of $3 \mu\text{m}^2$ leading to a high light intensity of 6 GW/cm^2 .

2.5 Microtoroidal Resonators

Silica microtoroidal resonators were first reported in 2003 [27]. They have attracted intense interests because of their on-chip structure and high Q factors. The toroidal structure is obtained by melting a silica microdisk with a high power CO_2 laser, which gives rise to ultra-smooth surface.

2.51 Fabrication

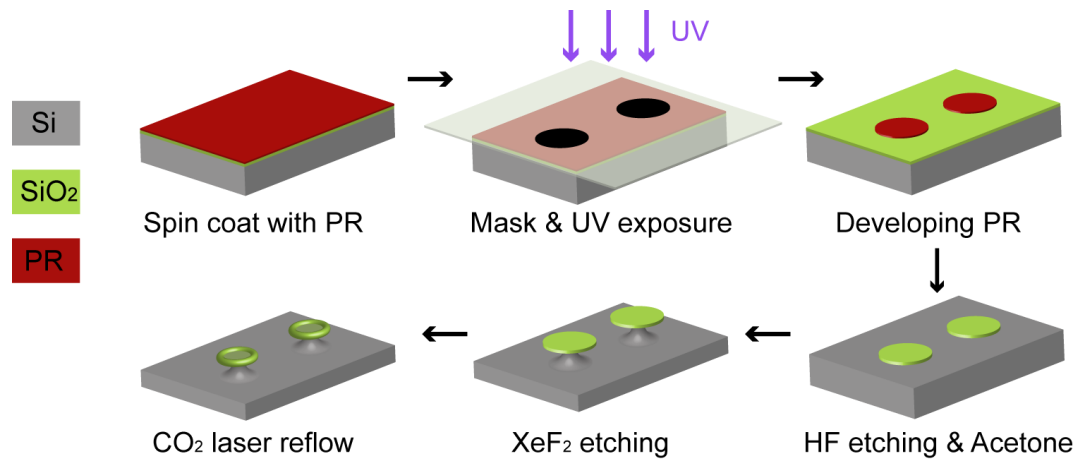


Figure 2.6 Fabrication flow for silica microtoroids on a silicon substrate.

Figure 2.6 shows the fabrication flow of silica microtoroids on a silicon substrate. First, circular silica pads with controlled diameters are obtained through photolithography and buffered-HF etching. To prevent the leakage of light from the silica disks to the silicon substrate, the substrate is isotropically etched using XeF₂. After this process, the silica disks are supported by the remaining silicon pillars. Finally, a high power CO₂ laser is used to reflow the silica disks one by one, during which surface tension causes the disks to collapse into toroids. Optical micrographs in Figure 2.7 depict the top view and side view of a fiber taper coupled microtoroid. The size of the microtoroid is characterized by the major diameter D and minor diameter d .

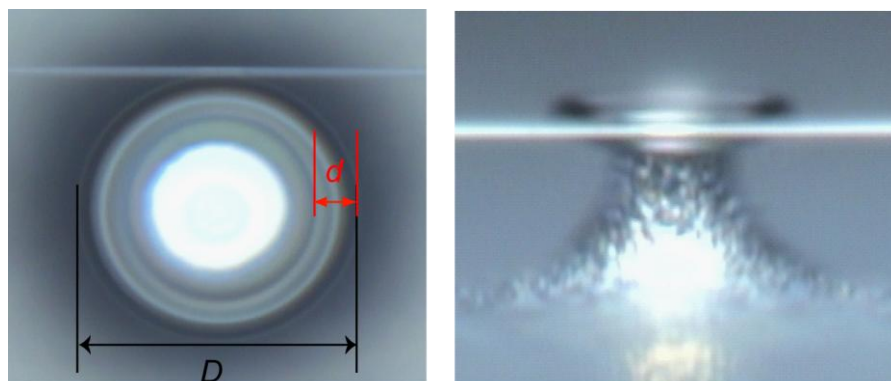


Figure 2.7 Top and side view of a fiber taper coupled microtoroid. The major (D) and minor (d) diameters of the microtoroid are marked in the plot.

2.52 Mode Distribution

Like other WGM resonators, light propagates along the surface of the microtoroid. In the toroidal shaped structure, light is confined in both radial and polar directions, ensuring smaller mode volumes and fewer resonant modes than those in microspheres of the same size [47]. Figure 2.8 presents the electric energy density distribution for WGMs of different orders in a microtoroid and a microsphere in air at 1550 nm. The simulations are performed using COMSOL. The mode volume of the fundamental mode is $270 \mu\text{m}^3$ for toroid and $471 \mu\text{m}^3$ for sphere. Smaller mode volume allows higher intracavity light intensity, and thus stronger light-matter interactions. Fewer resonant modes in the microtoroid makes it a suitable cavity to obtain single-mode lasing. Moreover, in the resonator based sensing applications, it is easier to track the resonance shift of a specific resonant mode if there are a limited number of modes within one free spectral range.

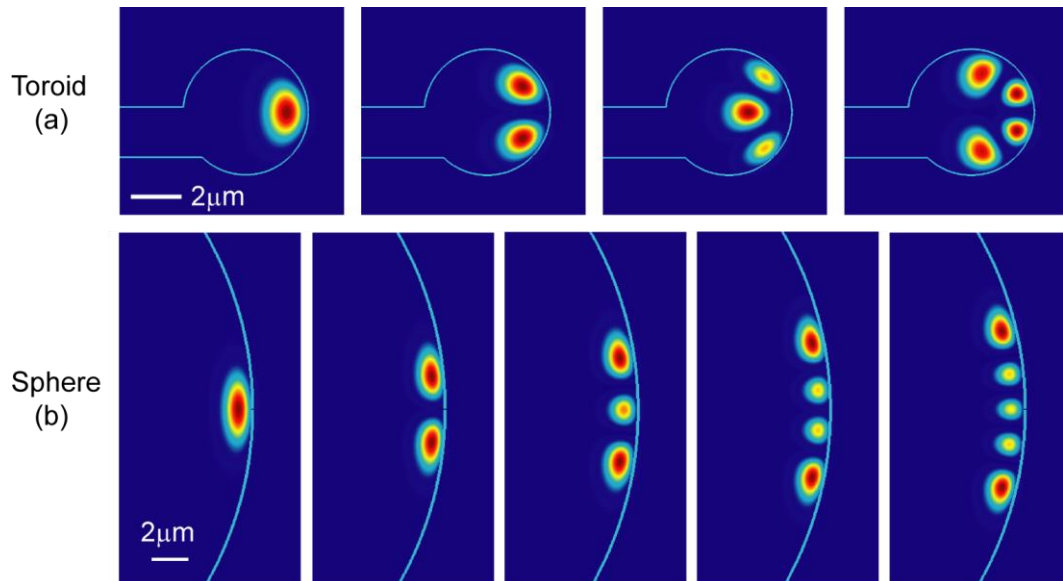


Figure 2.8 Cross section distribution of the electric energy density of WGMs along the radial and polar directions in a silica microtoroid (a) and microsphere (b). The toroid has major and minor diameters of $40 \mu\text{m}$ and $5 \mu\text{m}$, and the sphere has a diameter of $40 \mu\text{m}$.

Chapter 3

Polymer-Silica Hybrid Resonators

Polymer and polymer coated microresonators have attracted increasing interests in recent years due to their advantages (e.g., low cost, diversity, easy fabrication, flexible mechanical properties, rich surface functionalities, and easy incorporation of functional materials) over inorganic materials. Poly(methyl methacrylate) (PMMA), Polystyrene (PS), Poly(dimethylsiloxane) (PDMS) and SU-8 are the commonly used polymers for resonator fabrication because of their good optical properties [23,38,50-52]. PDMS is a soft polymer that is widely used to make microfluidic devices because of its attractive properties such as high dielectric strength, high compressibility, high gas permeability, low chemical reactivity, biocompatibility, and non-toxic nature [53-55]. In this chapter, we first introduce the PDMS coating on a silica microtoroid for thermal compensation in the cavity [56], and then study the thermal oscillation in the transmission spectrum of a PDMS coated silica microtoroid which is the result of competition of thermal effects in the PDMS coating layer and the silica cavity [57].

3.1 Thermal Effect in WGM Resonators

Microresonators have found a wide range of applications such as lasing and sensing. Stability of the resonance wavelengths in such resonators is of great importance in those applications. For instance, the instability of WGMs due to environmental perturbations and probe induced noises directly degrades the sensitivity of the resonator-based sensors and affects the stability of the lasing frequencies. Among different noise sources, temperature variation shows a large effect on the cavity resonances.

The WGM resonances are susceptible to thermal fluctuations caused by either the ambient environmental temperature variations or the absorption of circulating light by the cavity material. From the resonant condition, resonance shift $\Delta\lambda$ can be expressed as

$$\frac{\Delta\lambda}{\lambda} = \frac{\Delta n_{\text{eff}}}{n_{\text{eff}}} + \frac{\Delta R}{R} \quad (3.18)$$

where R is the resonator radius. The shift $\Delta\lambda$ is determined by the refractive index change Δn_{eff} and the cavity size change ΔR , both of which are temperature dependent. As the cavity temperature varies, n_{eff} and R change due to the thermo-optic effect and thermal expansion effect, respectively, giving rise to the resonance shift. The coefficients of thermal-optic and thermal expansion effects for fused silica are $dn/dT=1.19\times 10^{-5} \text{ }^\circ\text{C}^{-1}$ and $(1/R)dR/dT = 5.5\times 10^{-7} \text{ }^\circ\text{C}^{-1}$, respectively, where T denotes the temperature. It is worth noting that refractive index of the cavity material is also related to optical Kerr effect. The third-order nonlinearity for fused silica is $2.2\times 10^{-20} \text{ m}^2/\text{W}$ [58], which is so small that the temperature induced thermal effect plays a major role in determining the refractive index.

The thermal effect induced resonance shift has a two-fold influence. On one hand, temperature fluctuations in the environment will reduce the stability of the cavity resonances. For example, in a silica resonator, corresponding to a temperature change of 1°C , the resonance shift of the WGM at wavelength 1550 nm is around 0.01 nm based on Eq. (3.18). Such effect can be used for temperature sensing with ultra-high sensitivity [38]. On the other hand, high incident power launched into the cavity will cause thermal drift of the resonant mode in the transmission spectrum. As the probe wavelength approaches the resonance of the WGM, light is gradually coupled into the cavity and partially absorbed by the cavity material. Heat generated in this process will change the temperature in the mode volume, and thus cause shift of the resonance wavelength and broadening or compression of the resonance linewidth, leading to a distorted resonance line [59]. As shown in Figure 3.1, in the wavelength up scan, when the cavity is heated up due to light absorption, the resonance wavelength shifts along the direction of the input probe scanning, leading to broadening of the resonant mode. In the wavelength down scan, the resonance wavelength shifts in the opposite direction

with the probe, so the mode is compressed. Since the thermal heating comes from optical absorption, it increases with the input light power, leading to a broader resonant mode.

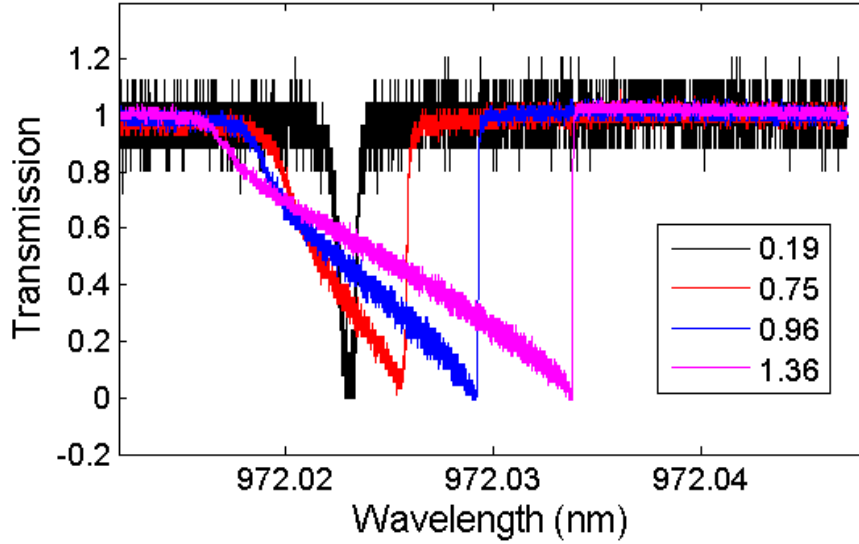


Figure 3.1 Transmission spectra during wavelength up scan at different input powers showing thermal drift of the resonant mode in a silica microtoroid. The input light powers marked in the plot have unit of mW. The microtoroid has major (minor) diameter of 32 (5) μm . The Q factor of the measured resonant mode is 3×10^6 .

3.2 Compensation of Thermal Effect

Since thermo-optic and expansion coefficients for silica are positive, thermal effect cannot be avoided in a pure silica resonator. To reduce the thermal effect, a natural thought is to introduce another material with negative thermal coefficient into the cavity mode volume to compensate for the positive thermal coefficient of silica [60-61]. Most polymer materials, such as PDMS, PMMA, and PS, have negative thermo-optic coefficients and can be used as the compensation layer. In this study, we coat the silica microtoroid with a thin layer of PDMS (GE RTV615A and B, 7:1), which has thermo-optic coefficient of $-1.0 \times 10^{-4} \text{ } ^\circ\text{C}^{-1}$, for the compensation purpose.

3.2.1 PDMS Coating

For polymer coating, different methods have been introduced including spin coating, drop coating, and dip coating. The thickness of the coating layer depends on the material viscosity, spin speed, and dip speed [62-63]. Due to the high viscosity of PDMS, traditional coating methods are not suitable for homogeneous coating of a microtoroid which has an over-hang structure, since some PDMS residue might stick between the under-cut ring and the substrate leading to light leakage and Q degradation.

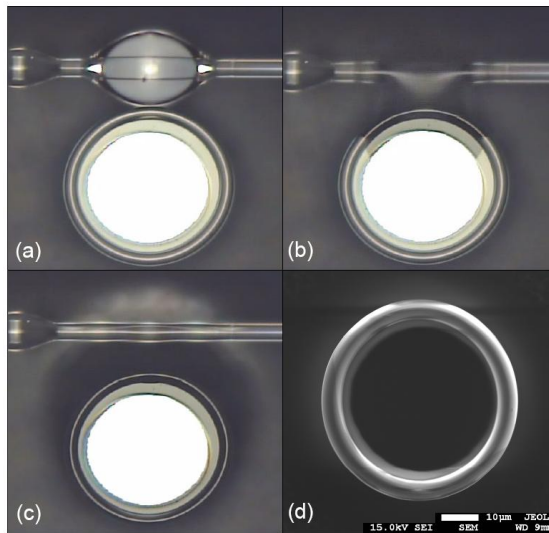


Figure 3.2 Illustration of PDMS coating on a silica microtoroid by wetting technique. (a) A PDMS droplet on a fiber taper adjacent to a microtoroidal resonator. (b) The resonator is partially wetted by PDMS. (c) Liquid PDMS spreads along the resonator surface forming a thin coating layer. (d) SEM image of a PDMS coated microtoroid.

Based on the low surface tension of PDMS, we developed a wetting method to selectively coat a single microtoroid [56,64]. The coating process is depicted in Figure 3.2. First, a fiber tip with diameter around 10 μm is obtained from a standard single mode fiber using a heat-and-pull setup [40]. Subsequently, a PDMS droplet is formed at the end of the fiber tip by dipping the fiber tip into liquid PDMS shortly. Then the PDMS droplet on the fiber tip is transferred to a fiber taper by touching the taper with the tip end (Figure 3.2(a)). Afterwards, the microtoroid, which is mounted on a 3-axis piezo-controlled translational stage, is carefully moved towards the fiber taper to touch the PDMS droplet with its toroidal edge. Due to low surface tension, parts of the liquid

PDMS spread out along the peripheral ring of the microtoroid and form a smooth thin layer, while other parts remain on top of the disk and have a negligible influence on the resonant modes. Finally, it takes 24 hours for the PDMS coating to cure at room temperature. Scanning electron microscope (SEM) image in Figure 3.2(d) shows a smooth coating surface on the microtoroid.

The coating thickness t_p can be roughly estimated by $t_p = \eta_p D_p^3 / 6\pi Dd$, where D_p denotes the diameter of the PDMS droplet on the fiber taper, D and d are the major and minor diameters of the microtoroid, respectively, and η_p is the fraction of PDMS that flows along the toroidal ring surface which depends on D_p , D , d , and the relative position between the PDMS droplet and the microtoroid.

3.2.2 Theoretical Simulation

We first investigate theoretically the effects of the PDMS coating layer on the silica microtoroid. In a coated microtoroid, light propagates along the peripheral ring interface of silica and PDMS with its evanescent tail extending into the PDMS layer because of the small contrast of refractive indices between silica (1.445) and PDMS (1.41). Finite element method (FEM) is applied to compute the field distribution of the fundamental WGM as shown in Figure 3.3.

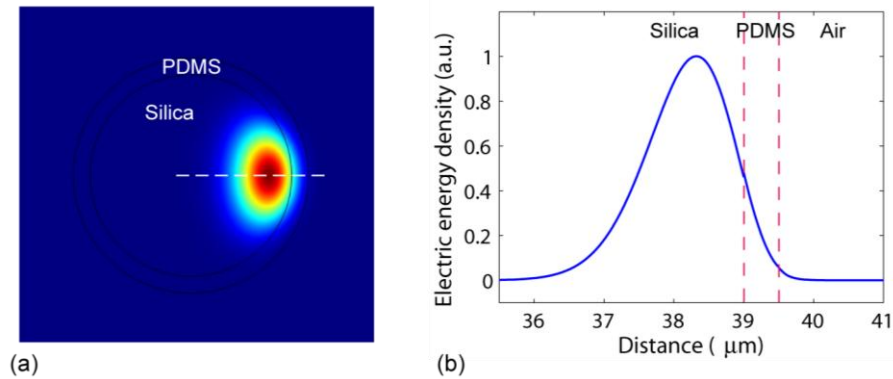


Figure 3.3 (a) Two-dimensional cross section field distribution of the TE polarized fundamental mode in a PDMS coated silica microtoroid. (b) Normalized field distribution along the radial direction as marked by the white dashed line in (a). The silica microtoroid has major (minor) diameter of 78 (6) μm . The thickness of the PDMS layer is 0.5 μm as denoted by the red dashed lines in (b).

The effective refractive index of the WGM of interest can be expressed as [65]

$$n_{\text{eff}} \approx \eta_1 n_1 + \eta_2 n_2 \quad (3.19)$$

where n_1 and n_2 represent the refractive index of silica and PDMS, respectively. η_1 and η_2 denote the fractions of light energy traveling in the silica ring and the PDMS layer, respectively. The sum of η_1 and η_2 is nearly 1 since the fraction of light energy in air outside the PDMS layer is negligible (Figure 3.3). Derived from Eq. (3.19), the change of n_{eff} versus temperature change (effective thermo-optic coefficient) yields

$$\frac{dn_{\text{eff}}}{dT} \approx \eta_1 \frac{dn_1}{dT} + \eta_2 \frac{dn_2}{dT} \quad (3.20)$$

where dn_1/dT and dn_2/dT denote the thermo-optic coefficient of silica (positive) and PDMS (negative), respectively. By adjusting the coating thickness, η_1 and η_2 can be controlled to reduce the absolute value of dn_{eff}/dT , thus reducing the total thermo-optic effect of the resonator. By setting Eq. (3.20) to zero, we obtain that the fraction η_2 should be 0.106 to compensate for the positive thermo-optic effect in silica completely.

Besides n_{eff} , the PDMS coating layer also affects the cavity Q factors. Without the coating layer, Q factor of the resonator is mainly determined by the absorption of silica for resonator diameters larger than 30 μm [43,47]. With the PDMS coating, the total quality factor Q_{tot} is expressed as

$$\frac{1}{Q_{\text{tot}}} = \frac{1}{Q_{\text{silica}}} + \frac{1}{Q_{\text{PDMS}}} \quad (3.21)$$

where Q_{silica} and Q_{PDMS} denote the quality factors induced by the power loss in silica and PDMS, respectively. Due to the large absorption loss of light in PDMS (0.4 dB/cm in 1550 nm band), Q_{PDMS} becomes dominant to determine Q_{tot} .

By increasing the coating thickness, more light energy distributes in the PDMS layer so that η_2 increases and η_1 decreases. As a result, the loss in PDMS increases, leading to a decrease in Q_{tot} as shown in Figure 3.4. Fractions η_1 and η_2 are calculated by integrating the light energy of the fundamental mode over the silica ring and the PDMS layer,

respectively. When the thickness of the PDMS layer is $0.55 \mu\text{m}$, η_2 is around 0.106, resulting in a complete compensation of the positive thermo-optic effect in silica. For $t_p < 0.55 \mu\text{m}$ ($t_p > 0.55 \mu\text{m}$), the effective thermo-optic coefficient (Eq. (3.20)) is positive (negative), leading to a red (blue) shift of the resonance wavelength with temperature.

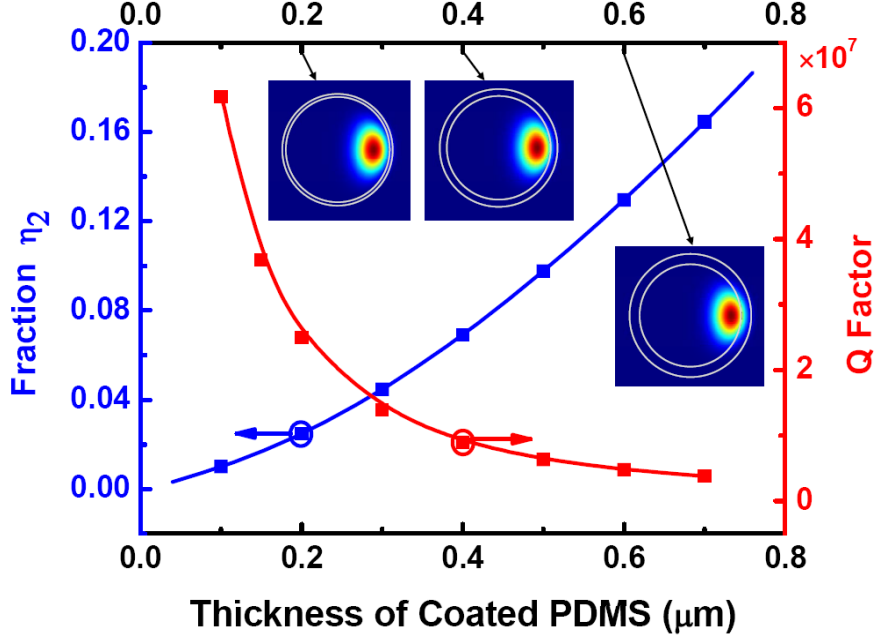


Figure 3.4 Simulation results showing the light fraction in the PDMS layer η_2 and the total Q factor of the fundamental mode as a function of the PDMS coating thickness t_p . The major and minor diameters of the microtoroid used in the simulation are $D(d) = 78(6) \mu\text{m}$. Inset: Two-dimensional field distribution of the resonant mode for $t_p = 0.2, 0.4, \text{ and } 0.6 \mu\text{m}$.

3.2.3 Experimental Results

Based on the theoretical results, we designed two experiments to investigate the dependence of thermal effect and cavity Q on the PDMS coating thickness. Figure 3.5 shows the experimental setup. A tunable external cavity continuous-wave laser in 1550 nm band is used to excite the WGMs and a 100-Hz triangle wave from a function generator is used to perform the fine scan of the laser frequency. The frequency scanning range is 25 GHz for the fine scan. Thus, the transition time of the laser frequency scanning through a WGM of quality factor $Q > 10^5$ is smaller than $400 \mu\text{s}$, which is much shorter than the response time of the thermal expansion effect, i.e., tens

of milliseconds [59]. Therefore, the thermal expansion effect can be neglected in the fast thermodynamic process. A fiber taper connected to the laser source is placed next to the microtoroid to couple light into and out of the toroid [66]. The output light from the fiber taper is detected by a low noise photodetector connected to an oscilloscope to observe the transmission spectra of the WGMs. The microtoroid used in the experiments has a major (minor) diameter of 78 (6) μm . Before PDMS coating, the Q factor of the fundamental mode is around 2×10^7 .

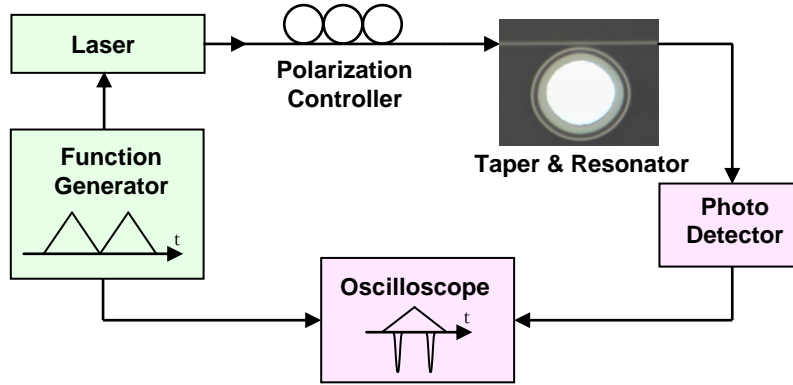


Figure 3.5 Schematics of the experiment setup.

In the first experiment, the microtoroid is coated with a PDMS layer of 0.31 μm . Thermal responses of four different WGMs in the same microtoroid are depicted in Figure 3.6. We increase the input optical power of the fiber taper to mimic the temperature increase, since temperature increase of the cavity is proportional to the absorbed light energy and thus the input light power. In Figure 3.6, the mode with the highest Q (4.2×10^6 , fundamental mode) shows positive thermal effect while the other three high-order modes show negative thermal effect. This can be understood by the fact that the high-order mode has a larger portion of light field distributed in the PDMS layer. The fraction η_2 for the fundamental mode is smaller than 0.106 which leads to insufficient compensation of the positive thermal effect in silica, while η_2 for the high-order mode is larger than 0.106 resulting in over compensation.

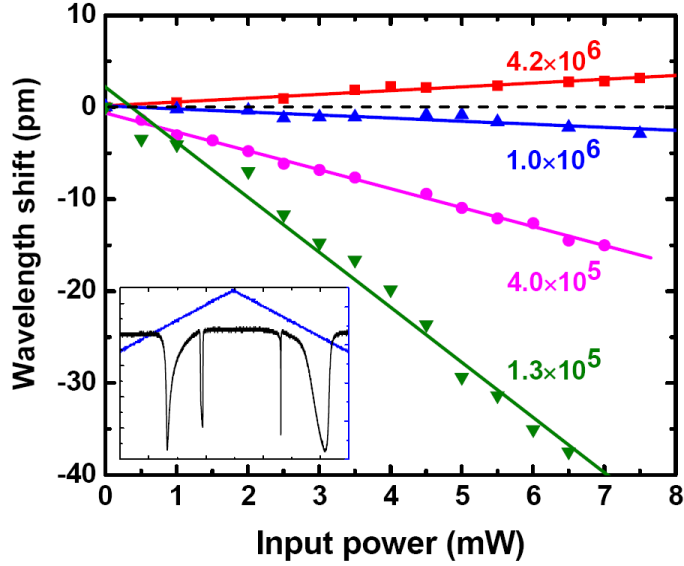


Figure 3.6 Resonance shift as a function of input optical power for four different WGMs in the same PDMS coated microtoroid ($t_p = 0.31 \mu\text{m}$). The dashed line indicates the curve without thermal effect. Inset: Two resonant modes (black line) during up and down wavelength scan of the pump laser (blue line). It is clearly seen in the transmission spectrum that the high Q mode ($\sim 2 \times 10^6$) shows a resonance red shift (i.e., linewidth broadening occurs in the wavelength up scan), while the low Q mode ($\sim 10^5$) shows a blue shift (i.e., linewidth broadening occurs in the wavelength down scan).

In the second experiment, we study the thermal effect of the fundamental WGM at different coating thickness. Figure 3.7 shows that the Q factor decreases with the increasing coating thickness, and the resonance wavelength experiences a transition from red to blue shift. At the thickness of $t_p = 0.52 \mu\text{m}$, the Q factor becomes 1.5×10^6 and the positive thermal effect is compensated completely by the PDMS layer. The thickness $0.52 \mu\text{m}$ deviates from the theoretical result which might be because the practical thermo-optic coefficient of PDMS is slightly different from the value of $-1.0 \times 10^{-4} \text{ } ^\circ\text{C}^{-1}$ used in the simulation. On the other hand, the measured Q factor is one order of magnitude lower than the simulation result, which may result from the contaminations induced in the coating process and the deviation of the PDMS absorption coefficient from the theoretical value. When the coating thickness is smaller than $0.52 \mu\text{m}$, certain high-order mode may have its thermal effect in silica compensated completely when its η_2 reaches 0.106. However, the fundamental mode with complete thermal

compensation possesses the smallest mode volume and can provide the highest sensitivity.

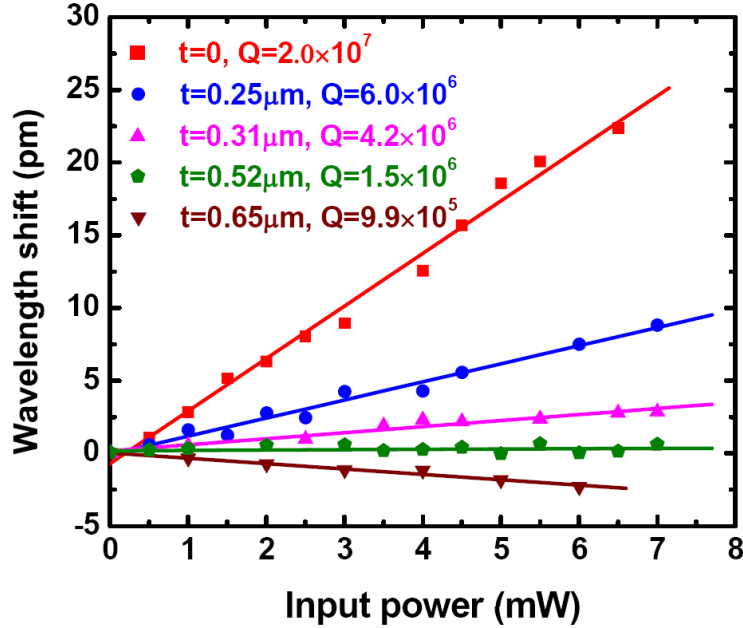


Figure 3.7 Resonance shift of the fundamental WGM versus input optical power for various PDMS coating thickness. The data is measured near the wavelength of 1550 nm.

In summary, we have developed a novel method for coating PDMS on a single selected microtoroid, and demonstrated complete compensation of thermal effect in WGMs thanks to the negative thermo-optic coefficient of PDMS. The measured Q factor is higher than 10^6 with the coating layer. The coated microtoroids can be used in bio/chemical sensing to improve the measurement precision. They also hold potential applications in nonlinear optics because of the larger nonlinear coefficient of PDMS over silica.

3.3 Thermal Oscillation

In this section, we study the thermal oscillations in the transmission spectra of a PDMS coated silica resonator. We demonstrate that the competing thermal effects in silica and PDMS lead to self modulation of the transmitted power. A theoretical model is built using thermal dynamics and coupled mode theory to analyze the oscillation behaviors.

Effects of input power, taper-cavity gap, and wavelength scanning speed on the oscillation behaviors are investigated with a detailed comparison between the theory and experiments [57].

3.3.1 Introduction

The combination of high Q factor and small mode volume allows buildup of high light intensity in the WGM resonator, and gives rise to large optical nonlinearities [58,67-68] and thermal effects [69-72]. Some typical thermal responses, such as distorted asymmetric lineshape and hysteresis have been investigated in high Q resonators [59,70]. In silica microspheres, oscillations from competition between different nonlinearities have been observed [69,72]. In silicon resonators, self modulation due to competing free carriers and phonon populations has been reported [73]. To summary, transmission oscillations can exist in a resonator possessing pairs of closely spaced modes. When nonlinear resonant response of the two neighboring modes is overlapped, periodical oscillations are produced by cyclic transitions of the resonance between the two modes. Similar oscillations can also exist in a resonator system possessing two nonlinear mechanisms which have opposite sign of nonlinear coefficient.

Resonators composed of multiple materials can lead to improved performance and novel behaviors not attainable in single-material resonators. It has been demonstrated that silica microcavities with appropriate coating layer can help increase the sensitivity of resonator-based biosensors [74], and compensate for the thermal effects [56]. Thermal response of the power transmission in such multi-layer resonators remains to be studied. Here we experimentally and theoretically analyze the thermally induced oscillations in the transmission of a PDMS coated silica microtoroid. We demonstrate that such oscillations are attributed to the competition between the opposite thermal effects in the silica core and the PDMS coating layer.

The multi-layer resonator for test is prepared by coating a silica microtoroid of major (minor) diameter of 42 (6) μm with a PDMS layer of thickness $t_p \sim 0.2 \mu\text{m}$. The negative thermo-optic coefficient of PDMS can compensate for the positive thermal effect in the silica resonator. The thickness of the coating layer is smaller than the critical value 0.43 μm which is required to completely compensate the thermal effect in silica. The measurement setup is similar as the one shown in Figure 3.5. A tunable laser in 1450 nm band is used to excite WGMs in the resonator. The highest Q factor of the coated toroid is 3.8×10^6 measured at a low input power to avoid thermal effect. Figure 3.8 presents the transmission spectra for two different input powers. Thermal effects result in a hysteretic response featured by broadening and compression of the resonance line during wavelength up and down scans, respectively. In Figure 3.8(a), during wavelength up scan, the distorted asymmetric lineshape exhibits a sharp drop followed by a mild recovery. Figure 3.8(b) depicts that at a large input power, a fine structure characterized by oscillations within the resonant mode shows up. This is attributed to the competition between silica and PDMS for their opposite thermo-optic effects, different thermal relaxation time, and thermal absorption coefficients. In this study, we consider the oscillation behaviors in the transmission spectrum during wavelength up scan, as they exhibit more interesting features.

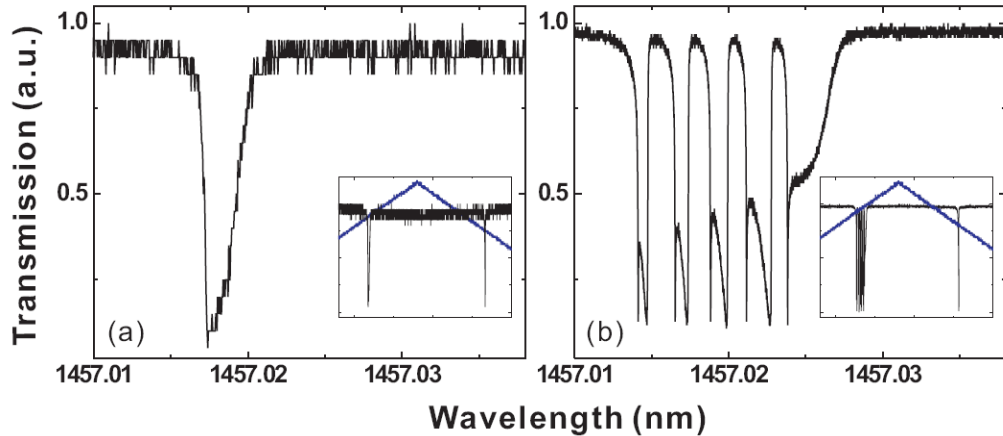


Figure 3.8 Transmission spectra of a resonant mode in a PDMS coated silica microtoroid at input powers of 0.7 mW (a) and 3.1 mW (b). The wavelength scanning speed is 40 nm/s. Insets: Transmission spectra corresponding to the same resonant modes for wavelength up and down scans (blue line: triangle wave from the function generator).

3.3.2 Theoretical Model

The dynamic process of the thermal flow and the induced resonance shift in polymer coated silica microtoroids are discussed in this section. In the resonator system, light absorption induced temperature changes in silica and PDMS are distinct due to their different thermal properties. Assuming the temperature changes within the mode volume in silica and PDMS are $\Delta T_1(t)$ and $\Delta T_2(t)$, respectively, the resonance wavelength $\lambda_c(t)$ can be written as [59]

$$\lambda_c(t) \approx \lambda_0 \left(1 + \frac{\eta_1 \frac{dn_1}{dT} \Delta T_1(t) + \eta_2 \frac{dn_2}{dT} \Delta T_2(t)}{n_{\text{eff}}} + \frac{n_{\text{Kerr}}}{n_{\text{eff}}} \frac{P_c(t)}{A} \right) \quad (3.22)$$

where λ_0 is the cold cavity resonance wavelength, dn_1/dT and dn_2/dT designate the thermo-optic coefficients of silica and PDMS, respectively, n_{eff} is the effective refractive index of the resonant mode which is calculated by Eq. (3.19), n_{Kerr} represents the optical Kerr coefficient of fused silica, A is the WGM mode area, and $P_c(t) = |E_c(t)|^2 / \tau_r$ is the circulating power in the cavity with $E_c(t)$ and $\tau_r \sim 2n_{\text{eff}}\pi R/c$ describing the intracavity field and the cavity round-trip time, respectively. The second term in the bracket describes the resonance shift induced by thermo-optic effects in silica and PDMS. The third term includes the effect from optical Kerr nonlinearity in silica. Since the thermal expansion coefficient of silica is much smaller than its thermo-optic coefficient and the coating layer is too thin to introduce significant expansion, we have neglected the thermal expansion effects in Eq. (3.22) and in the following discussions.

Dynamics of temperature changes in the resonator and the intracavity field can be expressed by the rate equations [39,75]

$$\frac{d\Delta T_i(t)}{dt} = -\gamma_{\text{th},i} \Delta T_i(t) + \gamma_{\text{abs},i} P_c(t) \quad (3.23)$$

and

$$\frac{dE_c(t)}{dt} = - \left[\frac{\kappa_0 + \kappa_{\text{ex}}}{2} + i\Delta\omega(t) \right] E_c(t) + i \frac{t_c}{\tau_r} E_{\text{in}}. \quad (3.24)$$

Equation (3.23) describes time evolution of the temperature variations $\Delta T_i(t)$ within the mode volume ($i=1$: Silica, and $i=2$: PDMS) with $\gamma_{th,i}$ depicting the thermal relaxation rate, and $\gamma_{abs,i}$ representing the thermal absorption coefficient. The first term on the right side of Eq. (3.23) describes the heat dissipation process, while the second term denotes temperature changes due to light absorption. In Eq. (3.24), $\kappa_0 = \omega_c / Q_0$ describes the intrinsic loss rate of the cavity, $\kappa_{ex} = \omega_c / Q_{ex}$ is the taper coupling induced decay rate, $t_c = (\kappa_{ex} \tau_r)^{1/2}$ is the coupling coefficient from the fiber taper to the cavity, and $\Delta\omega(t) \equiv \omega_s(t) - \omega_c(t)$ is the detuning between the excitation frequency ω_s and the resonance frequency ω_c . The total Q factor is calculated by $1/Q = 1/Q_0 + 1/Q_{ex}$. Input field E_{in} is assumed to be constant during the laser frequency scan, and it is related to the power P_{in} launched into the fiber taper through $|E_{in}|^2 = P_{in} \cdot \tau_r$.

To study the thermal effects in a resonator, two important thermal mechanisms should be considered: a faster one describing heat dissipation from the mode volume to the rest of the cavity with a relaxation time of microseconds, and a slower one depicting temperature equalization of the cavity as a whole with the environment with a relaxation time of tens of milliseconds [69-71]. The WGM we studied has a quality factor of $Q_0 \sim 3.8 \times 10^6$ at resonance frequency $\omega_c \sim 1.3 \times 10^{15}$ rad/s. For the wavelength scanning speed of 40 nm/s, 80 nm/s, and 120 nm/s in our experiments, the transition time τ_{trans} for the excitation wavelength scanning through the resonant mode is $\tau_{trans} \sim 9.6 \mu\text{s}$, 4.8 μs , and 3.2 μs , respectively. This timescale is comparable with the relaxation time of the faster thermal mechanism, but is much faster than the slower thermal mechanism. Thus, in the theoretical model, we consider only the thermal dissipation from the mode volume to the rest of the cavity. Therefore, $\gamma_{th,i}$ in Eq. (3.23) is determined by thermal conductivity K_b , heat capacity C_b , density ρ_i of the cavity materials, geometry of the cavity, and WGM mode volumes in the specified cavity layers $V_{mode,i}$. The thermal absorption coefficient can be estimated by $\gamma_{abs,i} \sim \alpha_{abs,i} c \tau_r \eta_i / (C_b \rho_i V_{mode,i} n_{eff})$, where $\alpha_{abs,i}$ is the linear absorption coefficient of the cavity material. In practical experiments, it is difficult to

estimate the values of $\gamma_{\text{th},i}$ and $\gamma_{\text{abs},i}$, however, we can keep these parameters adjustable to find the best fit to experimental data [59].

The time used to build up a stable resonant mode inside a resonator is characterized by the photon lifetime $\tau_{\text{lifetime}}=Q_0/\omega_c$ which is 2.9 ns in our experiments. Since $\tau_{\text{trans}} \gg \tau_{\text{lifetime}}$ is always satisfied, the resonant mode has long enough time to fully develop. Therefore, we can analyze Eq. (3.24) in steady-state situation by setting the time derivative of $E_c(t)$ to zero and obtain

$$E_c(t) = \frac{it_c}{\tau_r[\delta_0 + \delta_c + i\Delta\omega(t)]} E_{\text{in}}. \quad (3.25)$$

The electric field coupled out of the resonator is expressed as

$$E_o(t) = \sqrt{1-t_c^2} E_{\text{in}} + it_c E_c(t). \quad (3.26)$$

Consequently, the normalized power transmission $T_r = |E_o(t)|^2 / |E_{\text{in}}|^2$ is used to characterize the performance of the resonator.

Table 3.1 Parameters used in the numerical simulations.

Parameters	Values		Units	Source
D	42		μm	measurement
d	6		μm	measurement
t_{PDMS}	0.2		μm	measurement
Q_0	3.8×10^6		-	measurement
c	2.998×10^8		m/s	constant
A	3.05		μm^2	simulation
n_{Kerr}	2.2×10^{-20}		m^2/W	constant
	Silica	PDMS		
$\alpha_{\text{abs},i}$	0.0156	2.3	m^{-1}	constant
n_i	1.45	1.41	-	constant
η_i	0.966	0.034	-	simulation
$V_{\text{mode},i}$	501	18	μm^3	simulation
dn_i/dT	1.2×10^{-5}	-1.0×10^{-4}	K^{-1}	constant
C_i	740	1300	J/kg/K	constant
ρ_i	2200	965	kg/m^3	constant
K_i	1.38	0.20	$\text{W}/\text{m}/\text{K}$	constant
$\gamma_{\text{th},i}$	90	9280	kHz	fitting
$\gamma_{\text{abs},i}$	1.83×10^3	4.77×10^5	K/J	fitting

Parameters used in the simulations are listed in Table 3.1. Among them, \mathcal{A} , η_1 , η_2 , $V_{\text{mode},1}$ and $V_{\text{mode},2}$ are obtained by calculating the WGM field distribution in the silica core and the PDMS coating layer.

3.3.3 Experimental Results

In this section, we discuss the observed oscillations in the transmission spectra and study quantitatively the dynamics of temperature changes within the mode volume in silica and PDMS. In Figure 3.9, simulation results using the theoretical model show a good agreement with the experimental data in Figure 3.8(b). Temperature variations and resonance shift during the transmission oscillation are presented for analysis. The first oscillation cycle is enlarged in Figure 3.9(d)-(f) to analyze the transmission in four distinct regions. It is noted that Kerr effect is two orders of magnitude smaller than the thermo-optic effect in silica, so λ_c is mainly determined by the second term in Eq. (3.22). If the second term is positive, λ_c shows a red shift, otherwise it has a blue shift.

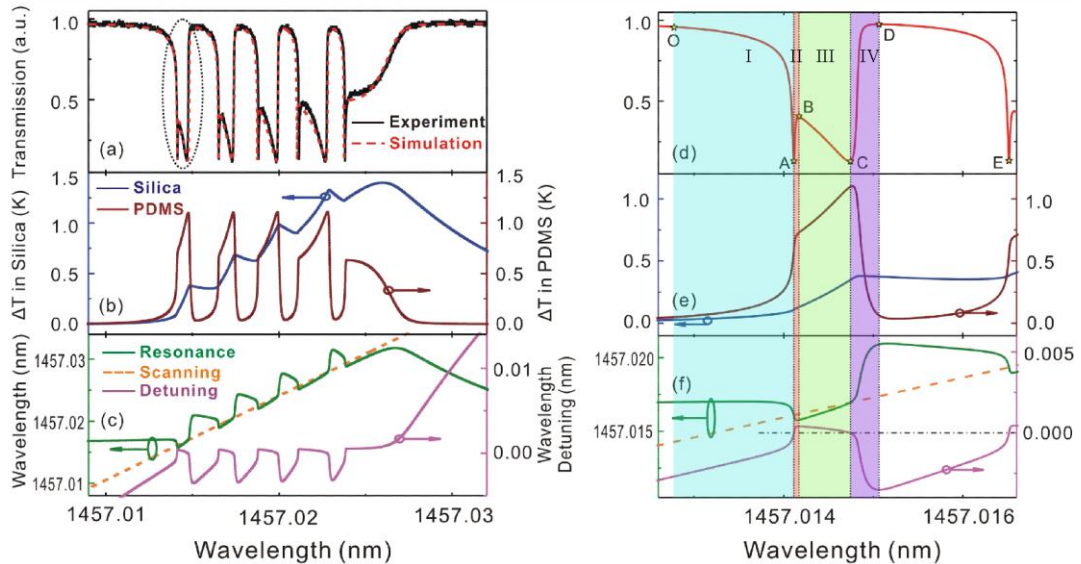


Figure 3.9 Thermally induced oscillations in the transmission spectrum of a PDMS coated silica microtoroid. (a) Measured and calculated transmission spectrum. (b) Calculated temperature changes in silica and PDMS. (c) Calculated resonance wavelength λ_c , scanning wavelength λ_s , and the detuning $\Delta\lambda \equiv \lambda_s - \lambda_c$. (d)-(f) Zoom-in plots of (a)-(c) for the first oscillation cycle marked by the dotted oval in (a). The oscillation cycle is divided into four regions (I-IV) marked by different colors. The black dot-dashed line in (f) represents zero detuning.

Region I: When the scanning wavelength λ_s gets closer to the resonance wavelength λ_r , light is gradually coupled into the resonator, leading to a gradual decrease in the transmission between points O and A as shown in Figure 3.9(d). As a result of light absorption, the WGM experiences a temperature increase, which subsequently induces a refractive index increase in silica and decrease in PDMS. In Figure 3.9(e), the temperature increase in PDMS is larger than that in silica, explained by the larger optical absorption of PDMS. Thus, thermal effect in PDMS layer becomes dominant, inducing a blue shift in λ_c (green line in Figure 3.9(f)). Since λ_s and λ_c move in opposite directions, $\Delta\lambda$ goes to zero rapidly (purple line in Figure 3.9(f)), resulting in a sharp drop in the transmission. At point A, λ_s is on resonance with the resonant mode, i.e., $\Delta\lambda=0$, and the transmission reaches its minimum determined by the coupling between the fiber taper and the cavity.

Region II: In this region, temperatures of the mode volume in silica and PDMS keep increasing. At the beginning of this region, the thermal effect of PDMS still dominates, so λ_c keeps a blue shift. Since λ_c and λ_s shift in opposite directions, a quick increase in $\Delta\lambda$ accompanied by an increase in the transmission is observed in Figure 3.9(e) and (d). Gradually, the thermal effect in silica becomes stronger, and λ_c experiences a transition from blue to red shift as the wavelength up scan continues. Although the red shift allows λ_c moving in the same direction with λ_s , the pace of the red shift of λ_c cannot catch up with the wavelength scan speed, so the transmission increases continuously. Finally at point B, λ_c exhibits the same red shift speed with λ_s and $\Delta\lambda$ reaches a local maximum, leading to a local maximum in the transmission. The time width of region II is around 2.35 μs .

Region III: After passing point B, the thermal effect of silica prevails since a stable temperature rise has been established in silica. As a result, the red shift of λ_c becomes faster than that of λ_s , leading to a gradual decrease in the magnitude of $\Delta\lambda$, which is

reflected in the decrease of the transmission. At point C, λ_c finally catches up with λ_s , so the transmission reaches its minimum again. In this region, the reduction in the slope of temperature increase in PDMS is attributed to the enhanced heat dissipation from the mode volume in PDMS at high temperature to the rest part of PDMS. The time width of region III is around 11.6 μs .

Region IV: After passing point C, the red shift of λ_c continues and $\Delta\lambda$ deviate from zero again. This increases the transmission and reduces the absorbed power as well as heat generation in the cavity. When absorption is smaller than heat dissipation, temperature in the mode volume begins to decrease. The rate of temperature decrease in PDMS is much faster than that in silica because of the larger heat dissipation coefficient of PDMS. Therefore, λ_c is more affected by the temperature decrease in PDMS showing a faster red shift than λ_s . The fast separation of λ_c from λ_s helps recover the transmission quickly. At point D, λ_c is largely detuned from λ_s resulting in a maximum transmission. The time width of region IV is around 7.84 μs .

After λ_s passing point D, the temperature decrease in silica induces a blue shift of λ_c which pushes λ_c toward λ_s and leads to light coupling into the cavity. This starts heating up the PDMS which further enhances the blue shift of λ_c . The decreasing $\Delta\lambda$ leads to a gradual decrease in the transmission again. The cycle repeats until the light absorption cannot balance out the heat dissipation in silica so that the red shift of λ_c lags behind the up scan of λ_s .

In Figure 3.9(a), as λ_s increases, the width of AC (Figure 3.9(d)) in each cycle increases, while the width of CE decreases. This can be explained as follows. The width of AC (CE) is mainly determined by the temperature increase (decrease) rate in silica as shown in Figure 3.9(b). When the oscillation starts, the temperature in silica keeps increasing until the oscillation cycles end. Equation (3.23) shows that higher temperature causes slower (faster) temperature increase (decrease) rate in AC (CE) region. Moreover, λ_s and

λ_c are moving in the same direction in AC region with $\lambda_s > \lambda_c$, but in opposite directions in CE region with $\lambda_s < \lambda_c$. Therefore, as the wavelength up scan goes on, longer time is needed in AC region for λ_c to catch up with λ_s , while in CE region, shorter time is expected for λ_c to coincide with λ_s .

The above discussions clearly show that the transmission oscillations are induced by the opposite thermal drifts of the resonance wavelength in different cavity materials. During the wavelength scan process, λ_c exhibits blue and red shifts alternately and gives rise to continuous changes between positive and negative $\Delta\lambda$, leading to oscillations in the transmission spectrum. In what follows, we investigate the effects of input power, taper-cavity gap, and wavelength scanning speed on the oscillations. The tested PDMS coated resonator is the same as the one measured in Figure 3.8, and the measured WGM is at around 1448.3 nm

Figure 3.10 presents the transmission spectra at various input powers in the under coupling region. Numerical simulation shows a good agreement with the experimental results. The corresponding λ_s and λ_c are calculated and shown in the insets. For a small input power, no oscillation exists in the transmission spectrum as show in Figure 3.10(a). This is because the temperature induced resonance shift cannot catch up with the up scan of λ_s at a low power level. In particular, the red shift of λ_c induced by the temperature increase in silica is not fast enough to catch up with λ_s , leading to the distorted resonance lineshape. For large input powers, once λ_c is exceeded by λ_s , the succeeding temperature increase in silica allows λ_c to increase and catch up with λ_s . The cycle repeats and leads to oscillations in the transmission spectra. From Eq. (3.23), higher input power can provide larger temperature increase in the cavity, and thus sustain more oscillation cycles as demonstrated in Figure 3.10. In the measurement, a threshold power of 1.33 mW is observed to obtain oscillations in the transmission.

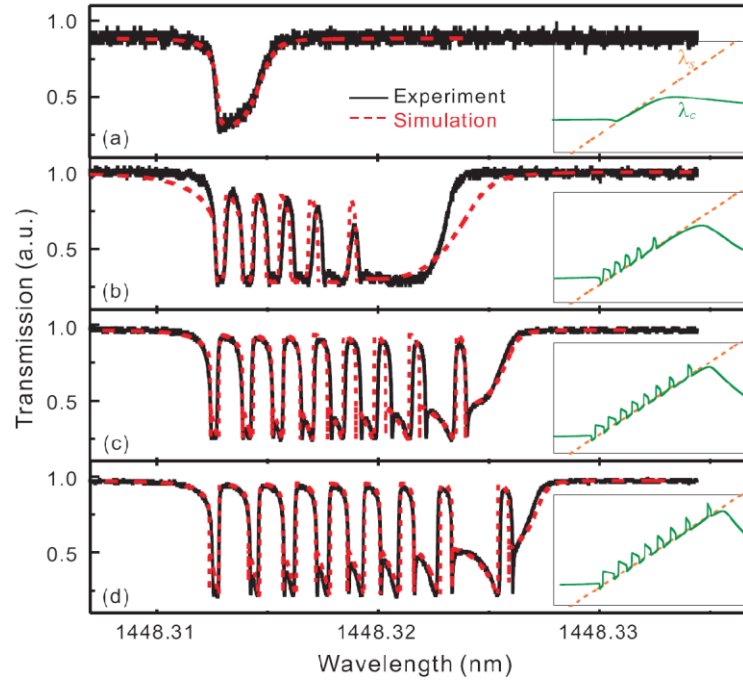


Figure 3.10 Experimental (black solid lines) and numerical simulation (red dashed lines) results of the transmission spectra at input powers of 1.11 mW (a), 1.98 mW (b), 3.15 mW (c), and 4.04 mW (d), respectively. The wavelength scanning speed is 40 nm/s. Insets: Simulation results of scanning wavelength λ_s (orange dashed lines) and resonance wavelength λ_c (green solid lines).

Figure 3.11 investigates the influence of the taper-cavity air gap on the oscillation behavior. Since the air gap determines the taper-cavity coupling, it has similar effects on the transmission spectrum as the input power. In the under coupling region (Figure 3.11(a) and (b)), reduced air gap increases the power coupled into the cavity, thus resulting in more oscillation cycles. In the over coupling region (Figure 3.11(c)), the total Q factor decreases and the resonance linewidth is broadened due to the large coupling loss. The transmission decreases slowly at the beginning of the resonance. Thus, the thermal effect has enough time to manifest itself in silica and PDMS. Since the PDMS layer is not sufficiently thick to compensate for the thermal effect in silica, a red shift of λ_c is expected. Figure 3.11(c) demonstrates that at the beginning of the mode, silica induced resonance red shift dominates and no oscillation is observed. As $\Delta\lambda$ decreases, temperature in PDMS increases quickly, inducing oscillations in the transmission spectrum. When the air gap becomes even smaller (approaching the deep over coupling region), the thermo-optic effect of PDMS can never compete with that of silica as

shown in Figure 3.11(d). Thermal effect of silica dominates in the whole thermal drift area, and causes a continuous red shift of λ_c . Therefore, no oscillation appears in the transmission spectrum.

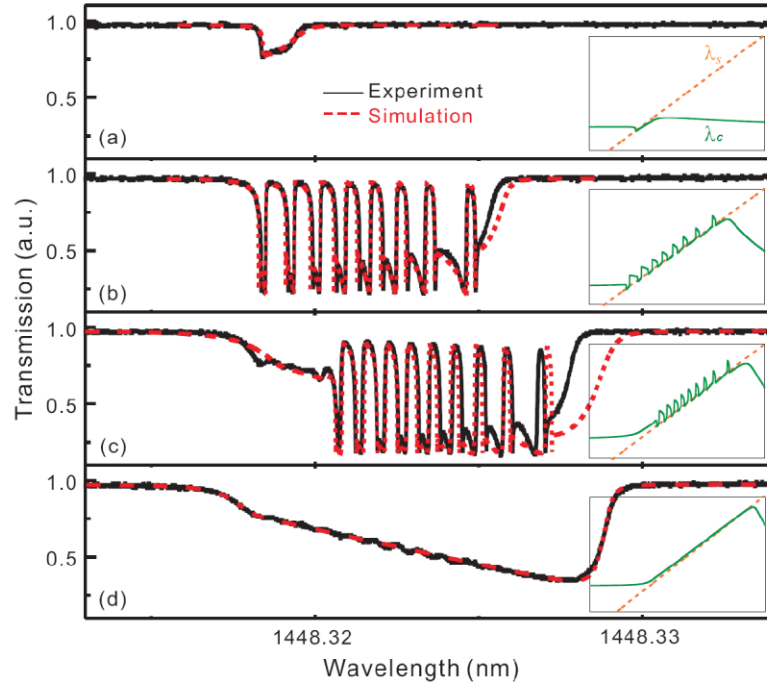


Figure 3.11 Experimental (black solid lines) and numerical simulation (red dashed lines) results of the transmission spectra for taper-cavity gap of 0.8 μm (a), 0.4 μm (b), 0.2 μm (c), and 0 (d), respectively. The transmission is measured at an input power of 3.91 mW and wavelength scanning speed of 40 nm/s. Insets: Calculated λ_s (orange dashed lines) and λ_c (green solid lines).

Figure 3.12 depicts the effect of wavelength scanning speed on the transmission spectra obtained in the under coupling region. As the scanning speed increases, the number of oscillation cycles decreases. This is because for a larger scanning speed, the laser wavelength scans through the resonant mode at a higher speed, resulting in a shorter material absorption time and a smaller temperature increase in the mode volume. This leads to a narrower resonance region and thus fewer oscillation cycles. In addition, at a higher scanning speed, the red shift of λ_c in region III (marked in Figure 3.9(d)) needs longer time to keep up with the up scan of λ_s , leading to a broader dip in each cycle and fewer cycles in the whole thermal drift area. In Figure 3.12(c), the WGM experiences

only regions I and II. In region III, the red shift of λ_c cannot catch up with the fast wavelength up scan, resulting in one sharp dip in the transmission spectrum.

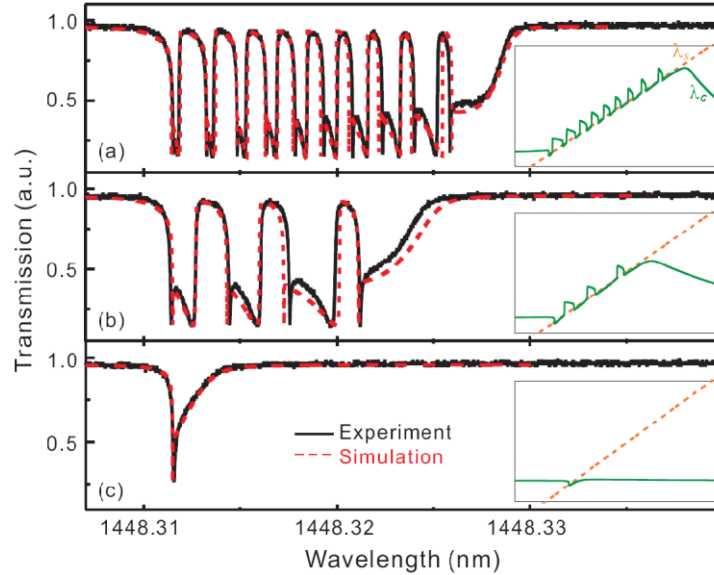


Figure 3.12 Experimental (black solid lines) and numerical simulation (red dashed lines) results of the transmission spectra at wavelength scanning speed of 40 nm/s (a), 80 nm/s (b), and 120 nm/s (c), respectively. The input power is 3.91 mW. Insets: Calculated λ_s (orange dashed lines) and λ_c (green solid lines).

In summary, we have studied the thermal oscillations in the transmission spectrum of a PDMS coated silica microtoroid. The input power, taper-cavity coupling efficiency, and wavelength scanning speed are demonstrated to dramatically affect the oscillation behaviors. Numerical simulation results agree well with the experimental measurements. The self-oscillation phenomenon may be applied for optical modulation, all-optical switching, and optical memory elements.

It should be noted that such oscillations also exist in time domain. For example, when the laser input is fixed at the resonance wavelength, the transmitted light power varies with time, as show in Figure 3.13. The repetition rate and width of the pulses change with the input power. In our measurements, similar oscillations were also observed in PMMA and PS coated microtoroids.

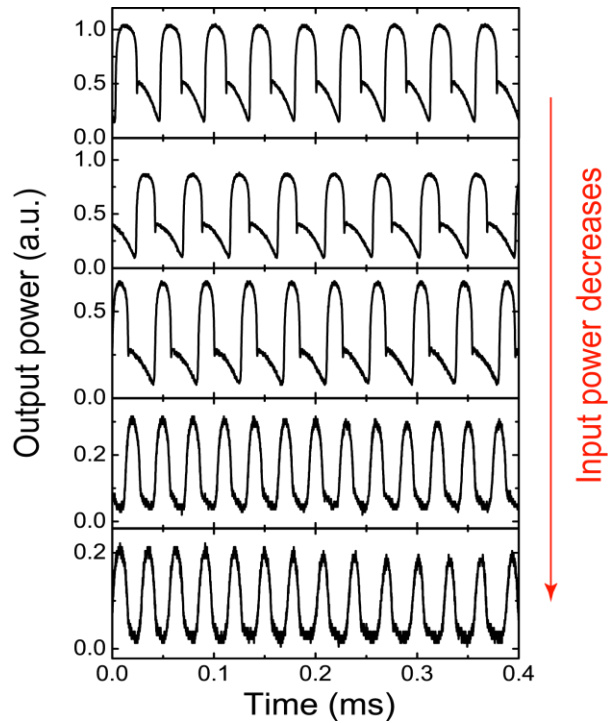


Figure 3.13 Power oscillations of the transmitted light with time from a PDMS coated silica microtoroid.

3.4 Applications of Polymer Coated Resonators

Polymer and polymer coated resonators have been utilized to detect bio-molecules, chemicals, temperature, humidity, ultrasound wave, and mechanical force [38,76-80]. Such resonator based sensing techniques count on monitoring the frequency shifts of the resonant modes, which result from changes in the refractive index of the resonant mode or deformation of the polymer structure. Enhanced sensitivity of resonator based biosensors has been demonstrated by coating the resonator with a thin layer of high refractive index polymer, which enhances extension of the evanescent field into the surrounding medium [74,77].

In addition to fully compensate the thermal effect in a resonator [56,60], polymer coating can also be used to control the cavity thermal response. WGMs in a polymer

coated resonator have distinct thermal response, i.e., red shift or blue shift with temperature, depending on the ratio of the light energy traveling in the resonator core and in the coating layer. As a result, two resonant modes in a single microcavity, which are originally separated in the spectrum and show different thermal response, can experience different frequency shifts with the same temperature variation and be tuned on resonance simultaneously. The different resonance tuning rates provide an easy way to obtain two resonant modes with the same resonance. Based on this method, electromagnetically induced transparency-like effect has been observed in a single PDMS coated resonator [81].

Chapter 4

Microcavity Lasers

Since the realization of the first laser in 1960 using ruby as the active material [82], many active media, i.e., materials that can generate optical gain such as semiconductors, quantum dots (QDs), organic dyes, organic polymers, and rare-earth metal ions, have been studied for their suitability for lasing. Meanwhile, a large variety of cavity configurations have been developed and implemented to decrease cavity losses and to improve light amplifications [7-8,18]. Lasing wavelength, spectral width of the lasing line, and lasing threshold are fundamental parameters to characterize a laser. These parameters depend on the cavity Q factor and the mode volume V . A large Q/V ensures strong coupling between the cavity field and the active material [83-84], implying the possibility of realizing low threshold and narrow linewidth lasers. WGM microresonators have been demonstrated as excellent candidates for constructing low threshold and narrow linewidth lasers, thanks to their high Q factors and small mode volumes. In this chapter, we first introduce various WGM microcavity lasers and then introduce our work on rare-earth ions doped microtoroid lasers [85].

4.1 Introduction

Lasing in WGM resonators can be achieved by either introducing active materials to the resonator or using intrinsic nonlinearities of the resonator material [12,86-90]. Combination of high- Q resonators and different gain materials leads to a variety of laser configurations covering a wide lasing spectral range from ultraviolet to infrared.

For example, for liquid droplet resonators, gain material can be easily dissolved in the droplets. Laser emission in liquid droplets was first observed in Rhodamine 6G (R6G)

doped ethanol droplets with diameter of 60 μm pumped by a continuous-wave argon laser. The threshold pump intensity was approximately 35 W/cm^2 [91]. For easy manipulation, dye doped liquid droplets have been generated in microfluidic channels for lasing application [92]. In Ref. [86], laser action was obtained from a silica microsphere formed by heat-fusing the tip of a neodymium (Nd^{3+}) doped silica wire. For a cold cavity Q factor of 2×10^8 , the absorbed pump power at lasing threshold was measured as low as 200 nW for resonant pumping. Shopova *et al.* reported laser emission in the range 1240~1780 nm from HgTe QDs coated silica microspheres of diameter 950 μm with threshold pump powers less than 2 μW at 830 nm [87]. Cao *et al.* achieved lasing in InAs QDs embedded GaAs microdisks [93]. For a 3 μm microdisk at 77 K, lasing in the range of 945~1005 nm with threshold around 20 μW was observed when the QDs were pumped with a continuous-wave HeNe laser at 633 nm. In Ref. [94], R6G doped PMMA conical cavities were used to generate laser emission at 600 nm. For a pump pulse duration of 15 ns and repetition rate of 5 Hz, lasing thresholds as low as 3 nJ/pulse and narrow laser linewidths of 50 pm were observed.

Among different gain materials, rare-earth ions (e.g., Er^{3+} , Yb^{3+} , Nd^{3+} , etc) are popular dopants for solid-state lasers due to their high efficiency, long upper-level lifetime, ability to generate short pulses, and wide emission spectrum spans from 0.3 to 3 μm which cover wavelengths crucial to many sensing and communication applications, e.g., Er^{3+} ions provides gain around 1550 nm which makes it a key dopant for optical communication applications [95]. Here we take the Er-doped microtoroidal resonator as an example to investigate the performance of WGM microlasers.

4.2 Er-Doped Microtoroid Lasers

Various methods have been used to fabricate rare-earth ion doped resonators, such as directly fabricating the resonator from the doped material [86], coating the resonator with rare-earth ions [96], and doping the resonator by ion implantation [97]. Among them, sol-gel synthesis provides a convenient way to tailor the dopants. In this section,

we describe the preparation of Er-doped toroidal resonators from sol-gel silica films, characterize the lasing performance, and investigate the dependence of lasing threshold on various resonator parameters.

4.2.1 Sol-gel Fabrication of Er-Doped Silica Microtoroids

Sol-gel method is a low-cost, fast, and flexible wet-chemical synthesis technique for preparation of glasses and ceramics. The sol-gel process is based on hydrolysis and condensation reactions of metal-alkoxide precursors in aqueous solution, alcohol, or other medium [98-99]. The reaction is performed under either acid or base catalyzed condition to obtain dense films. We use the sol-gel process under acid catalyzed condition to prepare silica thin films on silicon substrates from which silica toroidal resonators are fabricated. The process for synthesis of silica films can be divided into three steps: 1) Hydrolysis, Si-alkoxide is hydrolyzed by water molecules to produce a colloidal suspension (sol); 2) Condensation, hydrolyzed molecules produce Si-O-Si linkages or networks (gel); 3) Annealing, the silica-gel film is treated at high temperature to form dense glass. Dopants can be introduced into sol-gel materials by mixing relevant soluble chemicals in the precursor solutions. For example, in our experiments erbium nitrate ($\text{Er}(\text{NO}_3)_3$) is used to introduce Er^{3+} ions. The advantages of doping active medium via sol-gel technique include controllable dopant concentration, wide choice of material matrices, and flexibility and ease of adding multiple dopants.

Figure 4.1 is a flow chart showing the preparation of silica sol-gel films and the fabrication of silica microtoroids [12,27,90]. First, the sol-gel precursor solution is prepared in a Teflon beaker by mixing tetraethoxysilane (TEOS) in isopropanol alcohol (IPA) and water (H_2O) with hydrochloric acid (HCl) as catalyst. The weight ratio of IPA, H_2O , TEOS, and HCl is 6.5:0.7:0.6:6.1. Rare-earth compound (e.g., $\text{Er}(\text{NO}_3)_3$) of specific amount is mixed to the solution for desired dopant concentration. Subsequently, the solution is stirred with a magnetic bar at 500 rpm for 3 hours at 70°C . Hydrolysis and condensation take place during this process. Afterwards, the solution is aged at room temperature for 24 hours. The aged solution is then spin-coated on a silicon wafer

at 3000 rpm for 30 seconds to form a uniform layer. The coated film is heat treated in a tube furnace at 1000°C for 3 hours to remove the residual solvent, transferring porous silica to dense glass. Then the wafer is let cool down to room temperature naturally. Finally, a uniform and smooth silica film is obtained on the silicon substrate. The concentration of Er^{3+} ions in the silica film is tailored by controlling the amount of $\text{Er}(\text{NO}_3)_3$ in the sol-gel precursor solution. The film thickness after annealing depends on the dopant concentration and the spin coating condition. In our experiments, the thickness of one coating layer varies in the range of 350~500 nm. Desired film thickness can be achieved by applying multiple coating layers. For example, Figure 4.2 shows the SEM image of a three-layer silica film on a silicon substrate.

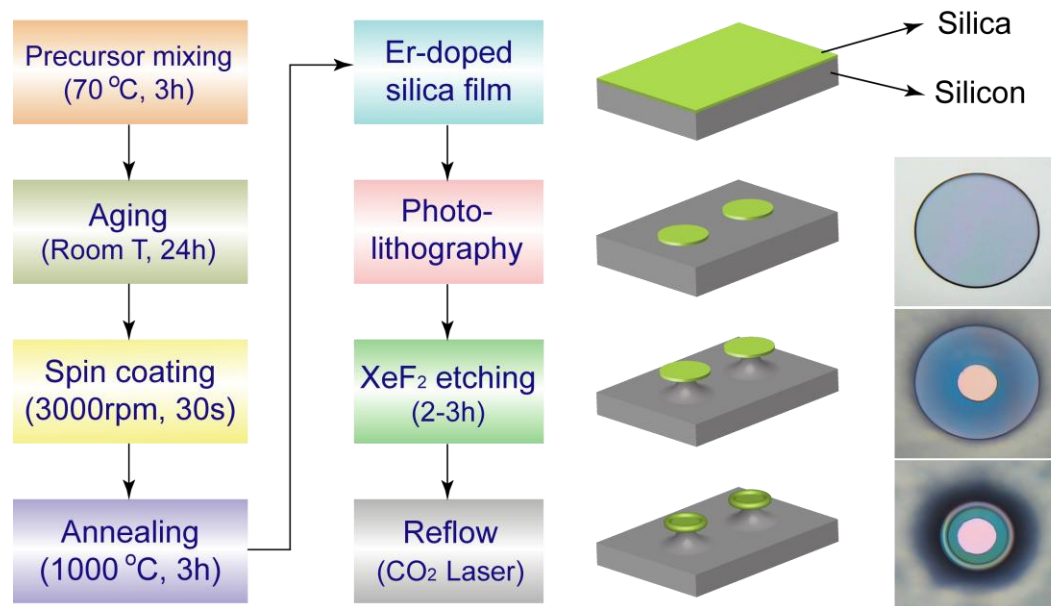


Figure 4.1 Fabrication flow of Er-doped microtoroids through sol-gel process and photolithography technique. The right two columns show the illustrations and optical micrographs of the microdisk, under-cut microdisk, and microtoroid.

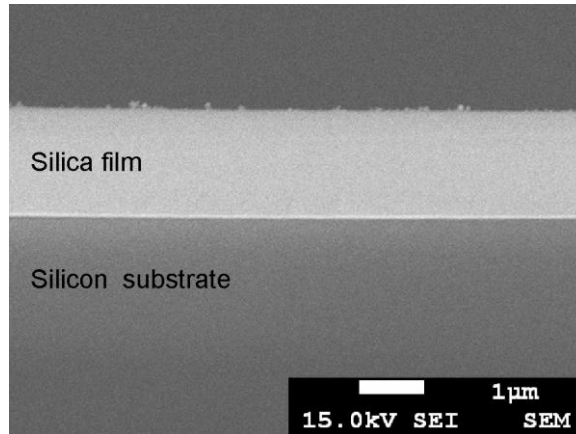


Figure 4.2 SEM image of silica sol-gel film coated on a silicon substrate. The coating was repeated three times to obtain the film thickness around 1.5 μm .

Active microtoroids are fabricated from Er-doped silica films through a standard process of photolithography, XeF_2 etching, and CO_2 laser reflow. The resulting patterns after each step are shown in the right column of Figure 4.1. We tested the Q factors of the microtoroids with Er^{3+} concentrations in the range of $10^{18} \sim 2 \times 10^{19}$ ions/ cm^3 in 1460 nm wavelength band. At each concentration, multiple measurements were performed on a few microtoroids and the highest Q is plotted in Figure 4.3. As the dopant concentration increases, the total cavity losses increase due to light absorption of Er^{3+} ions, leading to a reduced Q factor.

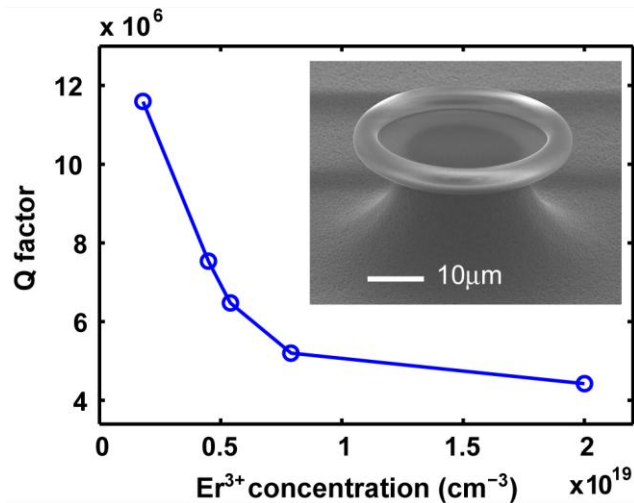


Figure 4.3 Measured Q factors of Er-doped microtoroids for different dopant concentrations. Inset: SEM image of a doped microtoroid.

4.2.2 Laser Characterization

The experimental setup used to characterize the microtoroid laser is shown in Figure 4.4 [85]. A continuous-wave light source in 1460 nm or 980 nm band is used to pump the cavity. A tapered fiber is used to couple light into and out of the resonator, with the coupling efficiency tuned by adjusting the gap between the taper and the resonator. A polarization controller (PC) is used to adjust the polarization state of the pump beam to optimize the coupling efficiency. The light coupled out of the resonator is connected to a 10/90 fiber coupler, with the 10% port connected to an optical spectrum analyzer (OSA) to record the lasing spectrum, and the 90% port directed to a fiber based wavelength division multiplexer (WDM) to separate the laser emission in 1550 nm band from the unabsorbed pump light. Both outputs of the WDM are monitored by photodetectors, the outputs of which are sent to an oscilloscope connected to a computer for data acquisition and processing. Within the resonator, laser emission takes place and propagates along both forward and backward directions (i.e., a WGM resonator supports two counter-propagating modes. Here, forward denotes the clockwise and backward denotes the counter-clockwise propagating light). Laser emission couples out from both ends of the fiber taper. In our experiments, for simplicity, we measure the lasing output transmitted in the forward direction.

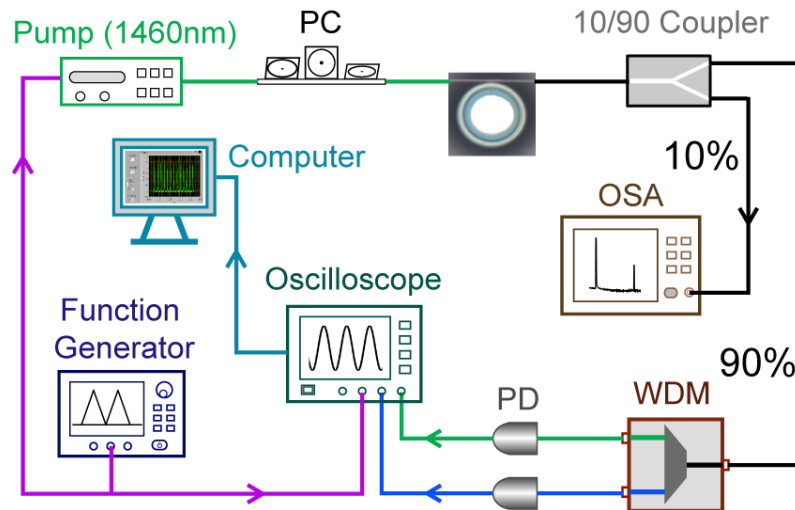


Figure 4.4 Schematic of experimental setup. PC: polarization controller, OSA: optical spectrum analyzer, WDM: wavelength division multiplexer, PD: photodetector.

In the experiments, the wavelength of the pump laser is tuned on resonance with a high Q cavity mode to achieve resonant pumping. Near the resonant wavelength, small input pump power is significantly enhanced inside the cavity to efficiently excite the Er^{3+} ions. Figure 4.5 shows the typical lasing spectrum and the laser threshold measurement. Spectral width of the laser line is much narrower than the resolution of our OSA (0.1 nm) and cannot be resolved [100]. From the linear relation between the pump and the laser output in Figure 4.5(b), the threshold pump power is around 12 μW [85].

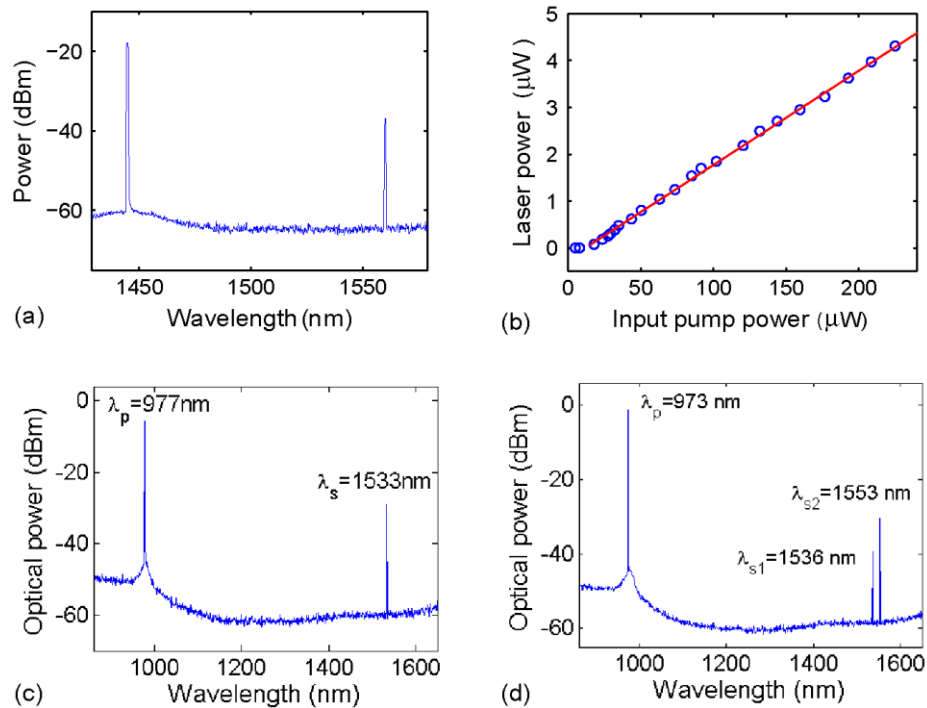


Figure 4.5 Lasing characterization of an Er-doped microtoroid. (a) Lasing spectrum showing pump at 1445 nm and lasing at 1560 nm. (b) Measurement of laser output versus input pump power. Lasing spectra for 980 nm band pumping showing single-mode (c) and two-mode (d) lasing.

4.2.3 Time Domain Laser Operation

Research on Er-doped fiber lasers revealed that laser operation under continuous pump condition can be continuous wave or self pulsation (SP) depending on the Er^{3+} concentration in the host matrix [90,101-102]. Here SP operation refers to spontaneous self pulsation in which the lasing signal appears as an infinite pulse train. It was

demonstrated in fiber lasers that, for low (high) Er^{3+} concentrations, the laser output intensity was continuous wave (self pulsation) for any pumping rate. For concentrations in between, the output intensity varied from self pulsation to continuous wave when increasing the pump power. Generation of self pulsation is attributed to the ion-ion interactions in Er^{3+} clusters. As ion concentration increases, average distance between the ions decreases. This enhances the ion-ion interactions and leads to so called ion pairs, in which cooperative energy transfer between ions occurs. For example, when two adjacent ions are excited to state $^4\text{I}_{13/2}$, one transfers its energy to the other one and decays to the ground state $^4\text{I}_{15/2}$ non-radiatively, while the other ion is upconverted to $^4\text{I}_{9/2}$ where it mostly relaxes to $^4\text{I}_{13/2}$ non-radiatively. The net effect is the loss of one excited ion, i.e., loss of one potential stimulated photon. In other words, the paired ions inside the resonator act as saturable absorbers or as an additional loss mechanism, giving rise to self pulsation [103-104].

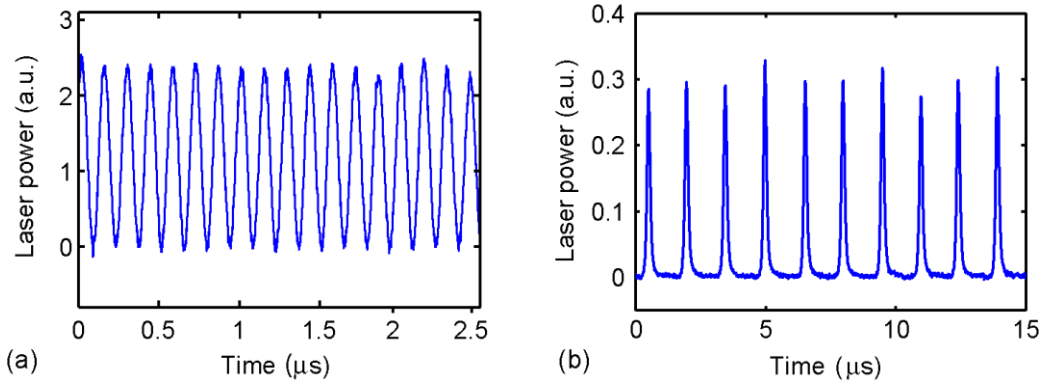


Figure 4.6 Laser output in time domain from Er-doped microtoroids. (a) Continuous-wave operation measured from a microlaser with Er^{3+} concentration of $\sim 5 \times 10^{18} \text{ cm}^{-3}$. The laser power fluctuation at frequency 6.7 MHz is attributed to the beating of the split laser modes [105]. (b) SP operation with pulse width $\sim 130 \text{ ns}$ and pulse repetition rate $\sim 680 \text{ kHz}$ measured from a microtoroid laser with Er^{3+} concentration of $2 \times 10^{19} \text{ cm}^{-3}$.

We observed and reported similar behaviors in Er-doped microtoroidal lasers [85,105]. For input pump powers less than 2 mW, the microlaser operates in continuous-wave regime (Figure 4.6(a)) for Er^{3+} concentrations below $7 \times 10^{18} \text{ cm}^{-3}$ and in SP regime (Figure 4.6(b)) for Er^{3+} concentrations above 10^{19} cm^{-3} . In between, both continuous-wave and self-pulsing operations can be obtained by controlling the intracavity pump power, e.g., changing the input pump power, adjusting the taper-cavity gap, or exciting

the pump modes of different Q factors. This is because the pumping rate in the cavity depends on the intracavity pump power which is a function of the taper-cavity coupling, the Q factor of the pump mode, and the input pump power. They, in return, can be used to control the laser operations. For example, Figure 4.7 shows the laser operation changing from continuous wave to self pulsation when the taper-cavity gap is reduced.

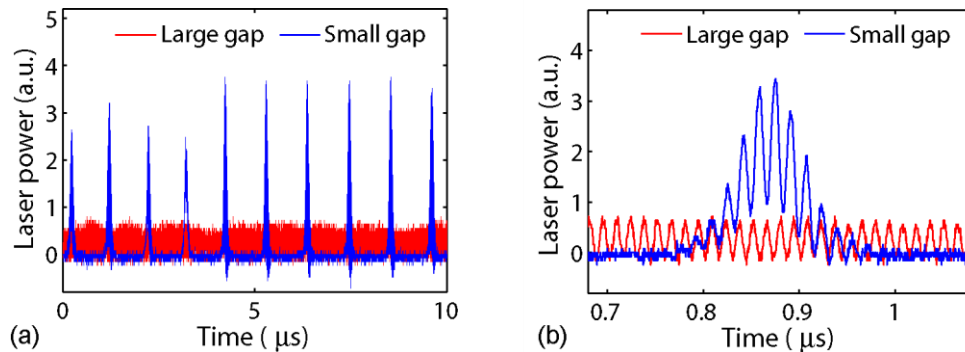


Figure 4.7 Laser power output at different taper-cavity coupling conditions with the same input pump power. The concentration of Er^{3+} ions is 10^{19} cm^{-3} . (a) For a large taper-cavity gap, continuous-wave lasing is obtained (red curves). When reducing the gap, self-pulsing laser emission occurs (blue curves). (b) Close-up of the laser emission in (a). The laser power fluctuations are due to laser mode splitting.

Continuous-Wave Laser Emission

Interestingly, in Figure 4.6(a), the laser power shows a sinusoidal oscillation instead of a constant output. Such oscillation is not observed for the unabsorbed pump light. We have demonstrated that the laser power oscillations are due to splitting of the laser mode induced by Rayleigh back-scattering from the defects or contaminants in the laser cavity [105-107]. Briefly speaking, coupling of the counter-propagating modes in the cavity via back-scattering lifts the mode degeneracy. As a result, the lasing mode splits into two. The two lasing frequencies, when detected by a photodetector, interfere and lead to a beat note signal which is observed in Figure 4.6(a).

Self-Pulsing Laser Emission

We observed in Figure 4.6(a) that the continuous-wave laser power was modulated by a beat note signal resulting from mode splitting. However, in Figure 4.6(b), we did not observe similar oscillations in the pulse train. This is because the period of the beat note was longer than the pulse duration. For a larger frequency splitting, where the beat note

period is smaller than the pulse width, the effect of mode splitting shows up as depicted in Figure 4.8.

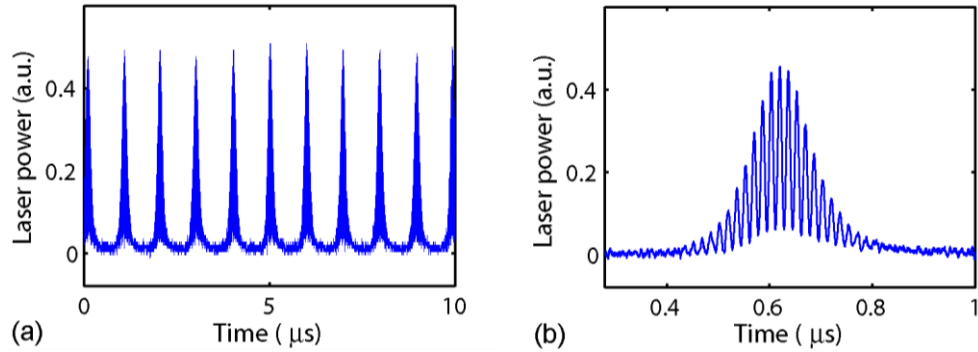


Figure 4.8 (a) Self-pulsing laser operation in the presence of mode splitting in the laser cavity. (b) Close-up of (a) for a single pulse. The pulse is modulated at frequency 62 MHz.

Figure 4.9 presents the transmission spectra of the pump and laser light acquired from the oscilloscope. The pump spectrum shows mechanical oscillation with frequency around 30 MHz [108-109]. However, the laser pulse is not disturbed by the mechanical oscillation. This can be interpreted as follows. Optical force induced radiation pressure changes the resonator shape periodically as well as the optical path and the resonance wavelength. As a result, the wavelength detuning changes and the pump transmission varies accordingly, leading to the power oscillation. Since laser emission occurs at the resonance wavelength of the cavity, the lasing wavelength might show fluctuations due to the mechanical oscillation, however, the laser power will not change a lot.

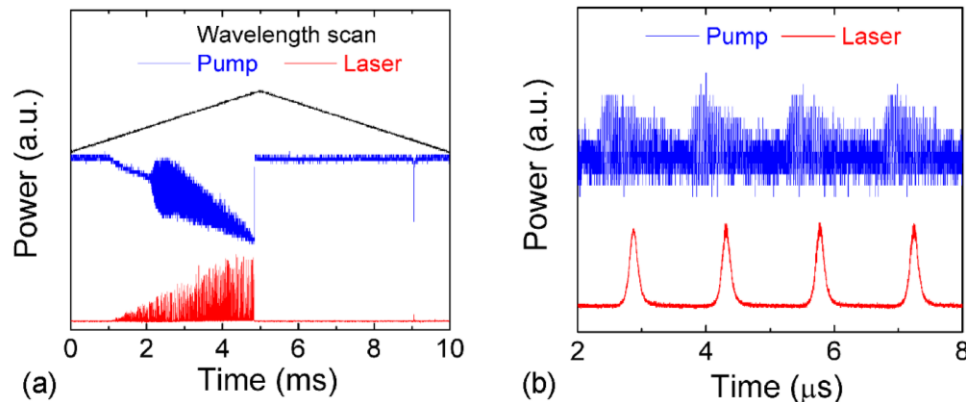


Figure 4.9 (a) Transmission spectra of the pump and laser light when the pump wavelength is scanned at a speed of 42 nm/s. The black triangle denotes wavelength up scan and down scan. The broadened resonant mode during wavelength up scan is attributed to thermal effect in the cavity. (b) Zoom-in plot of (a).

In the rest of this section, we discuss in detail the formation of pulse lasing in heavily Er-doped microlasers and investigate the dependence of the pulse repetition time and pulse width on the pump power and the taper-cavity coupling condition. The microtoroids used in the experiments have major (minor) diameter of 40 μm (5 μm) and Er^{3+} concentration of $2.2 \times 10^{19} \text{ cm}^{-3}$ [85].

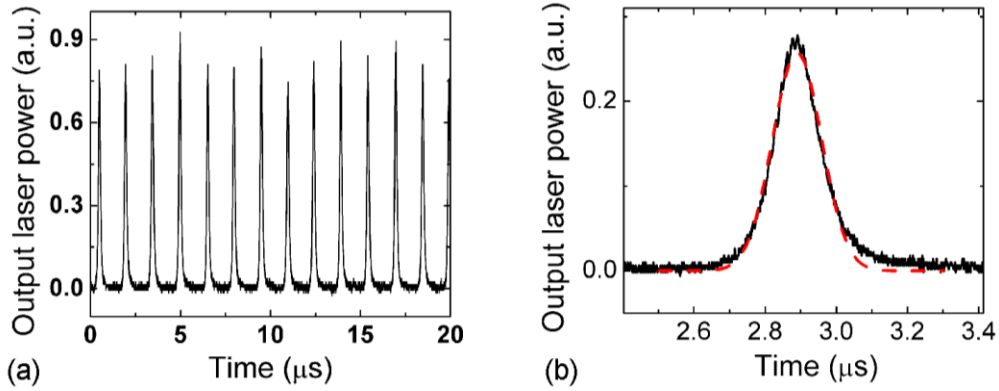


Figure 4.10 (a) Observed laser pulse train from an Er-doped microtoroid when the pump is fixed at the resonance wavelength. (b) Gaussian fitting (red dashed curve) of a single laser pulse.

Figure 4.10 depicts the measured laser pulse and Gaussian fitting of a single pulse. In heavily doped cavities, clusters of Er^{3+} ions cause a large excited state absorption due to energy transfer among paired ions which is responsible for the pulse laser [103-104]. In the pumping process, as more ions are excited to the higher energy level, energy transfer between paired ions increases, leading to an increase in the total loss of the cavity system (i.e., cavity loss and excited state absorption loss). As a result, a large population inversion is built up and more energy is stored in the gain medium. As soon as the gain exceeds the total loss, lasing starts and laser intensity rapidly builds up in the cavity because of the large amount of energy stored in the gain medium. Subsequently, the number of ions in the excited state decreases. This decreases the total loss of the cavity due to the reduced excited state absorption. As the pump continuously replenishes the population inversion, lasing output keeps increasing as shown in the rising side of the pulse until the saturation of the gain. Subsequently, lasing output reaches its peak and starts to decrease, which slows down the reduction of ions in the excited state and consequently increases the chances of excited state absorption. As a result, the lasing

output decreases further as the excited state absorption loss increases. The reduction of laser intensity continues until the lasing photons are consumed. With the pump continuously exciting the system, another cycle starts. This process repeats to generate an infinite laser pulse train. The pulse performance depends on the pumping rate within the cavity which affects the population inversion and the laser oscillation process. In Figure 4.10, fluctuations in the peak power of the pulses might originate from thermal effects, mechanical oscillations, perturbations in the pump power, and the fact that population inversion density may not return to the same value each time the cavity dumps out the pulse.

To study the effect of pump power on the laser pulses, we monitor the changes in the pulse train in response to variations in the launched pump power. The taper-cavity gap is adjusted close to critical coupling to maximize the pump power coupled into the cavity. To minimize the influence of environmental noises, the laser pulses are collected repeatedly using a LabVIEW program for hundreds of times at each pump power for analysis. Figure 4.11 shows that the pulse period (T_p), and pulse width ($\Delta\tau$, FWHM) decrease with increasing pump. This can be explained as follows. At a higher pump power, the recovery of population inversion is achieved faster due to the higher pumping rate. Thus the time interval between the end of a pulse and the start of the consecutive pulse, which is the time needed to create population inversion for lasing, is shorter. During the pulse generation, a higher pumping rate leads to a faster growth of net gain and thus a faster buildup of the pulse. The measured laser pulse in our experiments is symmetric, indicating that the fall time is close to the rise time. This is because similar mechanisms, such as coupling condition, pumping rate, and cavity losses, affect both the growth and decay rate of the net gain, which determine the rise time and fall time of the pulse. Therefore, for a fixed taper-cavity coupling, increasing pump power leads to decrease in T_p and $\Delta\tau$.

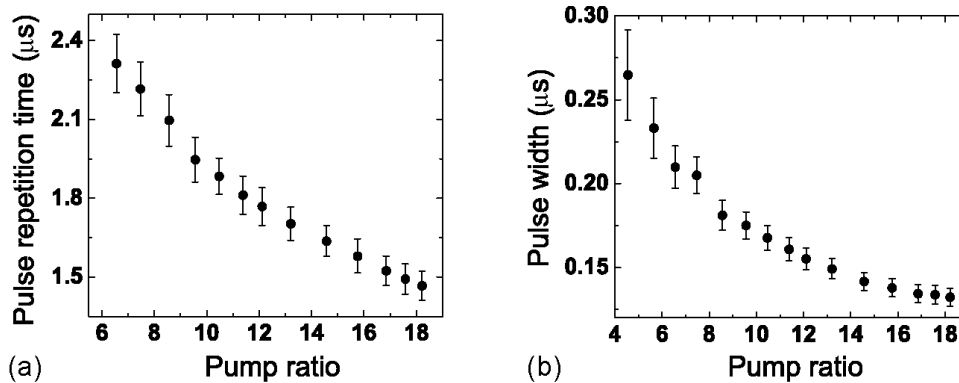


Figure 4.11 Dependence of pulse repetition time (a) and pulse width (b) on the input pump power. Pump ratio denotes the input pump power normalized by the threshold pump power. Data points and error bars represent the mean and standard deviation of multiple measurements.

Figure 4.12 shows the effect of taper-cavity coupling on the pulse train. Coupling between the fiber taper and the cavity decreases as the taper-cavity gap increases. At the critical coupling point of the pump light (i.e., minimum pump transmission), the intracavity pump power achieves its maximum, leading to minimized T_p and $\Delta\tau$. In the under coupling regime, as gap decreases, both T_p and $\Delta\tau$ decrease monotonously until the critical coupling point. Further decrease of the gap to over coupling regime leads to increasing T_p and $\Delta\tau$. In Figure 4.12(b), $\Delta\tau$ is longer in the over coupling regime than that in the under coupling regime for identical pump transmission. This is because in the over coupling regime, laser photons generated from stimulated emission are extracted from the cavity at a higher rate due to the stronger taper-cavity coupling. This leads to a slower buildup rate of the laser pulse within the cavity and thus a longer $\Delta\tau$.

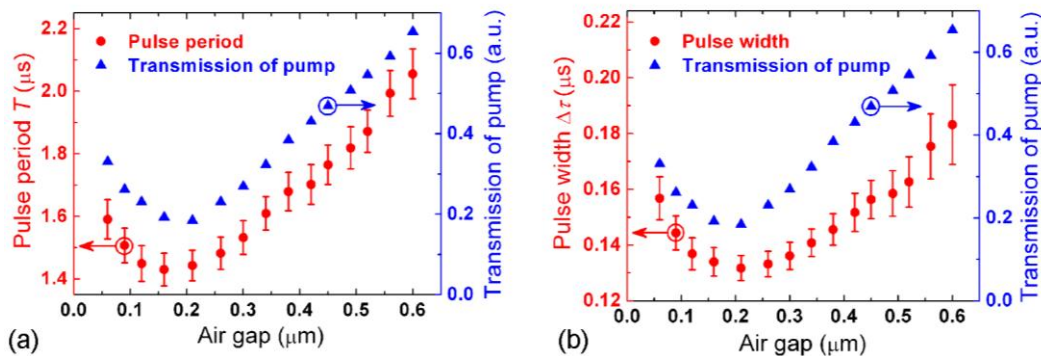


Figure 4.12 Dependence of pulse period (a) and pulse width (b) on the taper-cavity gap. Blue triangles are cavity loading curve for the pump mode, i.e., pump transmission versus gap. Data points and error bars denote the mean and standard deviation of multiple measurements.

4.2.4 Maximum Laser Power Output

Laser power coupling out of a laser cavity is determined by the output coupling coefficient and the circulating laser power within the cavity [110]. In our experiments, the same fiber taper is used to couple light in and out of the microlaser. Thus, the coupling condition which is optimized for the pump light may not be the optimal condition for extracting the laser light from the cavity and vice versa. In general, the coupling condition will affect (i) the pump-cavity coupling efficiency and hence the intracavity pump power, and (ii) the coupling loss experienced by the lasing mode which determines the lasing threshold and the extraction rate of the laser power from the cavity. Therefore, the maximum laser power output does not necessarily coincide with the critical coupling point of the pump light. The optimum laser output and the corresponding coupling condition depend on the taper size, field distributions of the pump and the laser modes, and the intrinsic cavity loss. The situation should be considered case-by-case for each individual microlaser [111]. Our measurement results in Figure 4.13 show the pump transmission and the laser power output as a function of the taper-cavity gap for continuous-wave and self-pulsing operations, respectively. In these measurements, the maximum laser output occurs in the over coupling regime of the pump light.

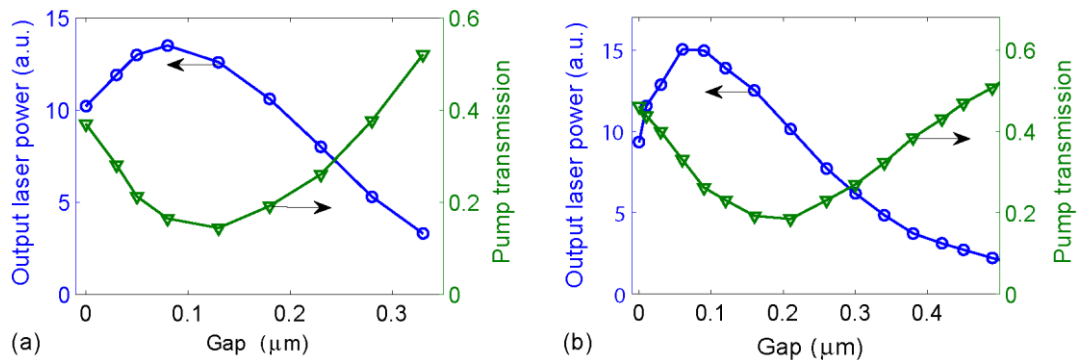


Figure 4.13 Laser power output versus taper-cavity gap for continuous-wave (a) and self-pulsing (b) laser operations. The circles denote the laser power output, and the triangles represent the normalized transmission for the pump light. The laser power in (b) is the peak power of the pulses.

4.2.5 Lasing Threshold

Laser threshold is achieved when the small-signal gain generated from the excited active medium equals the total loss of the resonator system [110,112]. Below the threshold, optical gain increases linearly with the intracavity pumping power, which depends on the input pump power, cavity Q factor, and taper-cavity coupling strength. The value of the gain is also closely related to the size of the resonator and the dopant concentration. In the following discussion, the dependence of the threshold pump power on those parameters is considered.

In general, high Q factor is preferred to reduce the lasing threshold. In a microlaser cavity, pumping rate R_p is proportional to the ratio of the intracavity pump power P_c to the mode area A , i.e., $R_p \propto P_c/A$. For a fixed input power, P_c is proportional to the Q factor. A higher cavity Q factor results in a longer photon lifetime in the resonator and more light energy stored in the cavity. Therefore, the higher the cavity Q , the higher the pumping rate and thus the smaller the lasing threshold [111].

The taper-cavity coupling strength has a two-fold effect on the lasing threshold, since it affects both the pump and laser modes. On one hand, the coupling strength affects the intracavity pump power and thus the pumping rate. On the other hand, the coupling strength has impact on the total loss experienced by the laser photons. The threshold increases in the over coupling regime due to the increased coupling loss, and in the under coupling regime due to the inefficient pump coupling from the fiber taper to the cavity [111,113].

The cavity size affects the lasing threshold through the mode area. As the cavity size shrinks, the mode is more confined in the resonator giving rise to a smaller mode area [47-48]. This leads to an increased intracavity light intensity and thus a reduced threshold pump power. As shown in Figure 4.14(a), the mode area decreases as the microtoroid major and minor diameters decrease. When the microtoroid diameter is larger than 22 μm , high cavity Q ($>10^8$) can be maintained as shown in Figure 4.14(b).

Below 22 μm , the Q factor decreases substantially due to the increased radiation loss, setting a practical limit on the size of microlasers. To shrink the cavity size as well as the mode volume, one can fabricate the laser cavity with host materials of larger refractive indices [114], integrate a photonic crystal structure with the cavity to use the forbidden band for light confinement [115], or introduce metallic coating on the cavity to support surface mode at the metal-dielectric interface [116-117].

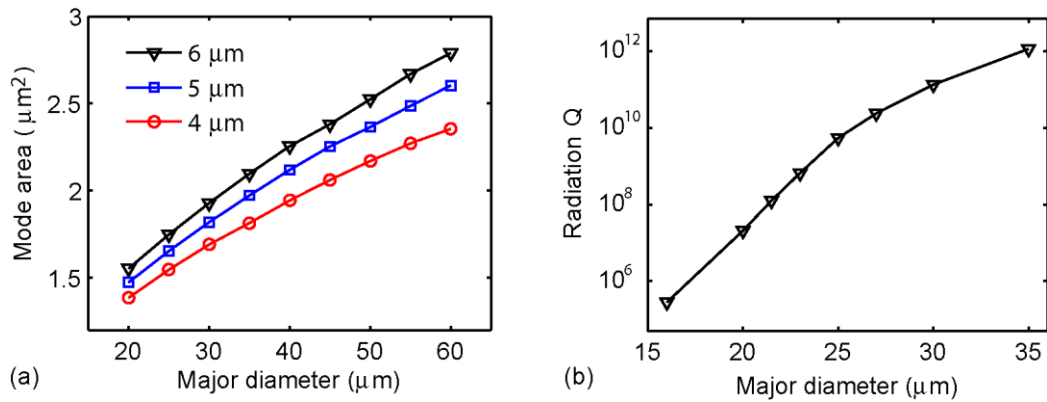


Figure 4.14 Simulation results in a microtoroid showing the mode area (a) and the radiation loss induced Q factor (b) versus major diameter of the toroid at minor diameters of 6, 5, and 4 μm .

The Er^{3+} concentration directly influences the optical gain in the laser cavity and thus affects the lasing threshold. For a fixed cavity Q factor, there exists a minimum Er^{3+} concentration to produce enough gain to compensate for the round trip loss experienced by photons to achieve laser oscillation. The minimum concentration to observe lasing increases with decreasing Q factor. There also exists an optimal Er^{3+} concentration which gives the lowest threshold input pump power. In lower concentration limit, a higher pump power is needed to excite Er^{3+} ions in order to provide sufficient gain overcoming the total losses, leading to a higher threshold. For higher ion concentrations, excited state absorption and cooperative upconversion take place, quenching the excited ions and reducing the level of population inversion. The quenching effect reduces the pumping efficiency and thus increases the lasing threshold [111].

4.2.6 Upconversion

In heavily Er-doped silica glass, upconversion process can occur through either multi-photon absorption or energy transfer between excited ions [118-119]. For Er^{3+} ions pumped in 980 nm or 1480 nm band, green light emission due to upconversion is a common observation, which is the result of direct transition of excited ions from $^4\text{S}_{3/2}$ and $^2\text{H}_{11/2}$ levels to the ground state $^4\text{I}_{15/2}$. The simplified energy level diagrams and pumping schemes are shown in Figure 4.15(a) [120-121]. Green laser has been reported in Er-doped silica microtoroids with lasing threshold of 690 μW when pumping at 1458 nm [122]. Figure 4.15(b) shows our experimental observations of upconversion emission from an Er-doped microtoroid. Green light emission is clearly seen along the periphery of the microtoroid.

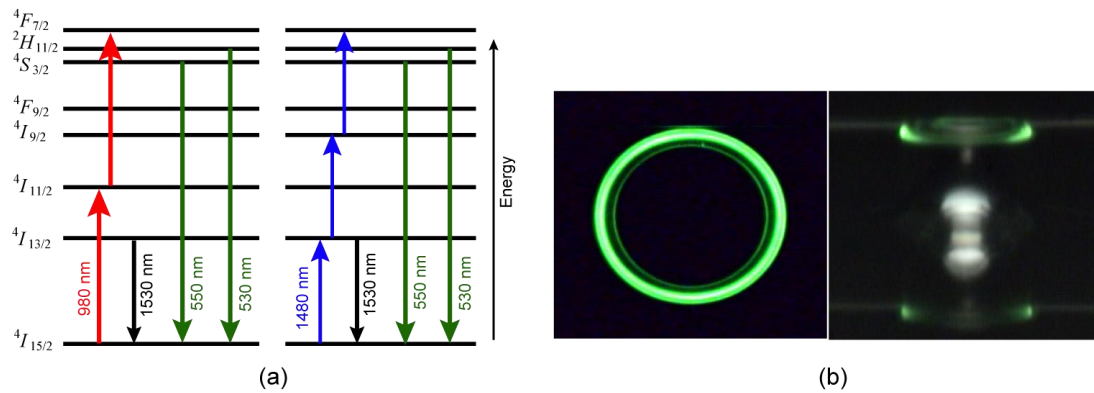


Figure 4.15 Upconversion of Er^{3+} ions. (a) Energy level diagrams of Er^{3+} in silica glass and the associated electron transition processes for generating green upconversion emission under excitation at 980 nm and 1480 nm. (b) Top and side view of green upconversion from an Er-doped silica microtoroid with Er^{3+} concentration of $2 \times 10^{19} \text{ cm}^{-3}$.

4.3 Yb-Doped Microtoroid Lasers

Using the sol-gel fabrication method, we demonstrated lasing from Yb-doped microtoroidal resonators. Figure 4.16 gives the absorption and emission spectra of Yb^{3+} ions in glass [123-125]. When pumping in 970 nm band, laser emission is generated in 1030 nm band. The Yb-doped glasses have a very simple electronic level structure, with the ground state manifold $^2\text{F}_{7/2}$ and one excited state manifold $^2\text{F}_{5/2}$. The simple

electronic structure excludes the excited state absorption and the quenching effect. The large gain bandwidth allows wide tuning of the lasing wavelength.

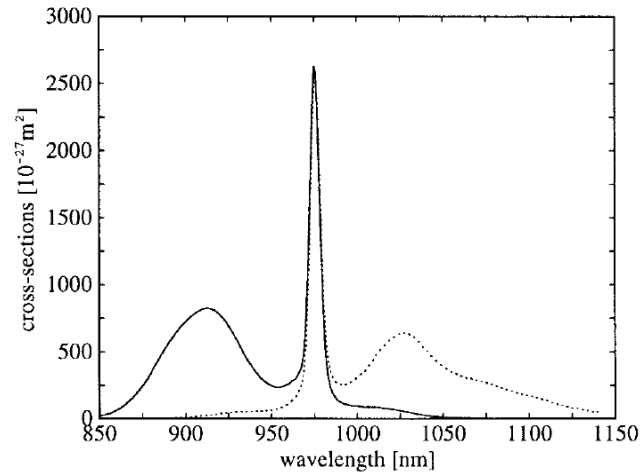


Figure 4.16 Absorption (solid) and emission (dotted) cross sections of Yb^{3+} in germanosilicate glass [123].

In our experiments, the Yb-doped microtoroids are fabricated following the process in Figure 4.1 by using ytterbium nitrate ($\text{Yb}(\text{NO}_3)_3$) as the dopant. The concentration of Yb^{3+} ions in silica is around $5 \times 10^{19} \text{ cm}^{-3}$. Figure 4.17 is the measured Q factors for an Yb-doped microtoroid at different wavelengths. The lower Q factor at 965 nm is attributed to the absorption of Yb^{3+} ions in this wavelength band.

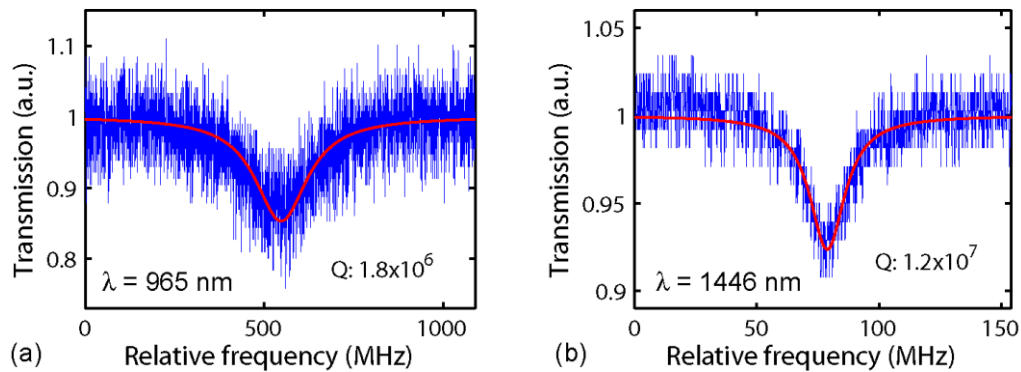


Figure 4.17 Measurement of Q factor from the transmission spectrum of an Yb-doped microtoroid at 965 nm (a) and 1446 nm (b). Red curves are Lorentzian fitting.

Figure 4.18 reveals single-mode lasing in 1043 nm. The laser-pump curve reveals a lasing threshold of $16 \mu\text{W}$. Lasing emission from Yb-doped microtoroids in water was also demonstrated [13,126]. The small absorption of water in Yb^{3+} emission band

reduces cavity losses making it possible to generate laser emission in water. We have demonstrated that microlasers in aqueous environment can be used for high-performance biosensing [13].

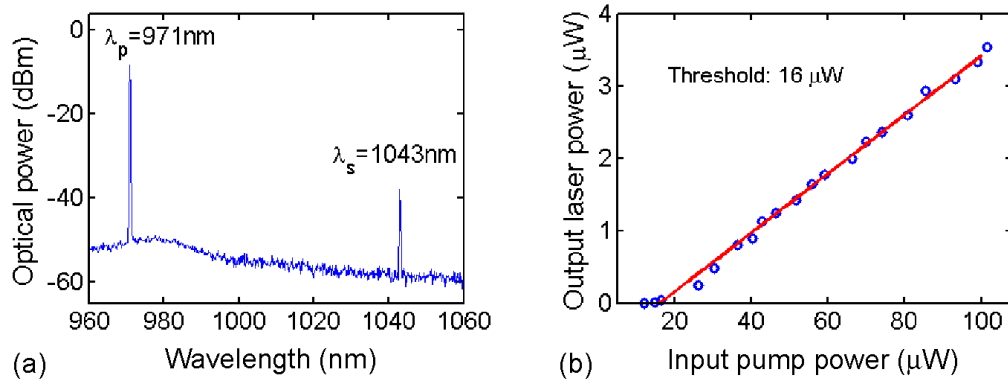


Figure 4.18 (a) Typical lasing spectrum of an Yb-doped microtoroid laser. (b) Lasing threshold measurement.

Chapter 5

Mode Splitting in Passive Resonators for Nanoparticle Sensing

There is a strong demand for portable systems that can detect and characterize individual pathogens and other nanoscale objects without the use of labels for applications in human health, homeland security, environmental monitoring and diagnostic [127-130]. However, most nanoscale objects of interest have low polarizabilities due to their small size and low refractive index contrast with the surrounding medium. This leads to weak light-matter interactions, and makes label-free detection of single nanoparticles very difficult. Microresonators have emerged as highly sensitive platforms for such applications because the combination of high Q factor and small mode volume V leads to significantly enhanced light-matter interactions. In the past few years, there have been tremendous research efforts using WGM resonators for detection and characterization of nanoscale objects [14,131-132]. The underlying principle is the change in effective refractive index or effective polarizability of the resonator-surrounding system upon the arrival of nanoscale objects in the resonator mode volume. The change leads to shift and/or splitting of the resonance frequency, which in return can be monitored to detect the nanoscale objects.

We have demonstrated that mode splitting in a silica microtoroid can be used for detecting, counting, and sizing individual nanoparticles deposited onto the resonator [14]. In this detection scheme, since the two split modes reside in the same resonator, they are affected in the same way by the environmental noises [133]. This self-referencing property leads to an improvement of the detection limit. Using passive microtoroids, single PS nanospheres with radius 20 nm have been detected [107].

5.1 Introduction of Mode Splitting

In optical microcavities, each traveling wave mode (TWM) possesses a twofold degeneracy due to two propagation directions: clockwise (CW) and counterclockwise (CCW). These two degenerate modes have the same resonance frequency, linewidth, and field distribution function. When a sub-wavelength scatterer in the optical path couples the two counter propagating modes, this degeneracy could be lifted, leading to mode splitting which is observed as doublet modes in the transmission spectrum. Modal splitting was first reported in high- Q microspheres by Il'chenko and Gorodetsky [69] and later addressed in detail by Weiss *et al.* [134] leading to theoretical and experimental investigations of intrinsic (i.e., due to material inhomogeneities, structural defects, contaminations) and intentionally induced (i.e., due to controlled placement of scatterers in the mode volume) mode splitting in various passive resonators including microspheres, microtoroids and microdisks [46,106,135-136].

5.1.1 Coupling Equations

Assuming the CW and CCW modes are coupled via a sub-wavelength scatterer (dipole approximation) in the resonator mode volume as shown in Figure 5.1, based on Eq. (2.8), coupled mode equation of the system can be written as [46,106]

$$\frac{da_{\text{CW}}}{dt} = -\left[i(\omega_c + g) + \frac{\Gamma + \kappa_0 + \kappa_{\text{ex}}}{2} \right] a_{\text{CW}} - \left(ig + \frac{\Gamma}{2} \right) a_{\text{CCW}} - \sqrt{\kappa_{\text{ex}}} a_{\text{CW}}^{\text{in}} \quad (5.27)$$

$$\frac{da_{\text{CCW}}}{dt} = -\left[i(\omega_c + g) + \frac{\Gamma + \kappa_0 + \kappa_{\text{ex}}}{2} \right] a_{\text{CCW}} - \left(ig + \frac{\Gamma}{2} \right) a_{\text{CW}} - \sqrt{\kappa_{\text{ex}}} a_{\text{CCW}}^{\text{in}} \quad (5.28)$$

where

$$g = -\frac{\alpha f^2(\mathbf{r})\omega_c}{2V} \quad (5.29)$$

denotes the coupling strength, and

$$\Gamma = \frac{\alpha^2 f^2(\mathbf{r})\omega_c^4}{6\pi\nu^3V} \quad (5.30)$$

is the energy damping rate induced by the scatterer, i.e., coupling of CW and CCW modes to the environment and to other modes. Here, a_{CW} and a_{CCW} are the intracavity field amplitudes for CW and CCW modes, a_{CW}^{in} and a_{CCW}^{in} are the input fields of the external waveguide, ω_c is the resonance frequency, α is the polarizability of the scatterer, $f(\mathbf{r})$ represents the normalized (i.e., normalized to the maximum value) distribution of the WGM field magnitude at the position \mathbf{r} of the scatterer, v is the velocity of light in the surrounding medium, and V is the mode volume. For a spherical scatterer of radius R , α is given by

$$\alpha = \frac{4\pi R^3 (n_p^2 - n_m^2)}{(n_p^2 + 2n_m^2)} \quad (5.31)$$

where n_p and n_m denote the refractive indices of the scatterer and the surrounding medium, respectively.

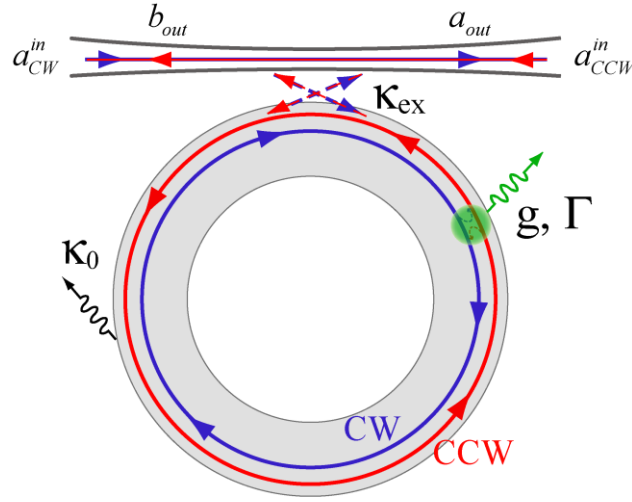


Figure 5.1 Schematic of a waveguide coupled resonator with scatterer induced mode splitting. CW: clockwise, CCW: counter-clockwise, κ_0 : intrinsic resonator loss, κ_{ex} : taper-resonator coupling loss, g : coupling coefficient of CW and CCW modes, and Γ : linewidth broadening due to the scatterer (green circle).

We apply Fourier transform on Eqs. (5.27) and (5.28) to obtain the steady-state solution

$$\left(-i\Delta\omega + ig + \frac{\Gamma + \kappa_0 + \kappa_{ex}}{2}\right)a_{CW} + \left(ig + \frac{\Gamma}{2}\right)a_{CCW} + \sqrt{\kappa_{ex}}a_{CW}^{in} = 0 \quad (5.32)$$

$$\left(-i\Delta\omega + ig + \frac{\Gamma + \kappa_0 + \kappa_{ex}}{2}\right)a_{CCW} + \left(ig + \frac{\Gamma}{2}\right)a_{CW} + \sqrt{\kappa_{ex}}a_{CCW}^{in} = 0. \quad (5.33)$$

Transmitted field at the output of the resonator in the CW direction is $a_{out} = a_{CW}^{in} + \sqrt{\kappa_{ex}} a_{CW}$. Similar expression can be obtained for the output in the CCW direction as $b_{out} = a_{CCW}^{in} + \sqrt{\kappa_{ex}} a_{CCW}$.

If we define $a_{\pm} = (a_{CW} \pm a_{CCW}) / \sqrt{2}$ and $a_{\pm}^{in} = (a_{CW}^{in} \pm a_{CCW}^{in}) / \sqrt{2}$, Eqs. (5.32) and (5.33) become

$$\left(-i(\Delta\omega - 2g) + \frac{2\Gamma + \kappa_0 + \kappa_{ex}}{2} \right) a_+ + \sqrt{\kappa_{ex}} a_+^{in} = 0 \quad (5.34)$$

$$\left(-i\Delta\omega + \frac{\kappa_0 + \kappa_{ex}}{2} \right) a_- + \sqrt{\kappa_{ex}} a_-^{in} = 0. \quad (5.35)$$

Here, a_+ and a_- are two orthogonal standing wave modes (SWMs) which are superposition of CW and CCW traveling wave modes. From Eqs. (5.34) and (5.35), a_+ and a_- are decoupled and therefore can be easily solved. The two SWMs have different resonance frequencies and damping rates. The symmetric mode (SM, “+”) has a detuning $2g$ from the degenerated WGM and an additional damping rate 2Γ , while the asymmetric mode (ASM, “-”) is not unperturbed by the scatterer. This is a result of the fact that the ASM (SM) field places the scatterer at its node (anti-node).

In this work, we study the single input case, i.e., $a_{CCW}^{in} = 0$. Then a_{CW} and a_{CCW} can be obtained by solving Eqs. (5.32) and (5.33) or Eqs. (5.34) and (5.35) and yielding

$$a_{CW} = \frac{-\sqrt{\kappa_{ex}} \left(-i\Delta\omega + ig + \frac{\Gamma + \kappa_0 + \kappa_{ex}}{2} \right)}{\left(-i\Delta\omega + ig + \frac{\Gamma + \kappa_0 + \kappa_{ex}}{2} \right)^2 - \left(ig + \frac{\Gamma}{2} \right)^2} a_{CW}^{in} \quad (5.36)$$

$$a_{CCW} = \frac{\sqrt{\kappa_{ex}} \left(ig + \frac{\Gamma}{2} \right)}{\left(-i\Delta\omega + ig + \frac{\Gamma + \kappa_0 + \kappa_{ex}}{2} \right)^2 - \left(ig + \frac{\Gamma}{2} \right)^2} a_{CW}^{in}. \quad (5.37)$$

Therefore, the power reflection R_{ef} and transmission T_r can be written as

$$\begin{aligned}
R_{\text{ef}} &= \left| \frac{b_{\text{out}}}{a_{\text{CW}}^{\text{in}}} \right|^2 = \left| \frac{\kappa_{\text{ex}} \left(ig + \frac{\Gamma}{2} \right)}{\left(-i\Delta\omega + ig + \frac{\Gamma + \kappa_0 + \kappa_{\text{ex}}}{2} \right)^2 - \left(ig + \frac{\Gamma}{2} \right)^2} \right|^2 \\
&= \frac{\frac{1}{4} \kappa_{\text{ex}}^2 (4g^2 + \Gamma^2)}{\left((\Delta\omega - 2g)^2 + \left(\frac{\kappa_{\text{SM}}}{2} \right)^2 \right) \left(\Delta\omega^2 + \left(\frac{\kappa_{\text{ASM}}}{2} \right)^2 \right)}
\end{aligned} \tag{5.38}$$

and

$$\begin{aligned}
T_r &= \left| \frac{a_{\text{out}}}{a_{\text{CW}}^{\text{in}}} \right|^2 = \left| 1 - \frac{\kappa_{\text{ex}} \left(-i\Delta\omega + ig + \frac{\Gamma + \kappa_0 + \kappa_{\text{ex}}}{2} \right)}{\left(-i\Delta\omega + ig + \frac{\Gamma + \kappa_0 + \kappa_{\text{ex}}}{2} \right)^2 - \left(ig + \frac{\Gamma}{2} \right)^2} \right|^2 \\
&= \frac{1}{2} \left(1 - \frac{\kappa_{\text{ex}} (2\Gamma + \kappa_0)}{(\Delta\omega - 2g)^2 + \left(\frac{\kappa_{\text{SM}}}{2} \right)^2} \right) + \frac{1}{2} \left(1 - \frac{\kappa_{\text{ex}} \kappa_0}{\Delta\omega^2 + \left(\frac{\kappa_{\text{ASM}}}{2} \right)^2} \right) - R_{\text{ef}}
\end{aligned} \tag{5.39}$$

where $\kappa_{\text{SM}} \equiv 2\Gamma + \kappa_0 + \kappa_{\text{ex}}$ is the total decay rate for the SM and $\kappa_{\text{ASM}} \equiv \kappa_0 + \kappa_{\text{ex}}$ is the decay rate for the ASM. The transmission spectrum has two resonant dips at 0 and $2g$ with linewidths of κ_{ASM} and κ_{SM} , respectively. The condition to resolve these two split modes is $|2g| > (\kappa_{\text{SM}} + \kappa_{\text{ASM}}) / 2$ which yields the strong coupling condition

$$|2g| > \Gamma + \omega_c / Q. \tag{5.40}$$

This means the coupling strength needs to exceed the sum of the scatterer induced loss and the cavity loss. This is a consequence of the long photon lifetime in the resonator which ensures that the coupling between the counter-propagating WGMs has time to manifest itself.

5.1.2 Measurements

Mode splitting can be detected and measured by recording the spectral transmission of the resonant mode while the excitation frequency is continuously scanned. To reduce

the influence of thermal effect, the launched power into the fiber taper should be as small as possible. In addition, a large taper-cavity gap is desired to minimize the taper coupling loss. Figure 5.2 shows the measured and calculated mode splitting spectra against the taper-cavity coupling condition. The simulation results in Figure 5.2(b) are calculated from Eqs. (5.38) and (5.39). In the top panel, where the large air gap indicates a small coupling loss, the two split modes are well resolved. With the taper-cavity gap declining, the coupling loss increases, leading to linewidth broadening of both modes. Further decrease in the gap damages the strong coupling condition. As a result, the two split modes merge together and become indistinguishable.

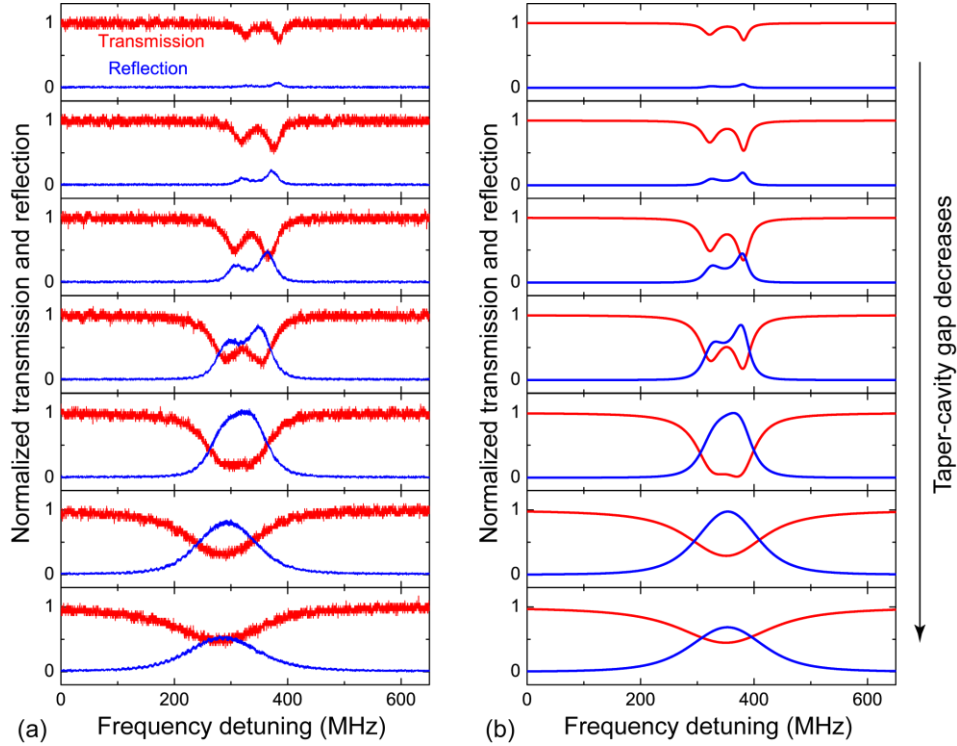


Figure 5.2 Power transmission (red) and reflection (blue) spectra of mode splitting in a passive silica microtoroid at different taper-cavity coupling conditions: (a) experimental measurements and (b) numerical calculations. From top to bottom panels, the taper-cavity gap gradually decreases with a total change of $0.5 \mu\text{m}$. Parameters for the simulation in (b) are $\kappa_0 = 1.0 \times 10^8 \text{ Hz}$, $\Gamma = 0.3\kappa_0$, and $g = -1.9\kappa_0$. From top to bottom panels, κ_{ex} equals to $0.16\kappa_0$, $0.35\kappa_0$, $0.65\kappa_0$, $1.2\kappa_0$, $3.0\kappa_0$, $9.0\kappa_0$, and $12.0\kappa_0$, respectively. In (b), the reflection coefficients are multiplied by 3 for visibility.

5.2 Mode Splitting for Single Nanoparticle Detection

Mode splitting in a WGM resonator can be used to detect single nanoparticles entering the resonator mode volume. In this section, we briefly introduce the theoretical model we use to characterize the particle induced splitting [107,137-139].

5.2.1 Single-Particle induced Mode Splitting

In the case of one single scatterer on the resonator, as shown in Figure 5.3(a), field distributions of the two SWMs have a spatial phase difference of $\pi/2$, i.e., the field node of one of the SWMs corresponds to the anti-node of the other. One SWM places its node at the location of the scatterer while the other has its anti-node at the same location. Obviously, the two SWM fields have different overlaps with the scatterer, and therefore are affected differently by the scatterer, which is reflected as the differences in the resonance frequency shift and resonance linewidth broadening with respect to the original degenerate mode. This effect is responsible for the observed mode splitting. The frequency splitting $2g$ and linewidth difference 2Γ of the two SWMs can be measured from the transmission spectrum [14].

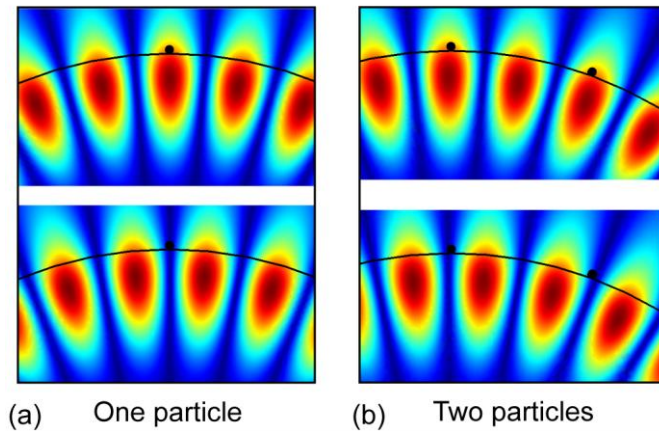


Figure 5.3 Mode distributions of two SWMs in a microtoroid in response to one single particle (a) and two particles (b) on the resonator surface. Black curves denote the resonator boundary and black dots represent particles.

Since both $2g$ and 2Γ are functions of the particle polarizability α , they can be used to estimate α , and thus the particle size. From Eqs. (5.29) and (5.30), $2g$ and 2Γ also depend on the particle position \mathbf{r} , which is difficult to measure. However, by taking their ratio, the position dependence is cancelled out yielding

$$\frac{\Gamma}{g} = -\frac{\alpha\omega_c^3}{3\pi v^3} \quad (5.41)$$

Substituting Eq. (5.31) to the above equation, the particle radius can be calculated by

$$R = \left[\frac{3\lambda_c^3 (\Gamma / g) (n_p^2 + 2n_m^2)}{32\pi^3 n_m^3 (n_p^2 - n_m^2)} \right]^{\frac{1}{3}}. \quad (5.42)$$

5.2.2 Multiple-Particle induced Mode Splitting

When multiple nanoparticles are deposited consecutively on a resonator, with each new particle entering the mode volume, the established SWMs are perturbed and redistributed such that the coupling strength between CW and CCW modes is maximized based on Fermat's principle [107]. As a result, one SWM experiences maximum resonance shift whereas the other SWM goes through minimum resonance shift, leading to a maximum frequency splitting between them. For example, Figure 5.3 presents the field distributions in response to one and two particles on the resonator.

Resonance shift and linewidth broadening of the two SWMs are given by sum of the effect from each individual particle whose contribution is modified by its position relative to the SWM distributions. This can be explained by the fact that strength of light-scatterer interaction, which determines the resonance shift and linewidth broadening, is proportional to the field intensity at the particle location. Assuming there are N particles continuously attaching on a resonator, we denote resonance frequency and linewidth of the initial degenerate mode as (ω_0, γ_0) and of the split modes after adsorption of N particles as (ω_N^1, γ_N^1) and (ω_N^2, γ_N^2) with the superscript describing two SWMs and the subscript representing particle number. We define the spatial phase

difference between the first particle and the anti-node of one of the SWMs as ϕ_N , and the phase distance between the first and the i -th particles as β_i . Then the frequency shift $(\Delta\omega_N^1, \Delta\omega_N^2)$ and linewidth broadening $(\Delta\gamma_N^1, \Delta\gamma_N^2)$ of the two SWMs can be expressed as

$$\Delta\omega_N^1 \equiv \omega_N^1 - \omega_0 = \sum_{i=1}^N 2g_i \cos^2(\phi_N - \beta_i), \Delta\omega_N^2 \equiv \omega_N^2 - \omega_0 = \sum_{i=1}^N 2g_i \sin^2(\phi_N - \beta_i) \quad (5.43)$$

$$\Delta\gamma_N^1 \equiv \gamma_N^1 - \gamma_0 = \sum_{i=1}^N 2\Gamma_i \cos^2(\phi_N - \beta_i), \Delta\gamma_N^2 \equiv \gamma_N^2 - \gamma_0 = \sum_{i=1}^N 2\Gamma_i \sin^2(\phi_N - \beta_i) \quad (5.44)$$

where $2g_i$ and $2\Gamma_i$ correspond to the resonance shift and linewidth broadening if the i -th particle is the only particle existed in the resonator mode volume.

Based on Eqs. (5.43) and (5.44), frequency splitting S_N and linewidth difference ρ_N of the two split modes are written as

$$S_N \equiv |\Delta\omega_N^1 - \Delta\omega_N^2| = \left| \sum_{i=1}^N 2g_i \cos(2\phi_N - 2\beta_i) \right| \quad (5.45)$$

$$\rho_N \equiv |\Delta\gamma_N^1 - \Delta\gamma_N^2| = \left| \sum_{i=1}^N 2\Gamma_i \cos(2\phi_N - 2\beta_i) \right|. \quad (5.46)$$

Parameter ϕ_N needs to satisfy the condition that the frequency splitting is maximized. By setting the derivative of Eq. (5.43) with respect to ϕ_N to zero, we obtain

$$\tan(2\phi_N) = \frac{\sum_{i=1}^N g_i \sin(2\beta_i)}{\sum_{i=1}^N g_i \cos(2\beta_i)}. \quad (5.47)$$

From the derivative of $\Delta\omega_N^1$ and $\Delta\omega_N^2$ with respect to ϕ_N , we can see that when one SWM has maximum resonance shift with respect to the degenerate mode, the other one shows minimum shift. For each new particle entering the mode volume, the two SWM distributions rotate to an appropriate position ϕ_N to maximize the frequency splitting. Frequency splitting and linewidth difference change correspondingly, which can be monitored to detect the particle.

As shown in Eqs. (5.45) and (5.46), even though S_N and ρ_N carry the information of particle polarizability, they depend on the positions of particles in the mode volume. In practical measurements, it is difficult and technologically challenging to place each particle at a specific position on the resonator. Therefore, S_N and ρ_N vary for each measurement. Figure 5.4(a) shows the measured frequency splitting in response to adsorption of PS nanospheres on a microtoroid. Each discrete change corresponds to one particle binding event. The variations in the amount of discrete changes are attributed to the non-uniform WGM field distribution along the resonator surface and the random particle positions on the resonator [13].

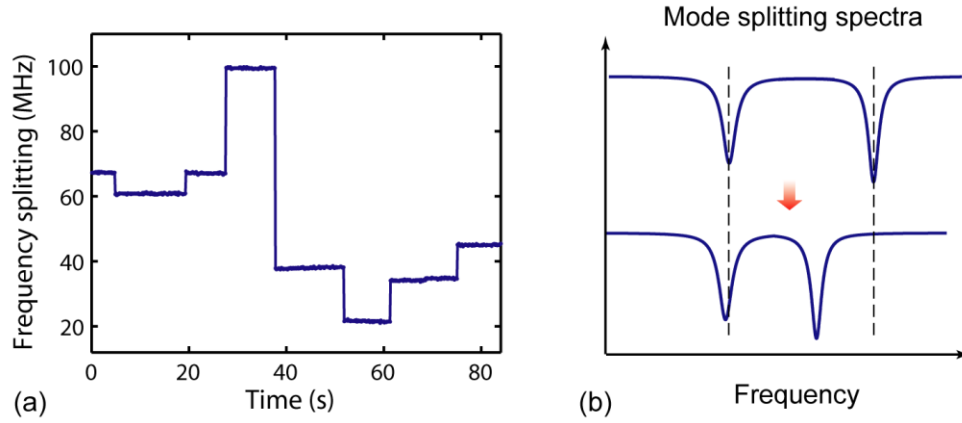


Figure 5.4 (a) Recorded frequency splitting with time as PS particles of radius 50 nm are deposited on a microtoroid continuously and one by one. (b) Illustration showing the possible shifts of the two split modes with the binding of a PS particle which leads to a decreased frequency splitting.

The effect of particle positions can be cancelled by taking into account the total resonance shift and linewidth broadening of the two split modes:

$$\Delta\omega_N^1 + \Delta\omega_N^2 = \sum_{i=1}^N 2g_i, \quad \Delta\gamma_N^1 + \Delta\gamma_N^2 = \sum_{i=1}^N 2\Gamma_i. \quad (5.48)$$

Using Eq. (5.48), the size of each adsorbed particle can be measured by detecting the corresponding resonance frequency shift and linewidth broadening of the two split modes. The details are presented in Ref. [107].

5.3 Self-Reference of Mode Splitting

In the presence of mode splitting in a WGM resonator, the two split modes reside in the same resonator, and thus are affected in the same way by environmental noises. Therefore, a self-referencing scheme is formed where one split mode acts as a reference for the other split mode and vice versa, leading to an improved detection limit for particle sensing. In this section, we experimentally demonstrate the self-referencing property of mode splitting by taking the change in environmental temperature as an example of the undesirable perturbations and studying its effect on the split modes. The effects are investigated in pure silica microtoroids and PDMS coated silica microtoroids. It is demonstrated that temperature changes in the surrounding environment have a negligible effect on mode splitting [133].

5.3.1 Temperature Response in Silica Microtoroids

Mode splitting in the silica microtoroid is introduced by depositing PS nanoparticles on the resonator surface. Environmental temperature is adjusted by a voltage controlled thermal cooler (TEC) placed under the microtoroid chip. Figure 5.5(a) shows the resonance frequency shifts of the two split modes with temperature. As temperature increases, resonances of both split modes shift to shorter frequency linearly, with the rate of shift (slope of the curve) mainly determined by the thermo-optic coefficient of silica.

When turning on the TEC, its temperature will gradually increase to the desired temperature. We recorded the mode splitting spectrum during this process at a data acquisition speed of 15 Frames/min, and presented the results in Figure 5.5(b) and (c). The TEC was turned on at Frame #1. The evolution of the mode splitting spectrum indicates the changes of the TEC temperature. Obviously, for a silica microtoroid, although the resonance of each split mode is significantly affected by the change in temperature, the amount of splitting between the two modes is not affected.

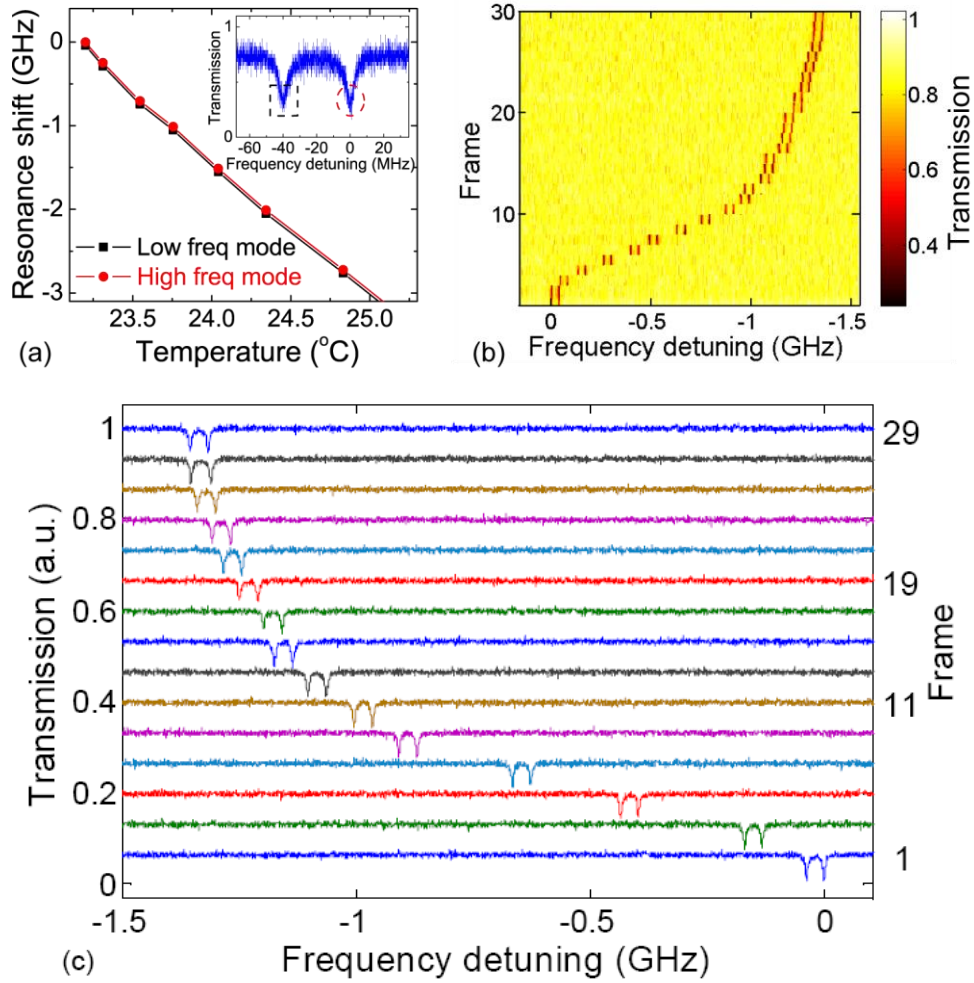


Figure 5.5 Dependence of mode splitting in a silica microtoroid on environment temperature. (a) Resonance frequency shifts of the split modes as a function of temperature. The red dots and black squares denote the higher-frequency and lower-frequency modes in the transmission spectrum, respectively, as marked in the inset. Inset: Splitting spectrum excited at around 1437.8 nm with doublet splitting of ~ 40 MHz. (b) Intensity graph of mode splitting spectrum as temperature increases. (c) Transmission spectra measured at different frames. Increasing frame number in (b) and (c) corresponds to increasing time.

5.3.2 Temperature Response in PDMS Coated Microtoroids

Microresonators made of polymers or coated with polymer thin films have been used for various sensing applications [38,78-80]. Mode splitting in polymer or polymer coated resonators has the potential as a sensing mechanism. Here, we study the temperature response of mode splitting in a PDMS coated silica microtoroid to further verify its

stability against thermal perturbations. The microtoroid is coated with a thin PDMS layer using wetting technique as described in chapter 3 [56]. The coated microtoroid has Q factors above 10^6 , mainly limited by the absorption of PDMS. Mode splitting can be introduced by either depositing nanoparticles on the coated resonator or embedding them inside the PDMS layer (e.g., incorporate particles in the PDMS prepolymer and then coat it on the resonator, or deposit particles on the silica resonator and then coat the PDMS layer). Electric field distributions of the split modes in both cases are shown in Figure 5.6. Symmetric and asymmetric modes with respect to the particle position are supported.

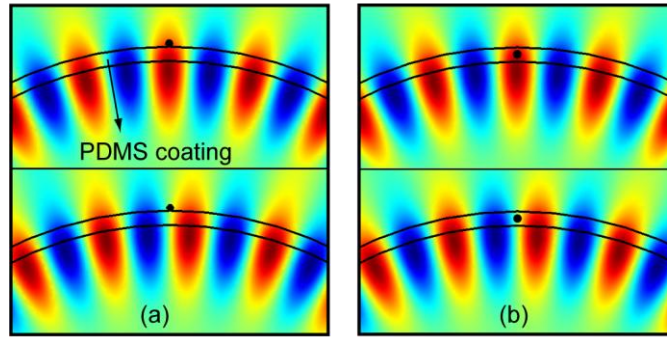


Figure 5.6 Field distributions of the symmetric and asymmetric modes with a particle deposited on the PDMS surface (a) and doped inside the PDMS layer (b).

In this study, we intentionally introduce mode splitting in the PDMS coated microtoroid with a fiber tip fabricated by heating and pulling an optical fiber followed by buffered-HF etching. After fixing the lateral position of the fiber tip, we gradually push it towards the peripheral of the resonator. As shown in Figure 5.7(a), when the tip makes the first contact with the resonator surface, it bends down and slides along the surface vertically. Due to the cone-like shape of the tip, the vertical movement gradually increases the size of the tip in the mode volume [137]. Figure 5.7(b) and (c) show the recorded mode splitting spectra for two WGMs with increasing tip size. In Figure 5.7(c), intrinsic mode splitting is observed due to the defects or contaminants introduced in the non-ideal coating process.

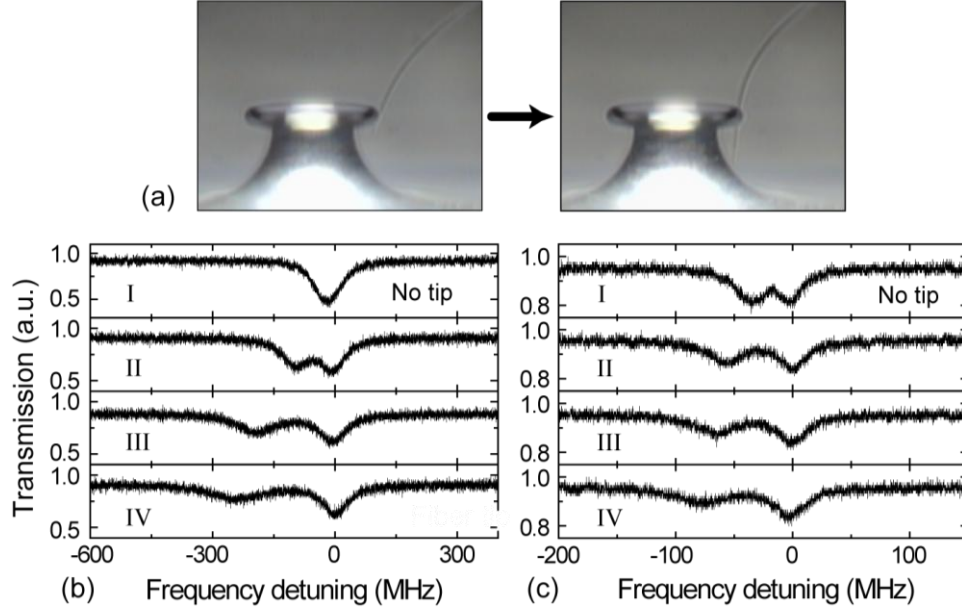


Figure 5.7 (a) Micrographs showing a fiber tip approaching a microtoroid. The right panel indicates a larger tip size interacting with the WGM field. Transmission spectra of WGMs at 1437.8 nm (b) and 1428.2 nm (c) in response to increasing tip size from top to bottom. From Lorentzian fitting, the linewidth of the resonant dip in I of (b) is 80.1 MHz corresponding to a Q of 2.6×10^6 , and the initial frequency splitting in I of (c) is 33.9 MHz.

As discussed in Sec. 5.2.1, size of the attached particle on the resonator can be estimated relying on the splitting spectrum using Eq. (5.42). Here we estimate the tip size by approximating it to a sphere. The resonance frequency and linewidth of the lower-frequency mode (f_1, γ_1) and the higher-frequency mode (f_2, γ_2) in Figure 5.7(b) and (c) are listed in Table 5.1. The calculated radius R of the tip interacting with the WGM field is also given.

Table 5.1 Resonance frequencies and linewidths of the split modes.

		f_1 (MHz)	f_2 (MHz)	γ_1 (MHz)	γ_2 (MHz)	$ f_2 - f_1 $ (MHz)	$ \gamma_2 - \gamma_1 $ (MHz)	R (nm)
(b)	I	0	-	-	80.10	-	-	0
	II	-96.12	-5.92	82.44	75.05	90.20	7.39	139.9
	III	-191.84	-5.93	115.58	80.16	185.91	35.42	185.4
	IV	-240.18	0.93	160.34	75.94	241.11	84.40	227.1
(c)	I	-35.70	-1.76	31.57	24.45	33.94	7.12	0
	II	-57.25	0.02	34.78	26.97	57.27	7.81	99.6
	III	-66.01	0.09	44.54	30.03	66.1	14.51	197.3
	IV	-77.91	-2.32	55.24	32.84	75.59	22.40	230.6

As the TEC temperature changes, the transmission spectrum is continuously recorded at a speed of 30 Frames/min. Figure 5.8(a) and (b) present the intensity graph and the transmission spectra of the split modes, where the TEC was turned on at Frame # 1 to start heating the sample, and turned off at Frame #58 to let the sample cool down. It is clearly seen that resonance wavelengths of the split modes experience red (blue) shifts as temperature increases (decreases). During the heating up and cooling down process, no significant alterations are observed in $2g$ and $2f$. Statistical analysis in Figure 5.8(c) and (d) shows splitting amount of 953 ± 25 MHz, and linewidth difference of 170 ± 26 MHz. The fluctuations might be attributed to the thermally induced changes in the refractive index and size of the fiber tip, fluctuations of the tip position with respect to the mode volume, and variations of the taper-cavity gap. It should be noted that the thickness of the PDMS layer mainly determines the rate of resonance shift with temperature, but does not affect the conclusions drawn above.

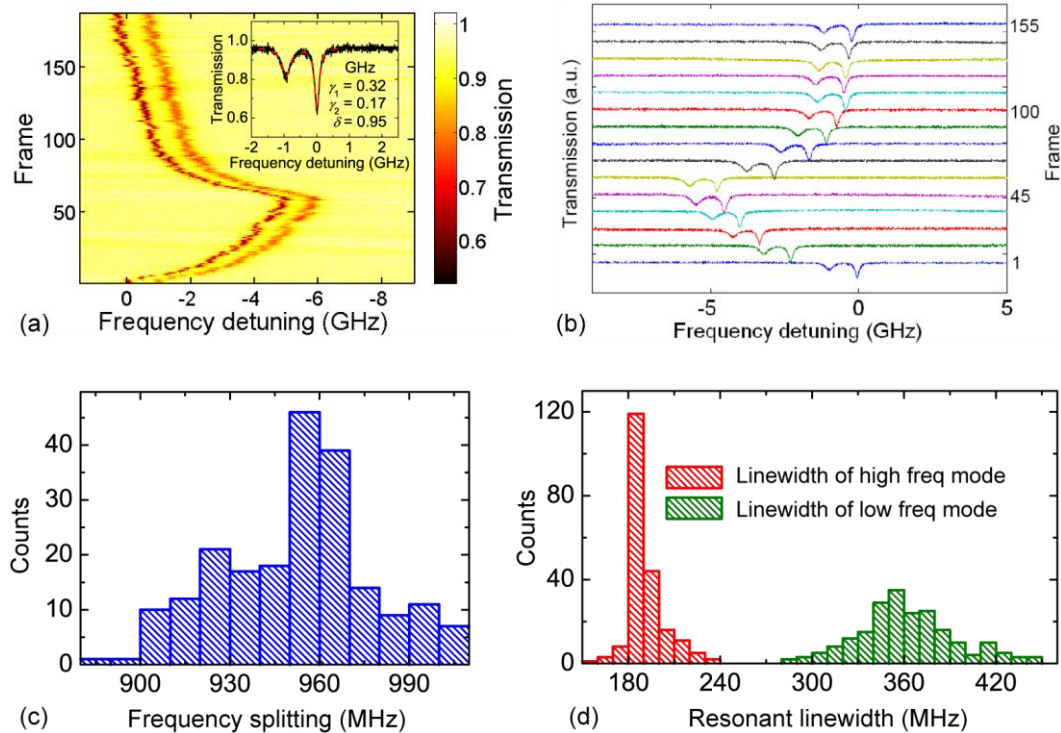


Figure 5.8 (a) Intensity graph of the splitting spectrum from a PDMS coated microtoroid. Inset: The WGM is excited at around 1536.5 nm with a frequency splitting of 950 MHz induced by a fiber tip. (b) Transmission spectra at different frames. Histograms of the frequency splitting (c) and linewidths (d) of the doublet modes for spectra in (a).

In summary, temperature response of the split modes in silica resonators and polymer coated resonators is investigated to show the robustness of mode splitting. From the experimental observations, we can conclude that regardless of the resonator material, mode splitting is robust against thermal perturbations. Similarly, the self-referencing property of mode splitting suggests that the influence of undesired environmental perturbations (e.g., humidity and air pressure) which affect the whole resonant system homogeneously can be avoided. Demonstration of mode splitting in polymer coated resonators opens exciting possibilities in resonator-based sensing technologies by combining the versatility of polymers with the self-referencing mode splitting technique. As mode splitting is affected by the overlap between the particle and the WGM field, any changes in the overlap (e.g., acoustic pressure induced deformation of the polymer, change in refractive index or shape of the particle) will lead to variations in the splitting, which in return can be utilized to detect these changes.

5.4 Detection Limit

Strong coupling condition in Eq. (5.40) indicates the lower bound of detectable particle size using a microcavity. The fundamental limitations are determined by the resonator parameter Q/V , which is pivotal in determining the interaction strength between the cavity field and the nano-object. Higher Q implies lower loss and narrower resonance linewidth, indicating smaller detectable changes in the resonance spectrum. For example, Q factor exceeding 10^8 can be easily obtained in silica microsphere and microtoroid resonators, allowing detecting resonance shift or splitting on the order of femtometer. Smaller V , on the other hand, implies a more confined field and a larger splitting $2g$. Using mode splitting based detection, the smallest detectable particle size is 20 nm in radius [107].

To obtain a better detection limit, we need to reduce the mode volume V and enhance the Q factor. The mode volume can be reduced by decreasing the cavity size. However, cavity size cannot be made arbitrary small without sacrificing the Q factor. If the

resonator size is smaller than some value, its Q will degrade significantly due to the increased radiation loss. The ultimate Q factor of the resonator is limited by the cavity material absorption loss. One method to enhance the Q factor and thus improve the detection limit is to dope the passive resonator with active medium so that a part of the cavity losses can be compensated by the optical gain provided by the active material. Mode splitting in active resonators will be studied in chapter 6.

Chapter 6

Mode Splitting in Active Resonators

It has been demonstrated that mode splitting in WGM resonators can be used to detect and size single nanoparticles. However, the minimum detectable particle size is limited by the linewidth of the resonant mode which is characterized by the Q factor. To enhance the Q factor, one can introduce active medium into the resonator. Optical gain from the active medium will compensate for the cavity losses, thereby increasing the Q factor.

In active microcavities, there are two specific regimes to reveal the originally covered mode splitting: (i) The active microcavity is pumped below the lasing threshold. Optical gain from the active medium compensates for part of the cavity losses depending on the pumping level and leads to Q -enhancement making mode splitting resolvable in the transmission spectrum [140]. (ii) The pump power exceeds the lasing threshold. Mode splitting manifests itself as two lasing modes with narrow linewidths. Mixing of these lasing modes in a photodetector leads to a heterodyne beat signal whose frequency corresponds to the mode splitting amount [105]. Lasing regime not only allows ultra-high sensitivity for mode splitting measurements but also provides an easily accessible scheme by eliminating the need for wavelength scanning around the resonant modes.

Mode splitting in active microresonators has immediate impact in enhancing the sensitivity of sub-wavelength scatterer detection and in studying light-matter interactions in strong coupling regime. In this chapter, we study the mode splitting effect in active microcavities operated below and above the lasing threshold, respectively.

6.1 Below the Lasing Threshold

In an active resonator, when the gain medium is pumped below the lasing threshold to provide optical gain, linewidth of the resonant mode is narrowed. Transmission spectrum of the resonant mode varies depending on the gain-loss relation. In the presence of mode splitting, the two split modes experience different loss mechanisms because of their spatially orthogonal field distributions. The same gain and different losses experienced by the two split modes lead to a number of different interesting transmission spectra depending on the mode splitting parameters and the coupling loss. In this section, we first introduce a theoretical model to study mode splitting in an active microresonator and then systematically investigate the effects of optical gain on mode splitting spectra by numerical analysis and experiments.

6.1.1 Active Microresonators without Mode Splitting

Effects of optical gain on a single WGM have been studied theoretically and experimentally [141-142]. For a fiber taper coupled passive resonator, the total round-trip losses are determined by the intrinsic loss rate κ_0 and the taper coupling loss rate κ_{ex} . In an active resonator, on the other hand, the total loss is reduced by the gain parameter ξ (round-trip energy gain). Thus, time evolution of the intracavity field a in an active resonator can be written as

$$\frac{da}{dt} = -\left(i\omega_c + \frac{\kappa_0 + \kappa_{ex} - \xi}{2}\right)a - \sqrt{\kappa_{ex}}a_{in} \quad (6.49)$$

where ω_c is the resonance frequency, and a_{in} is the input field. In Eq. (6.49), we ignore the gain saturation effect and focus on the small signal analysis. Using $a_{out} = a_{in} + (\kappa_{ex})^{1/2}a$ for the transmitted light field, the steady-state power transmission yields

$$T_r(\Delta\omega) = \left|\frac{a_{out}}{a_{in}}\right|^2 = \frac{\Delta\omega^2 + \left(\frac{\kappa_{eff} - \kappa_{ex}}{2}\right)^2}{\Delta\omega^2 + \left(\frac{\kappa_{eff} + \kappa_{ex}}{2}\right)^2} \quad (6.50)$$

where $\kappa_{\text{eff}} \equiv \kappa_0 - \xi$ is defined as the effective intrinsic damping rate of the resonator. In the following discussion, κ_0 and $\kappa_0 + \kappa_{\text{ex}}$ are referred to as intrinsic passive loss and total passive loss, respectively. From Eq. (6.50), it is seen that $\kappa_{\text{eff}} > 0$ corresponds to optical attenuation ($T_r < 1$) whereas $\kappa_{\text{eff}} < 0$ corresponds to optical amplification ($T_r > 1$), indicating that transmission spectra of the WGMs can be modified by adjusting the gain ξ .

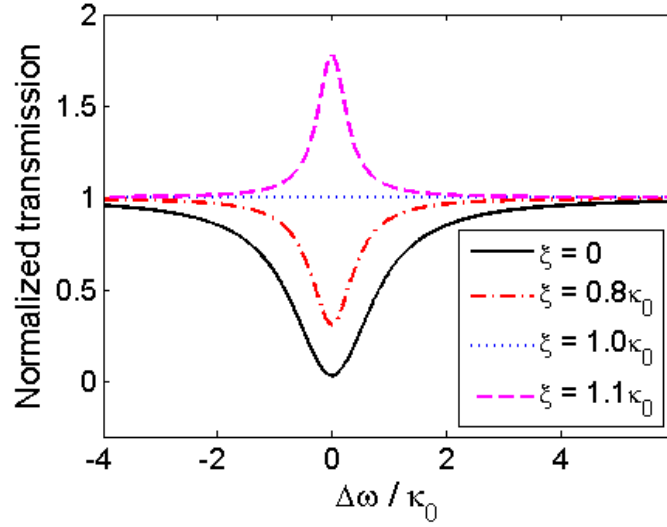


Figure 6.1 Simulation results showing the transmission spectrum at different gain values ξ . Parameters used for the calculations are: $\lambda_c = 1550$ nm, $\kappa_0 = 4.0 \times 10^7$ Hz ($Q_0 = 3.0 \times 10^7$), and $\kappa_{\text{ex}} = 0.7 \kappa_0$ ($Q_{\text{ex}} = 4.3 \times 10^7$).

Based on Eq. (6.50), there are four distinct regimes for the transmission spectrum determined by the value of ξ as shown in Figure 6.1. (i) No gain ($\xi = 0$). The optical mode is manifested as a Lorentzian-shaped dip in the transmission spectrum. (ii) Gain is smaller than the intrinsic passive loss ($\xi < \kappa_0$, i.e., $\kappa_{\text{eff}} > 0$). As ξ increases, κ_{eff} decreases, giving rise to narrowing of the resonance linewidth and enhancement of the Q factor. Thus, the cavity Q can be adjusted by modulating the optical gain without changing the coupling condition. Enhanced Q of the active resonator is ultimately limited by spontaneous emission noise of the gain medium. (iii) Gain exceeds the intrinsic passive loss but is smaller than the total passive loss of the resonator ($\kappa_0 < \xi < \kappa_0 + \kappa_{\text{ex}}$, i.e., $-\kappa_{\text{ex}} < \kappa_{\text{eff}} < 0$). The effective intrinsic loss κ_{eff} becomes negative. Consequently the resonant dip in the transmission spectrum evolves into a resonant peak, indicating that

light in the resonator is amplified. The resonator operates as a selective amplifier in this regime. (iv) Gain exceeds the total passive loss ($\xi > \kappa_0 + \kappa_{\text{ex}}$, i.e., $\kappa_{\text{eff}} < -\kappa_{\text{ex}}$). Laser oscillation is expected in this regime.

We conclude this section by noting that gain ξ of the active medium has a two-fold effect on the resonator. First, it narrows down the linewidth of the resonant dip or resonant peak. Second, it provides a way to control the transmission spectrum of the resonant mode, allowing the transition from a resonant dip to a resonant peak.

6.1.2 Active Microresonators with Mode Splitting

In the presence of a sub-wavelength scatterer in the resonator mode volume, the WGM undergoes mode splitting resulting from back-scattering induced coupling between the CW and CCW propagating modes (Figure 6.2). Consequently, a doublet in the form of two resonant dips appears in the transmission spectrum [106,136,139].

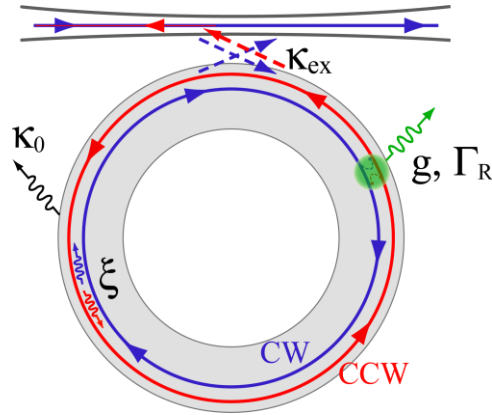


Figure 6.2 Schematic diagram showing mode splitting in a fiber taper coupled active resonator.

Mode splitting phenomenon has been observed and studied extensively in passive resonators, however, properties of mode splitting in active resonators remain to be explored. In order to understand how the gain affects the split modes and how the effects differ from those of a single mode case, we modify the equations of motion,

which describe the coupling of the two counter-propagating modes, by incorporating the gain of the active medium:

$$\frac{da_{CW}}{dt} = -\left(i\omega_c + ig + \frac{\Gamma + \kappa_0 + \kappa_{ex} - \xi_{CW}}{2}\right)a_{CW} - \left(ig + \frac{\Gamma}{2}\right)a_{CCW} - \sqrt{\kappa_{ex}}a_{CW}^{in} \quad (6.51)$$

$$\frac{da_{CCW}}{dt} = -\left(i\omega_c + ig + \frac{\Gamma + \kappa_0 + \kappa_{ex} - \xi_{CCW}}{2}\right)a_{CCW} - \left(ig + \frac{\Gamma}{2}\right)a_{CW} - \sqrt{\kappa_{ex}}a_{CCW}^{in} \quad (6.52)$$

where a_{CW} and a_{CCW} are intracavity field amplitudes for CW and CCW modes, a_{CW}^{in} and a_{CCW}^{in} are input fields of the external waveguide. Round-trip energy gains for CW and CCW modes under small signal assumption are denoted as ξ_{CW} and ξ_{CCW} , respectively. For high signal powers, gain saturations including self-saturation and cross-saturation would be taken into account leading to nonlinear coupling of CW and CCW modes [143-144]. In this study, we carry out the analysis in linear coupling regime as the experiments are performed below the lasing threshold and the optical power is kept small. Moreover, for the sake of simplicity, we assume $\xi_{CW} = \xi_{CCW} = \xi$. Then the transmission characteristic in steady-state regime is obtained by taking Fourier transform of Eqs. (6.51) and (6.52) yielding

$$\left(-i\Delta\omega + ig + \frac{\Gamma + \kappa_0 + \kappa_{ex} - \xi}{2}\right)a_{CW} + \left(ig + \frac{\Gamma}{2}\right)a_{CCW} + \sqrt{\kappa_{ex}}a_{CW}^{in} = 0 \quad (6.53)$$

$$\left(-i\Delta\omega + ig + \frac{\Gamma + \kappa_0 + \kappa_{ex} - \xi}{2}\right)a_{CCW} + \left(ig + \frac{\Gamma}{2}\right)a_{CW} + \sqrt{\kappa_{ex}}a_{CCW}^{in} = 0. \quad (6.54)$$

Transmitted field at the output of the resonator in the CW direction is $a_{out} = a_{CW}^{in} + \sqrt{\kappa_{ex}}a_{CW}$. Similar expression can be obtained for the output in the CCW direction as $b_{out} = a_{CCW}^{in} + \sqrt{\kappa_{ex}}a_{CCW}$.

Eigenmodes of this resonator system are two orthogonal standing wave modes having different resonance frequencies and damping rates. We transform Eqs. (6.53) and (6.54) to standing wave bases by defining $a_{\pm} = (a_{CW} \pm a_{CCW})/\sqrt{2}$ and $a_{\pm}^{in} = (a_{CW}^{in} \pm a_{CCW}^{in})/\sqrt{2}$, and obtain

$$\left(-i(\Delta\omega - 2g) + \frac{2\Gamma + \kappa_0 + \kappa_{ex} - \xi}{2}\right)a_+ + \sqrt{\kappa_{ex}}a_+^{in} = 0 \quad (6.55)$$

$$\left(-i\Delta\omega + \frac{\kappa_0 + \kappa_{ex} - \xi}{2}\right)a_- + \sqrt{\kappa_{ex}}a_-^{in} = 0. \quad (6.56)$$

Here, a_+ and a_- are decoupled and can be studied separately. From Eqs. (6.55) and (6.56), we see that the asymmetric mode (ASM, “-”) remains unperturbed by the scatterer, whereas the symmetric mode (SM, “+”) undergoes a detuning $2g$ from the degenerate mode and an additional loss 2Γ . From the experimental point of view, $|2g|$ represents the angular frequency splitting between ASM and SM, while 2Γ is the linewidth difference of ASM and SM.

From Eqs. (6.55) and (6.56), the ASM experiences total loss $\kappa_{ASM} \equiv \kappa_0 + \kappa_{ex} - \xi$ whereas the SM experiences total loss $\kappa_{SM} \equiv 2\Gamma + \kappa_0 + \kappa_{ex} - \xi$. The condition to resolve the splitting becomes

$$|2g| > (\kappa_{ASM} + \kappa_{SM}) / 2 = \Gamma + \kappa_0 + \kappa_{ex} - \xi. \quad (6.57)$$

The gain ξ makes it possible to resolve mode splitting even in a resonator with low Q factors (large κ_0). On the other hand, because the SM experiences an additional damping rate 2Γ over the ASM, they react differently to the same gain value ξ .

Table 6.1 Conditions of optical attenuation, amplification, and lasing for ASM and SM modes.

	ASM	SM
Intrinsic passive loss	κ_0	$2\Gamma + \kappa_0$
Coupling loss	κ_{ex}	κ_{ex}
Gain	ξ	ξ
Attenuation	$\xi < \kappa_0$	$\xi < 2\Gamma + \kappa_0$
Amplification	$\xi > \kappa_0$	$\xi > 2\Gamma + \kappa_0$
Lasing	$\xi > \kappa_0 + \kappa_{ex}$	$\xi > 2\Gamma + \kappa_0 + \kappa_{ex}$

Following similar analysis as for the single WGM in Sec. 6.1.1, Table 6.1 shows the conditions to obtain optical attenuation, amplification, and lasing for the ASM and SM, respectively. As ξ gradually increases, the ASM is amplified first. Gain ξ should be further increased to compensate for the additional loss 2Γ to amplify the SM. Depending on the relative value of ξ with respect to κ_0 , $\kappa_0 + \kappa_{ex}$, and $2\Gamma + \kappa_0$, the transmission spectrum of ASM and SM show different profiles: attenuation for both modes, amplification for both modes, and amplification for the ASM and attenuation for the SM.

To study the influence of optical gain on ASM and SM in the resonator, we need to find out the power transmission (T_r) and reflection (R_{ce}) coefficients which are accessible and measurable parameters in experiments. By defining $a_{\pm}^{out} = a_{\pm}^{in} + \sqrt{\kappa_{ex}} a_{\pm}$, field transmission $t_{\pm} = a_{\pm}^{out} / a_{\pm}^{in}$ can be obtained from Eqs. (6.55) and (6.56) as

$$t_+ = 1 - \frac{\kappa_{ex}}{-i(\Delta\omega - 2g) + (2\Gamma + \kappa_0 - \xi + \kappa_{ex})/2} \quad (6.58)$$

$$t_- = 1 - \frac{\kappa_{ex}}{-i\Delta\omega + (\kappa_0 - \xi + \kappa_{ex})/2}. \quad (6.59)$$

In the absence of CCW input, i.e., $a_{CCW}^{in} = 0$, the amplitude transmission coefficient (CW direction) yields

$$t = \frac{a_{out}}{a_{CW}^{in}} = 1 - \frac{\kappa_{ex}\beta}{\beta^2 - (ig + \Gamma/2)^2} = \frac{t_+ + t_-}{2} \quad (6.60)$$

where $\beta \equiv -i\Delta\omega + ig + (\Gamma + \kappa_0 - \xi + \kappa_{ex})/2$. The power transmission is then written as

$$T_r = |t|^2 = \left| \frac{t_+ + t_-}{2} \right|^2 = \frac{1}{4}|t_+|^2 + \frac{1}{4}|t_-|^2 + \frac{1}{2}\text{Re}\{t_+ t_-^*\}. \quad (6.61)$$

Here * denotes complex conjugate and $\text{Re}\{\dots\}$ implies that the real part is taken. Similarly, we get the amplitude reflection coefficient (CCW direction)

$$r = \frac{b_{out}}{a_{CW}^{in}} = \frac{\kappa_{ex}(ig + \Gamma/2)}{\beta^2 - (ig + \Gamma/2)^2} = \frac{t_+ - t_-}{2} \quad (6.62)$$

and the power reflection

$$R_{ef} = |r|^2 = \frac{1}{4}|t_+|^2 + \frac{1}{4}|t_-|^2 - \frac{1}{2}\text{Re}\{t_+t_-^*\}. \quad (6.63)$$

From Eqs. (6.61) and (6.63), it is easy to get

$$T_r = \frac{1}{2}|t_+|^2 + \frac{1}{2}|t_-|^2 - R_{ef} \quad (6.64)$$

yielding

$$R_{ef} = \frac{\frac{1}{4}\kappa_{ex}^2(4g^2 + \Gamma^2)}{\left((\Delta\omega - 2g)^2 + \left(\frac{2\Gamma + \kappa_0 + \kappa_{ex}}{2}\right)^2\right)\left(\Delta\omega^2 + \left(\frac{\kappa_0 + \kappa_{ex}}{2}\right)^2\right)} \quad (6.65)$$

and

$$T_r(\Delta\omega) = \frac{1}{2} \frac{(\Delta\omega - 2g)^2 + \left(\frac{2\Gamma + \kappa_0 - \xi - \kappa_{ex}}{2}\right)^2}{(\Delta\omega - 2g)^2 + \left(\frac{2\Gamma + \kappa_0 - \xi + \kappa_{ex}}{2}\right)^2} + \frac{1}{2} \frac{\Delta\omega^2 + \left(\frac{\kappa_0 - \xi - \kappa_{ex}}{2}\right)^2}{\Delta\omega^2 + \left(\frac{\kappa_0 - \xi + \kappa_{ex}}{2}\right)^2} - R_{ef}. \quad (6.66)$$

It is important to note that in Eq. (6.66) there are three terms: the first two terms describe the contributions of SM (a_+) and ASM (a_-) to the transmission, while the third term is an interference term including contributions from both modes.

Based on Eq. (6.66), we study the evolution of mode splitting spectrum with gain ξ for different Γ under three taper coupling conditions, i.e., $\kappa_{ex} < \kappa_0$, $\kappa_{ex} = \kappa_0$, and $\kappa_{ex} > \kappa_0$. A representative set of typical mode splitting spectra is depicted in Figure 6.3. It is seen that, for a given value of g , the mode splitting spectra are mainly determined by the interplay of the gain ξ and the loss experienced by ASM and SM. In what follows, we discuss four different operation regimes, where three typical mode splitting profiles, i.e. two resonant dips, one dip and one peak, and two resonant peaks, appear in the transmission spectra.

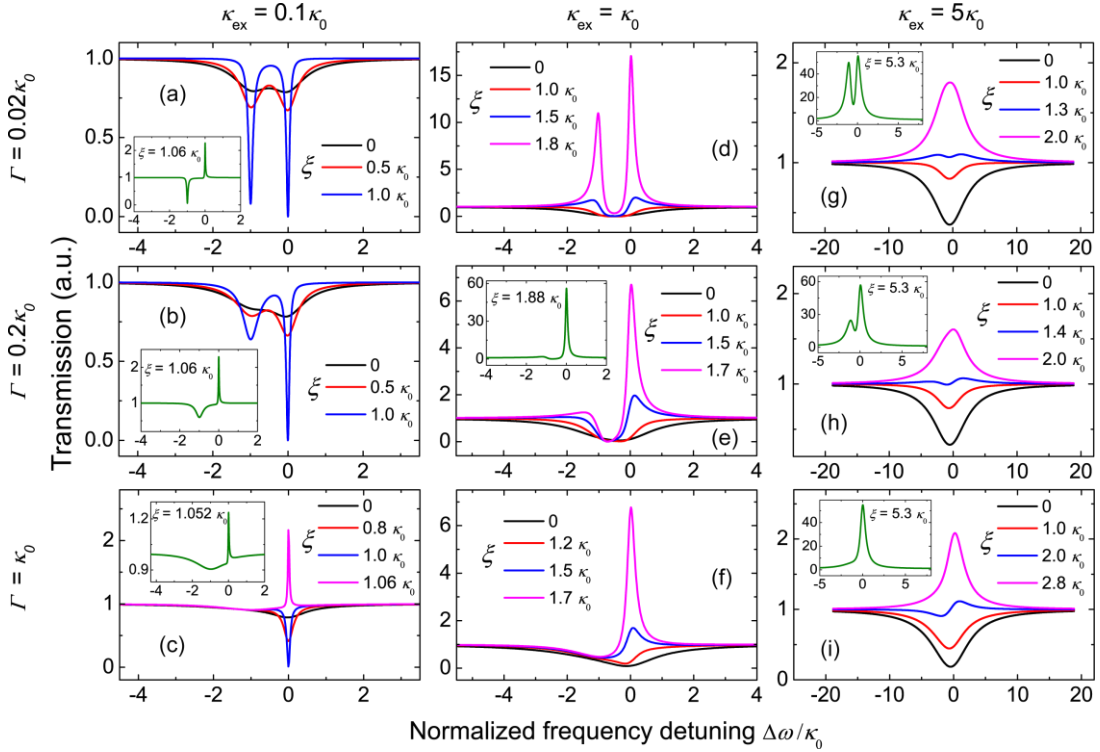


Figure 6.3 (a) Calculated power transmission spectra as a function of frequency detuning for various taper-cavity coupling condition κ_{ex} and additional damping rate Γ . Parameters used in the simulation are $\kappa_0=4.0\times 10^7$ Hz, $g=-0.5\kappa_0$, and $\lambda_c=1550$ nm. In each plot, transmission spectrum is obtained at different ξ .

(i) $\xi < \kappa_0$ (ASM: Resonant dip; SM: Resonant dip). Gain is too small to compensate for the intrinsic cavity loss of either ASM or SM, and therefore both modes experience attenuation. As ξ increases, resonance linewidths of ASM and SM become narrower, increasing the resolvability of mode splitting. When Eq. (6.57) is satisfied, the transmission spectrum shows two resonant dips (Figure 6.3(a) and (b)). Otherwise, mode splitting cannot be resolved and a single resonant dip is observed (Figure 6.3(c-i)). For the maximum gain in this regime, i.e., $\xi = \kappa_0$, the condition to resolve the splitting between two resonant dips becomes $|2g| > \Gamma + \kappa_{\text{ex}}$. In Figure 6.3, this condition is only satisfied in (a) and (b), in which doublet dips are observed.

(ii) $\kappa_{\text{ex}} < 2\Gamma$ and $\kappa_0 < \xi < \kappa_0 + \kappa_{\text{ex}}$ (ASM: Resonant peak; SM: Resonant dip). Gain overcomes the intrinsic loss experienced by ASM, but is still smaller than the intrinsic

loss of the SM. As a result, the ASM appears as a peak in the transmission spectrum while SM appears as a dip (Figure 6.3(b), (c), and (f)). It should be noted that, if $\kappa_{\text{ex}} < 2\Gamma$ is satisfied, below the lasing threshold (i.e., $\xi < \kappa_0 + \kappa_{\text{ex}}$), gain ξ is always smaller than the intrinsic loss of SM (i.e., $\xi < \kappa_0 + 2\Gamma$), and the SM will always reflect itself as a resonant dip. Therefore, no doublet peaks could be observed in the case of $\kappa_{\text{ex}} < 2\Gamma$.

(iii) $\kappa_{\text{ex}} > 2\Gamma$ and $\kappa_0 < \xi < \kappa_0 + 2\Gamma$ (ASM: Resonant peak; SM: Resonant dip). ASM is amplified whereas SM is attenuated, as shown in Figure 6.3(a), (e), (h), and (i).

(iv) $\kappa_{\text{ex}} > 2\Gamma$ and $\kappa_0 + 2\Gamma < \xi < \kappa_0 + \kappa_{\text{ex}}$ (ASM: Resonant peak; SM: Resonant peak). Gain overcomes the intrinsic losses of both ASM and SM leading to optical amplification for both modes. When Eq. (6.57) is satisfied, two resonant peaks corresponding to ASM and SM are distinguished in the transmission spectrum (Figure 6.3(d), (e), (g), and (h)). Further increasing ξ narrows down the resonance linewidths of the peaks. For the maximum ξ in this regime, i.e., $\xi = \kappa_0 + \kappa_{\text{ex}}$, Eq. (6.57) becomes $|2g| > \Gamma$. Therefore, conditions $\kappa_{\text{ex}} > 2\Gamma$ and $|2g| > \Gamma$ are required to resolve the doublet peaks in the transmission spectrum. For example, in Figure 6.3(i), $|2g| > \Gamma$ is not satisfied, and consequently the resonant peaks for ASM and SM cannot be resolved, showing only one peak in the transmission spectrum even for high ξ (inset of Figure 6.3(i)).

For the sake of simplicity, in the above discussions for different operation regimes, we considered only the influence of the first two terms in Eq. (6.66) on the mode splitting spectrum. In Figure 6.3, all three terms were used to calculate the spectra. Taking the third term into account does not change the conclusions on the type of possible profiles and splitting dynamics, however, it leads to modifications in the boundaries of the regimes (i)-(iv). This explains why two resonant dips are observed instead of one for $\xi = \kappa_0$ (i.e., the second term in Eq. (6.66) becomes a constant) in Figure 6.3(a) and (b).

Since 2Γ is the difference of damping rates between ASM and SM, its value determines how differently ASM and SM respond to changes in ξ . If $\Gamma \ll \kappa_0$, the losses experienced by ASM and SM are approximately equal, leading to symmetric transmission spectra (Figure 6.3(a), (d), and (g)). As Γ increases and is comparable to or larger than κ_0 , the spectrum becomes asymmetric. Transitions from symmetric to asymmetric spectra and from attenuation to amplification of the split modes are clearly seen in Figure 6.3. The amount of splitting $|2g|$ determines how far ASM and SM are separated, and will affect the condition to resolve mode splitting. Under different conditions, mode splitting in the transmission spectrum can be resolved as two resonant dips, two resonant peaks, or one resonant dip and one resonant peak.

For fixed mode splitting in a WGM resonator, the values of κ_0 , g , and Γ are all constant. Gain ξ from the active medium and coupling loss κ_{ex} can be tuned to adjust the appearance of the transmission spectrum. Here we discuss the effects of coupling loss on the mode splitting spectra when gain is below the lasing threshold.

As described in (i), to resolve the mode splitting as two resonant dips, condition $|2g| > \Gamma + \kappa_{\text{ex}}$ should be satisfied (when $\xi = \kappa_0$). This is easy to achieve for deep under coupling condition $\kappa_{\text{ex}} \ll \kappa_0$. Since the total cavity loss in this case is mainly determined by the effective intrinsic loss ($\kappa_0 - \xi$ for ASM and $2\Gamma + \kappa_0 - \xi$ for SM), increasing ξ reduces the effective intrinsic losses and thus narrows down the resonance linewidths, helping resolve the splitting. On the other hand, transmission spectrum in the deep under coupling regime with a resonant peak for ASM and a resonant dip for SM exists only for a small range of gain, which is $\kappa_0 < \xi < \kappa_0 + \min(\Gamma, \kappa_{\text{ex}})$.

If the coupling loss κ_{ex} is comparable with or larger than the intrinsic loss κ_0 , condition $|2g| > \Gamma + \kappa_{\text{ex}}$ in (i) is usually not easy to satisfy because of the large κ_{ex} . If $|2g| < \Gamma + \kappa_{\text{ex}}$, no resolved doublet dips appear in the transmission spectrum. Instead, transmission spectrum with one resonant peak (ASM) and one resonant dip (SM) is easy to be observed in this coupling regime.

The above model considers a single sub-wavelength scatterer in the mode volume of an active resonator. In the case of multiple scatterers in the mode volume, the above equations and analysis are still valid by assigning effective g and Γ which take into account the individual contributions from all scatterers. In this case, ASM (SM) refers to the resonant mode of the doublet with the narrower (broader) linewidth [137-138].

6.1.3 Experiments

In order to confirm the validity of the theoretical model and reproduce the mode splitting spectra predicted from the model, we perform experiments using Er-doped microtoroidal resonators, which are fabricated from Er-doped silica sol-gel films through photolithography procedure and CO₂ laser reflow [12]. Typical diameter of the microtoroids used in the experiments is 50 μm , and the Er³⁺ ion concentration is $\sim 3 \times 10^{18} \text{ cm}^{-3}$. During the fabrication process, clusters of Er³⁺ ions, dusts, and defects may be introduced in the resonator, causing Q degradation ($\sim 10^7$) and intrinsic mode splitting.

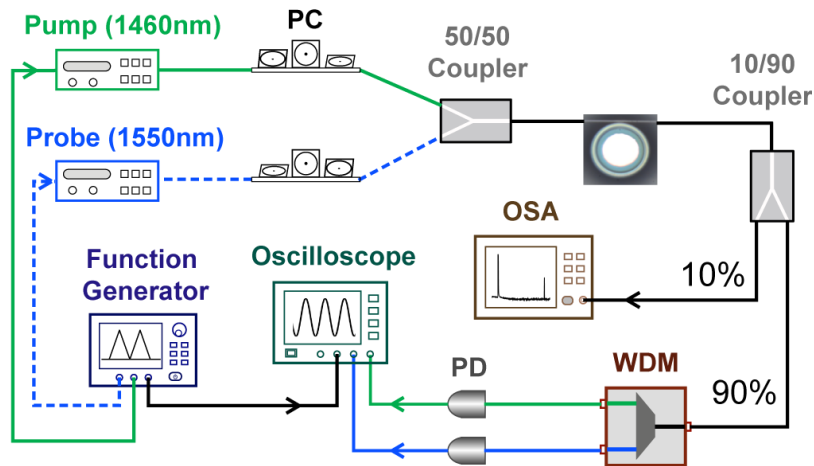


Figure 6.4 Experimental setup. PD: Photodetector, PC: Polarization controller, OSA: Optical spectrum analyzer, WDM: Wavelength division multiplexer.

The pump-probe experiment is designed with the setup shown in Figure 6.4. Transmission spectrum of the resonant mode is measured by injecting a low-power

probe light when the gain medium is pumped. Pumping of Er^{3+} ions in the resonator is achieved using a tunable laser in 1460 nm band. The pump wavelength is tuned on resonance with a resonant mode to increase the pumping efficiency. The probe light is provided by a tunable laser in 1550 nm band, which coincides with the emission band of Er^{3+} ions. Optical gain in 1550 nm band is controlled by adjusting the pump power. Both the pump and probe beams are launched into the Er-doped microtoroid through a fiber taper. The coupling strength is controlled by adjusting the gap between the resonator and the fiber taper with a nano-positioning system.

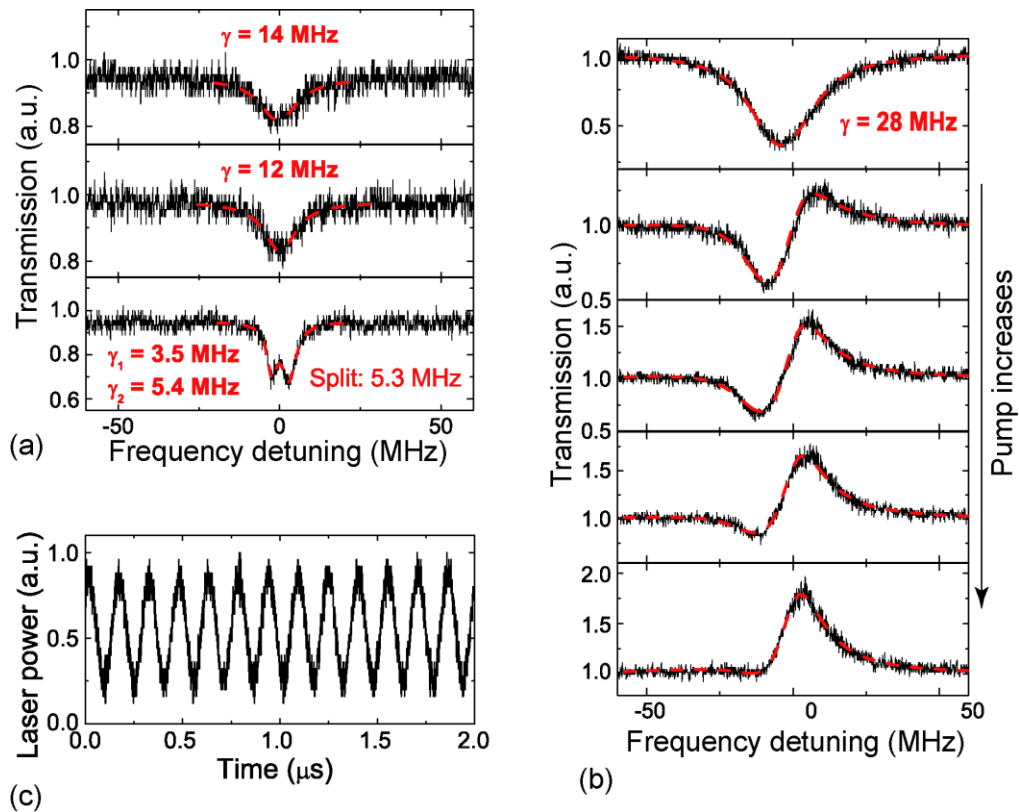


Figure 6.5 Transmission spectra of the probe light measured in the under coupling (a) and over coupling (b) regimes with increasing pump power (from top (pump power is 0) to bottom). γ denotes the resonance linewidth. Red dashed lines in (a) are Lorentzian fitting and in (b) are the best fitting in the least-squares sense using the theoretical model in Sec. 6.1.2. (c) Beat note signal from the split lasing modes.

Figure 6.5 depicts a series of transmission spectra for the probe light with increasing pump power in the under coupling and over coupling regimes. The probe light injected into the resonator is small enough to reduce the thermal effect and to avoid the gain

saturation. The launched pump power is carefully controlled in order to inhibit lasing, i.e., gain is below the lasing threshold. All transmission spectra are measured during up scan of the probe wavelength. It is seen that the gain in the active resonator affects the split modes differently in the under coupling and over coupling regimes.

In the under coupling regime (Figure 6.5(a)), before the gain medium is excited, a single resonant dip is observed with linewidth of 14 MHz, corresponding to $Q \sim 1.4 \times 10^7$. As the pump power increases, linewidth of the resonant mode narrows down which eventually allows resolving the mode splitting. This is reflected as the doublet resonant dips in the transmission spectrum with a splitting of 5.3 MHz. In the over coupling regime (Figure 6.5(b)), no doublet dips are observed as the pump power increases. This is because condition $|2g| > \Gamma + \kappa_{\text{ex}}$ is not satisfied due to the large taper-cavity coupling loss κ_{ex} . Instead, we can identify a resonant peak and a resonant dip in the transmission spectra for certain gain values. This is the result of the amplified ASM (peak) and the attenuated SM (dip) in the resonator, i.e., gain overcomes the loss of the ASM but is still smaller than the loss experienced by the SM. Theoretical fittings in Figure 6.5(b) using the model in Sec. 6.1.2 show good agreement with the experimental data.

Further increase of the pump power leads to lasing. In the presence of mode splitting, the laser mode splits into two. When detected by a photodetector, the two split laser modes interfere resulting in a beat note signal as shown in Figure 6.5(c). Details of mode splitting in a laser cavity will be discussed in Sec. 6.2.

Figure 6.6 shows the transmission and reflection spectra of mode splitting in an Er-doped microtoroid at 1551 nm when the launch pump power is kept constant and the taper-cavity gap gradually decreases. Variations in gap change both the pump power coupled into the resonator (i.e., pumping level, thus the gain ξ) and the coupling loss κ_{ex} , and therefore change the splitting spectrum. The numerical simulations are performed using Eq. (6.66). It is worth noting that the resonance spectra of the power transmission and reflection do not show exactly opposite shapes.

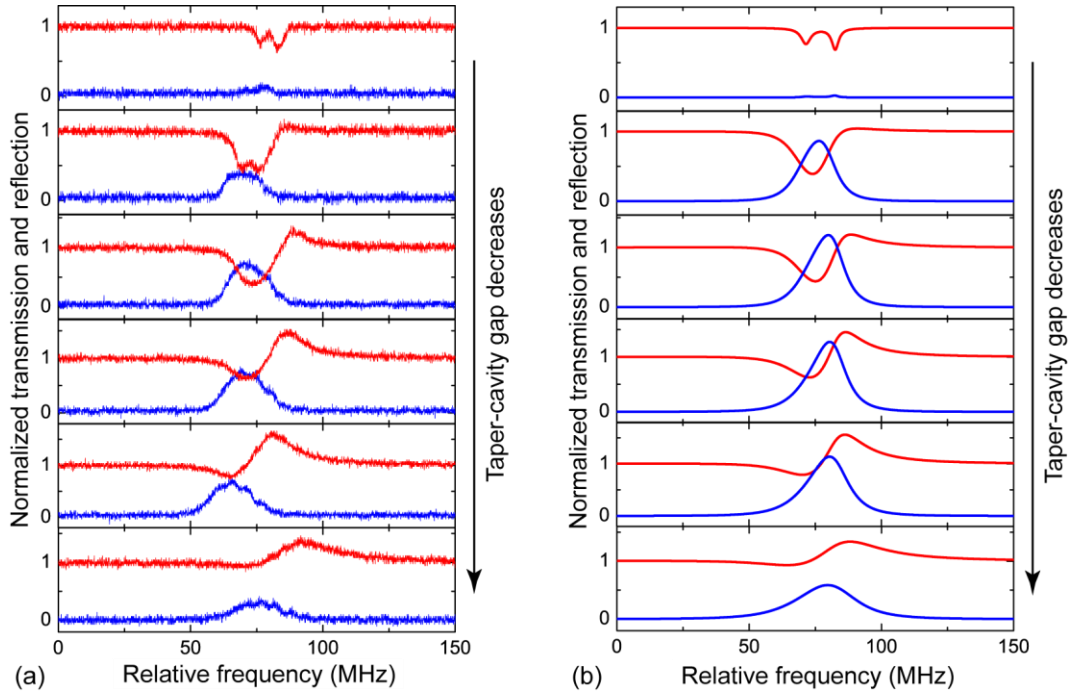


Figure 6.6 Experimental measurements (a) and numerical simulations (b) of the transmission and reflection spectra of mode splitting at different taper-cavity gap. Red curves represent the transmission and blue curves denote the reflection.

In this study, we systematically investigate the mode splitting spectrum in an active microresonator operating below the lasing threshold. Effects of the optical gain on the spectrum are studied theoretically and experimentally. Different from the simple optical amplification of a single WGM in an active resonator, transmission spectra of the split modes differ for various gain values and coupling losses, because the two split modes experience different loss mechanisms. As a result, transmission spectra with two resonant dips, two resonant peaks, or one resonant dip and one resonant peak are observed. Optical gain in active resonators enables resolving mode splitting which otherwise could not be distinguished in passive resonators. It holds the potential for ultra-sensitive nanoparticle detection and biosensing.

6.2 Above the Lasing Threshold

In this section, we study mode splitting in the lasing regime of an active resonator and introduce a heterodyne detection scheme for its monitoring. The detection scheme avoids the use of transmission spectrum via wavelength scan, thus making mode splitting phenomenon more accessible for fabricating on-chip sensors and for studying fundamental physics in microcavities [105].

6.2.1 Single-Mode Lasing

In the presence of mode splitting in a laser cavity, lasing appears at two split resonance frequencies located at ω_1 and ω_2 . Superposition of the two lasing modes, when detected by a photodetector of sufficient bandwidth, will result in a heterodyne beat note $i(t) \propto P_1 + P_2 + 2\sqrt{P_1 P_2} \cos(\Delta\omega t + \Delta\phi)$, where P_1 and P_2 are the powers of the two split modes, and $\Delta\omega = |\omega_1 - \omega_2|$ and $\Delta\phi$ are the frequency and phase differences between the split modes, respectively. Therefore, the photodetector output varies sinusoidally with the beat frequency $\Delta\omega$. The splitting can be detected through measuring the beat frequency either by using a spectrum analyzer or by applying fast Fourier transform (FFT) on the beat note signal.

We use the pump-probe experiments to demonstrate the above concept. The experimental setup is the same as shown in Figure 6.4. The Er^{3+} ion concentration in the silica microtoroid is below $7 \times 10^{18} \text{ cm}^{-3}$ to obtain continuous-wave laser operation. Figure 6.7(a) shows the lasing spectrum collected by an OSA (resolution 0.1 nm). When the pump at 1450.4 nm is above the threshold $P_{\text{th}} = 15 \text{ }\mu\text{W}$, single lasing line is observed at 1551.8 nm. Figure 6.7(b) is the transmission spectra of the pump and laser modes. The asymmetry in the spectrum during wavelength up scan and down scan is attributed to thermal effect in the cavity [59]. It is seen that the laser output increases linearly with the pump power coupled into the cavity. This can be used to estimate the lasing threshold. When the pump wavelength is fixed at the WGM resonance, temporal power

outputs of the laser and unabsorbed pump light are shown in Figure 6.7(c) and (d), respectively. The laser output shows a sinusoidal oscillation with frequency 6.52 MHz, however, such oscillation frequency is not observed in the pump output. The pump power fluctuation with a fundamental frequency of 33.0 MHz is attributed to mechanical oscillation [108].

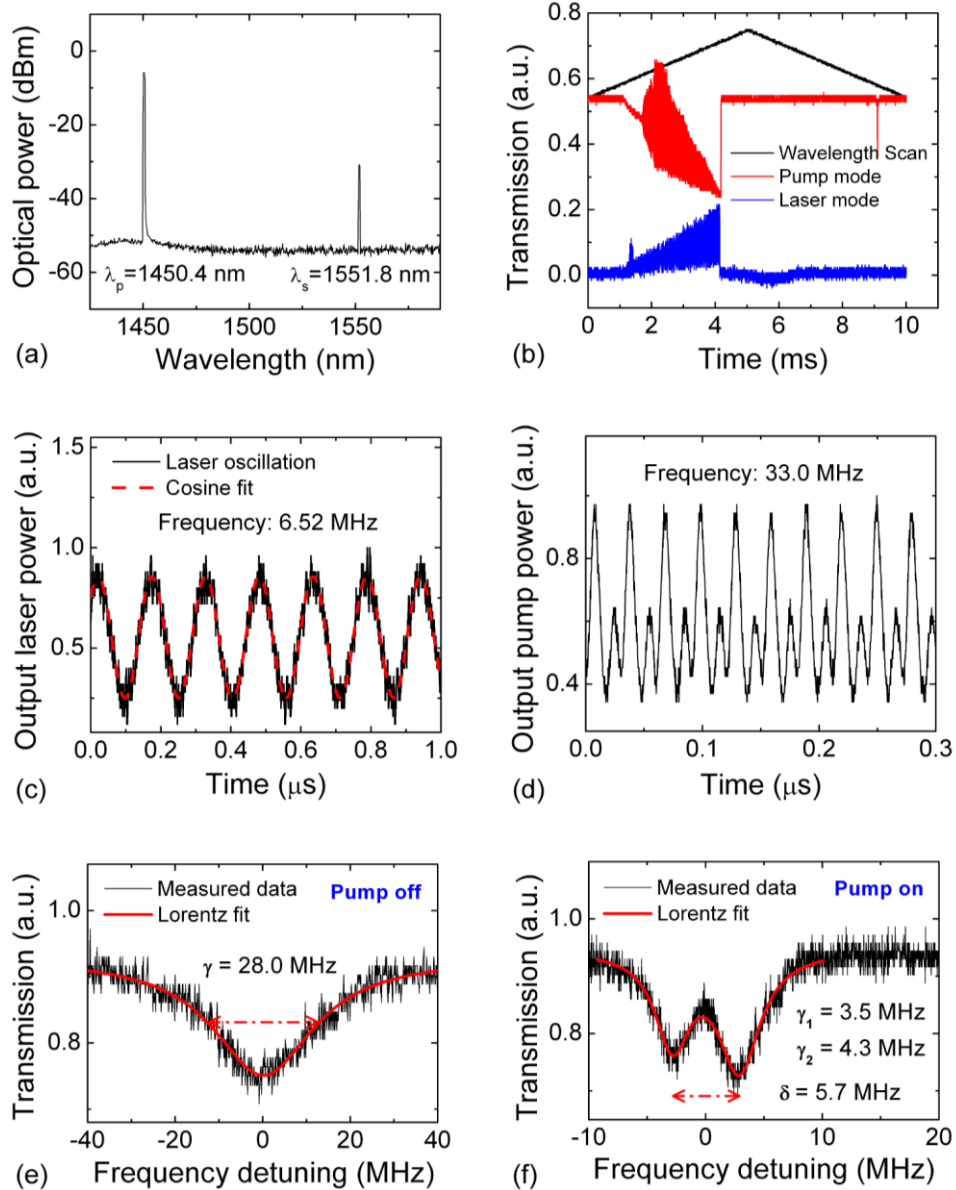


Figure 6.7 (a) Typical lasing spectrum of an Er-doped microtoroid. (b) Transmission spectra of the pump and laser light when the pump wavelength is scanned at a speed of 42.4 nm/s. The black triangle denotes pump wavelength up scan and down scan. Power output of the laser emission (c) and the transmitted pump light (d) when the pump wavelength is fixed. Red dashed line in (c) shows a cosine fitting. Transmission spectra of the probe light when the probe

wavelength is scanned and the pump laser is turned off (e) and on (f). Red lines in (e) and (f) are Lorentzian fittings. γ : resonance linewidth; δ : doublet splitting.

The observed laser power fluctuation in Figure 6.7(c) is the beat note signal formed by mixing two split lasing modes in a photodetector. If this is true, mode splitting should be observed in the transmission spectrum of the probe mode at the lasing wavelength. We confirm this with the pump-probe experiments. First, we finely scan the wavelength of the probe laser at around 1551.8 nm with a scan speed of 42.4 nm/s and record the transmission spectrum while the pump laser is off. As shown in Figure 6.7(e), a single resonant dip (probe mode) with linewidth 28 MHz corresponding to $Q \sim 6.9 \times 10^6$ is observed. Then the experiment is repeated when the pump laser is turned on and the pump power is below the lasing threshold. Figure 6.7(f) shows a doublet splitting in the transmission spectrum. The two resonances are separated by a frequency of 5.7 MHz, and their linewidths are 3.5 MHz and 4.3 MHz corresponding to $Q \sim 5.5 \times 10^7$ and $Q \sim 4.5 \times 10^7$, respectively. In the measurements, the taper-cavity gap is tuned in under coupling regime to reduce the coupling loss. The observation can be explained as follows. When the pump laser is off, resonance linewidth of the probe mode is broader than the splitting, so mode splitting cannot be resolved. When the pump laser is turned on, optical gain provided by the excited Er^{3+} ions compensates for part of the cavity losses resulting in a smaller net loss. This, in return, leads to a higher Q and a narrower linewidth revealing the splitting in the transmission spectrum. Observation of mode splitting for the probe mode in 1550 nm band confirms that origin of the detected sinusoidal laser signal is the interference of the split lasing modes in the photodetector.

Figure 6.8 presents another example of mode splitting in an Er-doped microtoroid. Laser emission occurs at 1554.6 nm while the pump is at 1451.5 nm. The laser power output fluctuates at a frequency of 26 MHz as shown in Figure 6.8(b). Figure 6.8(c) describes the evolution of the probe transmission spectrum when the pump power increases from the top to bottom panels. A frequency splitting of 24 MHz is clearly observed, which coincides with the beat frequency in Figure 6.8(b). Therefore the beat note of the split lasing modes can be employed to measure the frequency splitting.

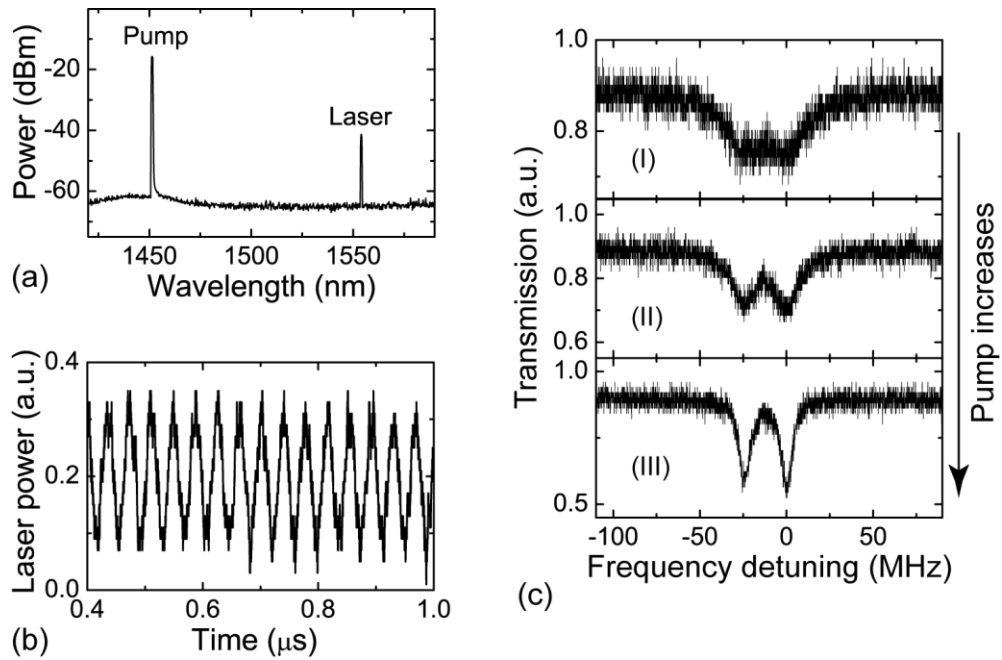


Figure 6.8 (a) Lasing spectrum. (b) Laser power fluctuations in time domain. (c) Evolution of the transmission spectrum of the probe mode as the pump power increases.

6.2.2 Multi-Mode Lasing

In an active microcavity with multi-mode lasing, each lasing mode undergoes distinct mode splitting determined by the overlap of the laser mode distribution with the scattering centers, and produces its own heterodyne beat note signal when detected by a photodetector. We perform the pump-probe experiments to confirm this claim.

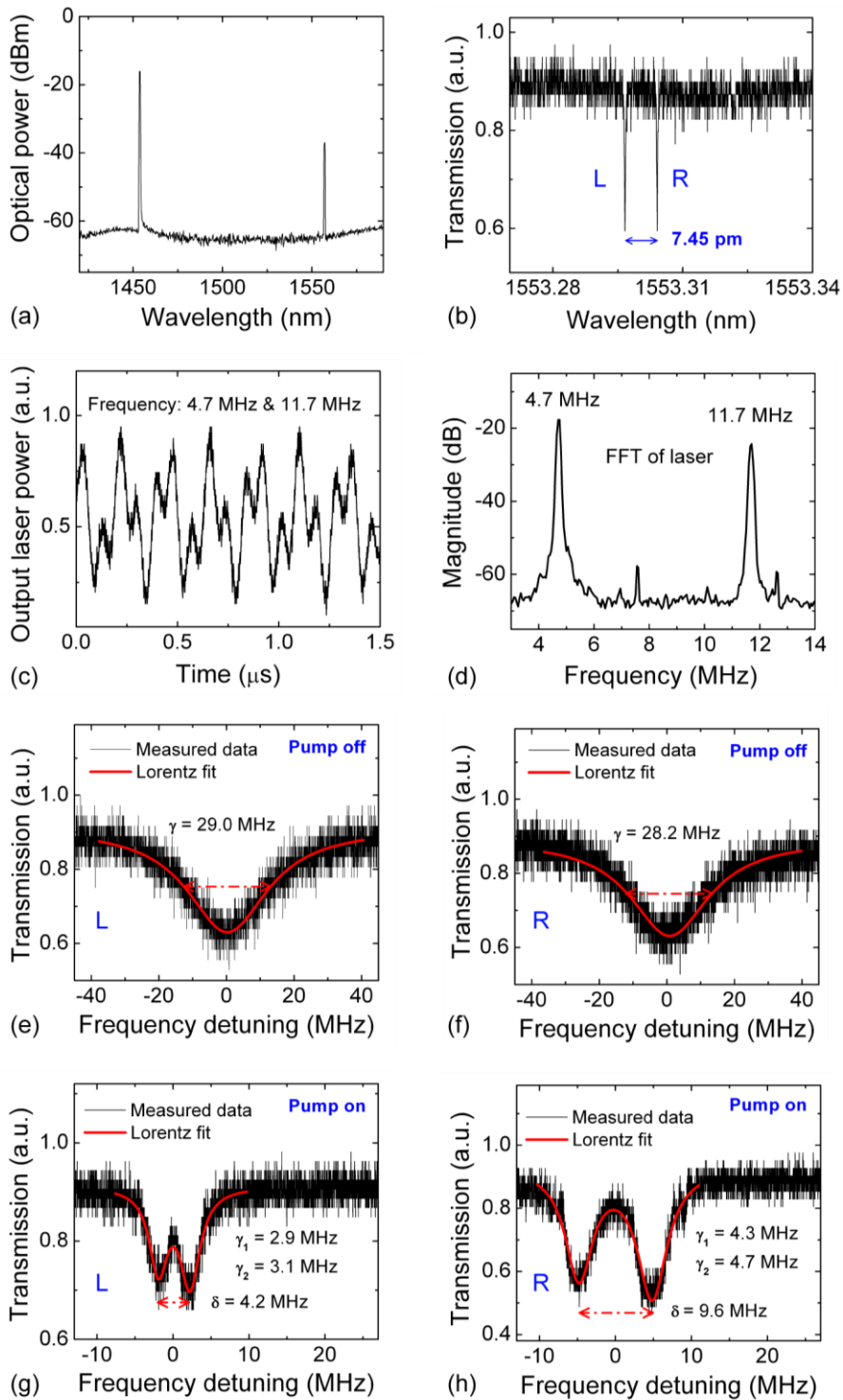


Figure 6.9 (a) Lasing spectrum. (b) Transmission spectrum of the probe light at the lasing wavelength when the pump laser is off. (c) Laser power output. (d) FFT spectrum of the laser signal in (c). (e-f) Zoom-in of the two resonant modes in (b). (g-h) Transmission spectra of the two resonant modes in (b) when the pump laser is turned on.

We choose an Er-doped microtoroid lasing at two different wavelengths to study the effects of multi-mode lasing on the beat note signal. The lasing spectrum is shown in Figure 6.9(a). There are two closely spaced lasing frequencies, however, the resolution of the OSA is not high enough to resolve them. This is confirmed by the two resonant modes in the probe transmission spectrum at the lasing wavelength in Figure 6.9(b). The laser power output from this two-mode microlaser is no longer a single frequency sinusoidal oscillation (Figure 6.9(c)). FFT in Figure 6.9(d) reveals two frequency components at 4.7 MHz and 11.7 MHz, suggesting that the two lasing modes experience different mode splitting. This is demonstrated by the transmission spectra in Figure 6.9(e-h). Without pumping the resonator, transmission spectrum at the lasing wavelength shows two adjacent WGMs separated by 7.45 pm (926 MHz) with linewidths of 29.0 MHz (Figure 6.9(e)) and 28.2 MHz (Figure 6.9(f)). When the pump laser is turned on, gain from the excited Er^{3+} ions starts compensating for the cavity losses and doublet splitting shows up for both WGMs (Figure 6.9(g) and (h)). The estimated splitting amounts from the transmission spectra are consistent with the beat frequencies in Figure 6.9(c) and (d).

The results indicate that, in the case of multi-mode lasing, each individual lasing mode experiences different mode splitting depending on its mode distribution. The resultant beat note is the superposition of multiple single-frequency sinusoidal signals and carries the information of mode splitting for each lasing mode. Mode splitting for multiple lasing in an active resonator can be utilized to decrease measurement errors in detecting and characterizing local changes on or around the resonator [13].

6.2.3 Influence of Thermal Effect

The discrepancy between the splitting amount estimated from the transmission spectrum and the beat frequency in Figure 6.7, Figure 6.8, and Figure 6.9 might be attributed to thermal effect in the resonator during wavelength scan, which leads to resonance frequency shift and linewidth broadening [59]. To show the influence of

thermal effect, we fix the pump power and wavelength, and measure the transmission spectrum of the probe mode at different input power P_s and wavelength scanning speed v_s of the probe light.

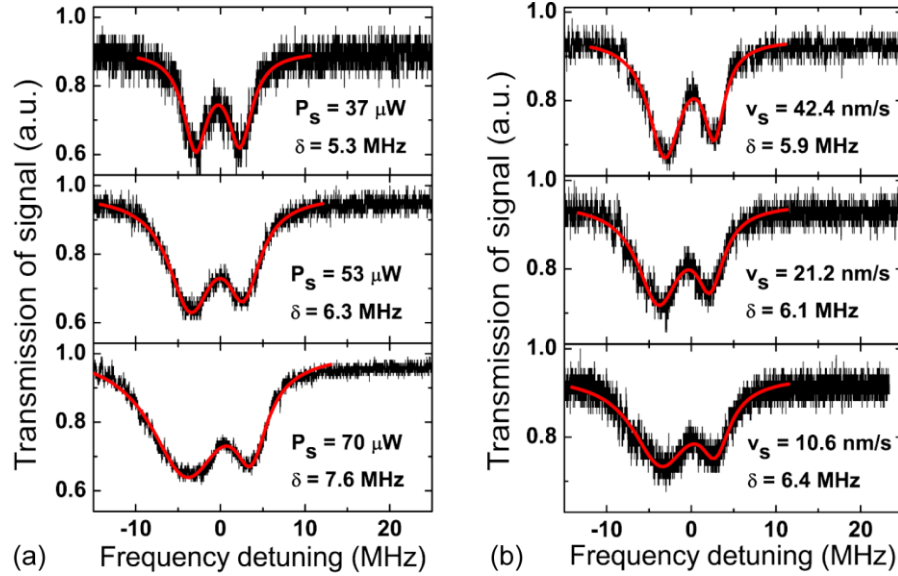


Figure 6.10 Effects of power P_s (a) and wavelength scanning speed v_s (b) of the probe laser on the mode splitting. In (a), the scan speed is $v_s = 42.4$ nm/s, and in (b), the power is $P_s = 48$ μ W.

As shown in Figure 6.10, the doublet splitting increases with the increasing probe power and the decreasing wavelength scanning speed. The broadened linewidth can be explained by the fact that higher power and lower scan speed induce larger temperature increase in the resonator. In the experiments, P_s and v_s can be optimized to minimize the effect of thermal heating on mode splitting estimation. In the heterodyne detection scheme, however, such issue is avoided because the splitting is detected from the beat note without the need for wavelength scan.

We investigate the effects of pump power and taper coupling condition on mode splitting measurement in the heterodyne scheme. As observed in Figure 6.11(a), the beat frequency does not show obvious change as the pump power increases. Figure 6.11(b) depicts that the beat frequency decreases slightly with increasing taper-cavity gap, e.g., an increase of 0.2 μ m in the gap leads to a splitting change less than 1%. These results suggest that the heterodyne technique provides more stable readings of mode splitting.

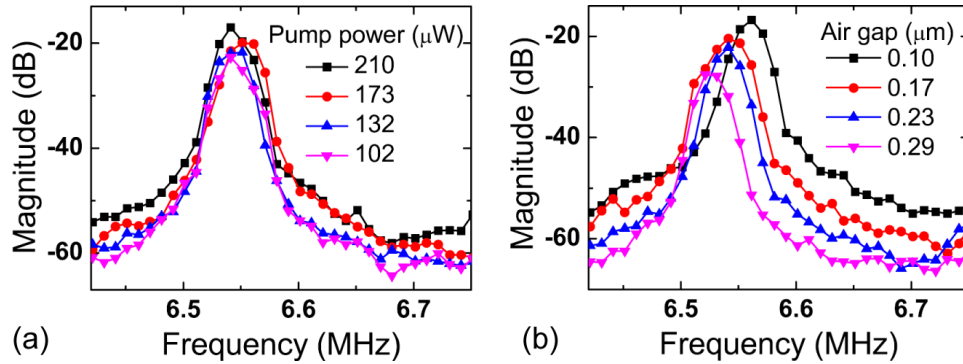


Figure 6.11 Effects of pump power (a) and taper-cavity gap (b) on FFT spectrum of the beat note signal from the split lasing modes.

6.2.4 Sensing

The heterodyne detection scheme is not limited to the intrinsic splitting measurement. It is also capable of detecting scatterers intentionally introduced into the mode volume of a microcavity laser. In the experiments, we use a fiber tip (size $< 1\mu\text{m}$) as the external scatterer and gradually approach it towards the resonator surface. As shown in the inset of Figure 6.12, the cone-like shape of the tip allows us to simulate a scatterer with increasing size interacting with the WGM field.

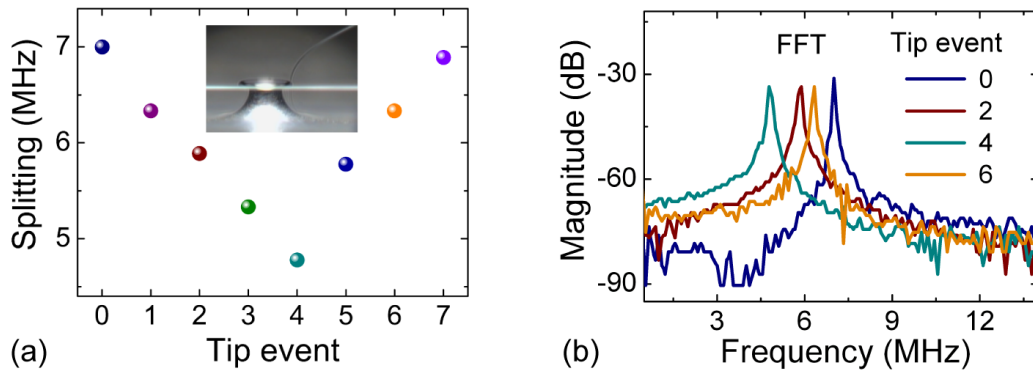


Figure 6.12 (a) Effect of an intentionally introduced scatterer (fiber tip) on the mode splitting in an active microcavity. Inset: Micrograph showing a fiber tip approaching a microtoroid surface. (b) FFT of the beat note signal at different tip positions (scatterer size).

Figure 6.12 depicts the measured heterodyne beat frequency as a fiber tip is gradually pushed towards the microtoroid. When the fiber tip is far away from the resonator, an

intrinsic mode splitting of 7 MHz is observed (event 0 in Figure 6.12(a)). As the fiber tip approaches the resonator, mode splitting (beat frequency) first gradually decreases and then starts increasing. This can be explained by the size and position of the tip in the WGM mode volume. Since in our experimental setting, silica fiber tip can only red shift the resonance wavelength, for the small tip size, the decreasing splitting in Figure 6.12 indicates that the split mode with higher frequency is strongly disturbed and shifted to the lower frequency side. As the tip size increases, either a crossing or an avoided crossing in the split frequencies may take place, leading to an increase in the splitting [137].

In conclusion, lasing in active resonators allows measurement of mode splitting from a heterodyne beat note formed by mixing the split lasing modes in a photodetector. This self-heterodyning scheme provides a wavelength scan free and compact tool for detecting nanoparticles in the resonator mode volume and for investigating light-matter interactions. It should be mentioned that the intrinsic splitting in the laser cavity will not affect the nanoparticle sensing, since the sensing is implemented by monitoring the relative changes in the mode splitting.

Chapter 7

Microlasers for Single Nanoparticle Detection

It has been demonstrated that mode splitting in passive resonators can be used to detect single nanoparticles entering the resonator mode volume [14,107]. The detection is limited by the cavity Q factors which define the resonance linewidths of the WGMs. In chapter 6, we showed that by using microcavity lasers, the WGM linewidths are narrowed indicating the potential to improve the detection limit.

In this chapter, we introduce single nanoparticle and virus detection using microcavity lasers [13]. The detection approach relies on measuring changes in the beat note that is produced when an ultra-narrow emission line from a WGM microlaser is split into two modes by a nanoscale object, and these two modes then interfere. The ultimate detection limit is set by the laser linewidth, which can be made much narrower than the resonance linewidth of any passive resonator [100,145]. This means that microlaser-based sensors have the potential to detect objects that are too small to be detected by passive resonator based sensors.

7.1 Experimental Setup

A WGM microlaser supports two frequency-degenerate but counter-propagating lasing modes, which are confined in the resonator with the evanescent tails probing the surrounding medium. A particle that enters the evanescent field of the microlaser couples the degenerate lasing modes to each other via intracavity Rayleigh back-scattering, and thus leads to laser frequency splitting. Spectral distance between the split

lasing modes is determined by particle polarizability α and particle position in the mode volume [106,138-139]. Thus, any change in α is translated into a change in the frequency splitting. Any particle binding event inducing excess polarizability is observed as a change in the splitting [14,107]. A simple and cost-effective method of measuring the frequency splitting is to mix the split laser modes in a photodetector, the output of which is a heterodyne beat note with the beat frequency corresponding to the frequency splitting [105]. Therefore, nanoparticle adsorption events can be revealed in real time by monitoring the beat note.

The nanoscale objects we measured in the experiments included PS nanoparticles (Thermo Scientific, 3000 series, radii range 15~50 nm, CV=16.8% for radius of 30 nm and CV=5.1% for radius of 50 nm. CV: coefficient of variation, defined as the ratio of standard deviation to mean), gold (Au) nanoparticles (BBInternational, radii range 10~100 nm, CV<8% for all particle size), and Influenza A (InfA) virus (Charles River Laboratories International Inc., type: X-31, A/Aichi/68 (H3N2)).

7.1.1 Measurements in Air

In the experiments performed in air, Er-doped microtoroids fabricated from the sol-gel silica film are used as the microlasers [12,85]. The concentration of Er³⁺ ions in silica is $\sim 5 \times 10^{18}$ ions/cm³, which assures continuous-wave laser operation. The resonators are 20~40 μm in diameter, and have Q factors of 6×10^6 at 1460 nm. The experimental setup is shown in Figure 7.1. The fiber taper coupled microlaser is continuously pumped by a light source at 1460 nm within the Er³⁺ absorption band. Laser emission in 1550 nm band is monitored by a photodiode connected to an oscilloscope. Data is collected at an acquisition rate of 10 Frames/s. Frequency components of the laser beat note are extracted via FFT.

A nozzle connected to a differential mobility analyzer (DMA) was used to deliver particles onto the microlaser. The particle delivery system works as follows [14].

Polydisperse droplets containing nanoparticles are carried out from the particle solution by compressed air using collision atomizer. Subsequently the solvent in the droplets is evaporated by silica gel desiccant. A radioactive source neutralizes the particles to ensure a well-defined charge distribution. The particles are then classified according to their electrical mobility using the DMA. Finally, particles within a narrow mobility range (i.e., particle size deviation within 5%) exit through the output slit and are delivered to the microlaser via a micro-nozzle. The concentration of the particle solution and the air flow rate from the nozzle are carefully controlled to ensure that the chance of delivering more than one particle within one frame acquisition time window is very low.

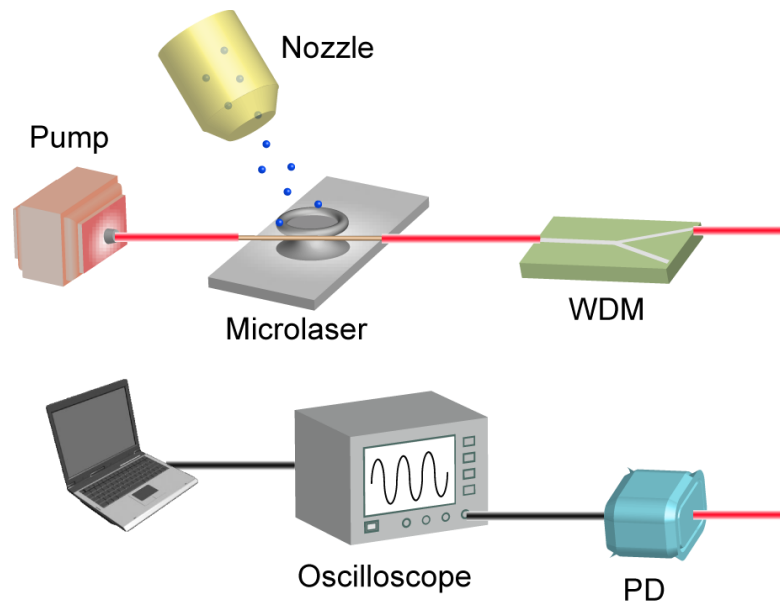


Figure 7.1 Schematic of the experimental setup. The pump light and the split lasing modes are separated using a wavelength division multiplexer (WDM). Split lasing modes are mixed in a photodetector (PD) leading to a heterodyne beat note signal. A nozzle continuously delivers nanoparticles onto the microtoroid laser, which translates changes in polarizability into changes in frequency splitting.

The concept of the detection is illustrated in Figure 7.2. Before the arrival of nanoparticles, there is a single lasing mode with constant laser intensity (i). With the arrival of the first nanoparticle, lasing mode splits into two leading to a beat note whose frequency corresponds to the frequency splitting (ii). Subsequent particle binding event changes the beat frequency (iii). Since the split lasing modes reside in the same microlaser, environmental noise such as temperature fluctuations (illustrated by a heat

source placed under the sample) affects both modes in the same way leading to a self-referencing scheme (iv). Thus, although each split mode undergoes spectral shift, the splitting between them does not change, making this detection scheme resistant to environmental noises [133].

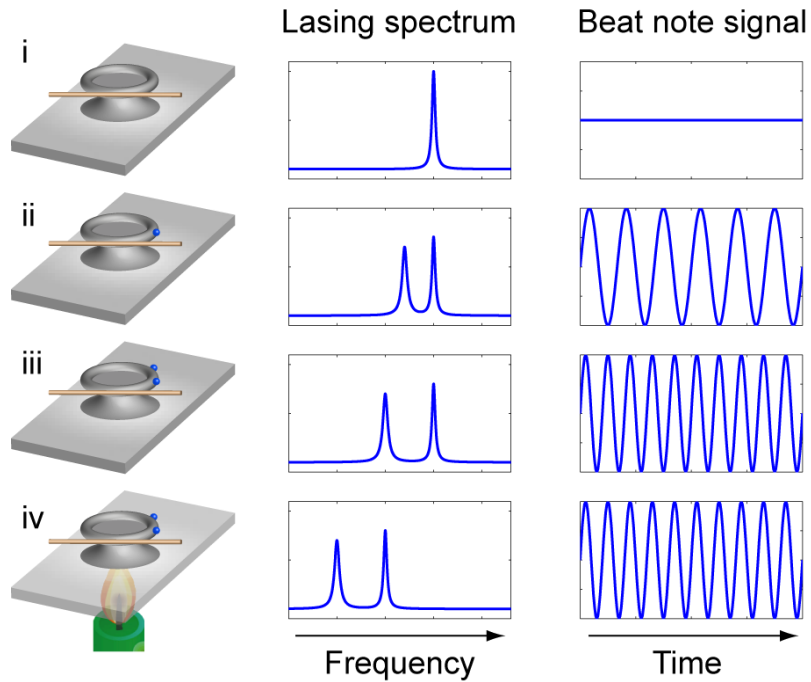


Figure 7.2 Illustration showing the detection of nanoparticles using mode splitting in a microcavity laser.

7.1.2 Measurements in Water

We test the applicability of using a microlaser for single nanoparticle detection in aqueous environment. The experimental setup is similar to that used for measurements in air except that the fiber taper and the microlaser are immersed in a 2-mL water chamber. The chamber is connected to a syringe pump with infuse and withdraw functions through inlet and outlet ports. Nanoparticle solution is pumped into the chamber continuously and particles are flown from one end of the chamber to the other end during which they bind to the microlaser occasionally [146-147].

In water experiments, Er-doped microtoroids cannot be used due to the high optical absorption of water in 1550 nm band. It degrades the resonator Q factor to values less than 10^5 which is not sufficient to generate laser emission with pump power at sub-mW level [111]. Since water absorption in 1040 nm band is much lower than that in 1550 nm band, we use Yb-doped microtoroids, which generate laser emission in 1040 nm band when pumped in 970 nm band, in water experiments [126]. We observed laser emission in water with Yb^{3+} concentration of 5×10^{19} ions/cm³ and microtoroid diameter of 100 μm . Because of the small refractive index contrast between silica and water, large resonator size is required to reduce the radiation loss, giving rise to Q factors of $\sim 6 \times 10^5$ in 970 nm band.

7.2 Single Nanoparticle Detection Results

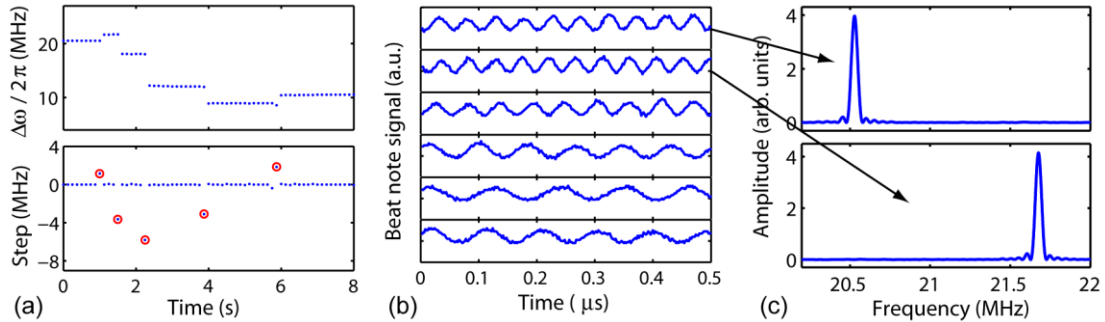


Figure 7.3 (a) Recorded real-time beat frequency when gold nanoparticles (radius $R = 50$ nm) are continuously deposited onto a microlaser. Lower panel of (a) shows the frequency difference of the beat note between two consecutive detected data points. Five particle binding events marked with red circles are clearly observed from the discrete jumps. (b) Beat note signals corresponding to each time segment in (a). (c) FFT spectra of the first and second beat notes from top in (b) as marked by black arrows. Obvious shift of the FFT frequency is observed corresponding to the first particle binding event in (a).

Single particle binding events are translated into discrete frequency changes of the heterodyne beat signal. Thus, particle detection and counting are achieved by monitoring the beat frequency. Figure 7.3 shows examples of the recorded beat frequency, beat note signal, and corresponding frequency spectra when gold nanoparticles are continuously deposited onto an Er-doped microtoroid laser. Each

particle binding event is signaled by a change in the frequency splitting reflected as a discrete change in the laser beat note frequency.

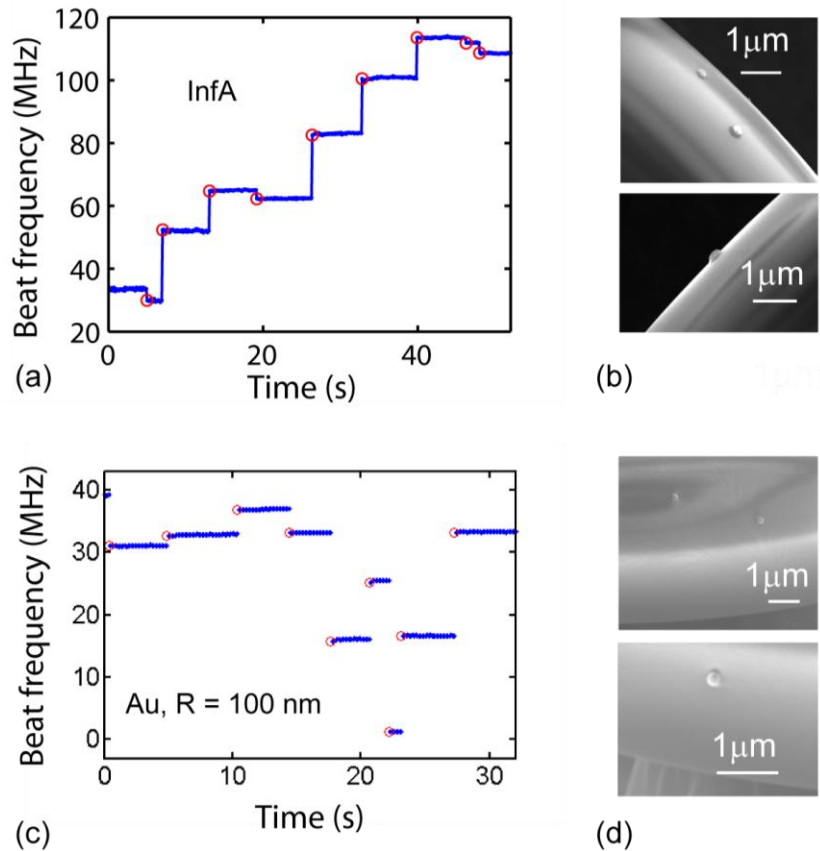


Figure 7.4 Beat frequency with time in response to the arrival of InfA virions (a) and gold nanoparticles of $R = 100$ nm (c) onto a Er-microlaser continuously. Red circles denote individual particle binding events. The major (minor) diameter of the microtoroid laser is 47 (3.7) μm for InfA measurement and 47 (4) μm for Au particle measurement. The SEM images show InfA (b) and gold particles (d) attached on the microlaser surface.

Figure 7.4 shows the evolution of beat frequency as InfA virions and Au particles enter the mode volume of a microlaser one by one. Each discrete upward or downward jump in the beat frequency indicates a single particle adsorption event. The directions and heights of the discrete jumps are related to the polarizability of each arriving particle and the location of each particle with respect to the previously adsorbed particles. Due to the trapping force from the resonator field, desorption of nanoparticles from the resonator happens rarely. In Figure 7.4(a), the InfA induced splitting shows larger upward jumps than downward jumps resulting in a faster increase of the frequency

splitting, which is different from the observation for Au nanoparticles in Figure 7.4(c). This can be explained by the fact that InfA virions have larger contact areas with the resonator surface leading to stronger light-matter interactions. This is clearly observed from the SEM images in Figure 7.4(b) and (d).

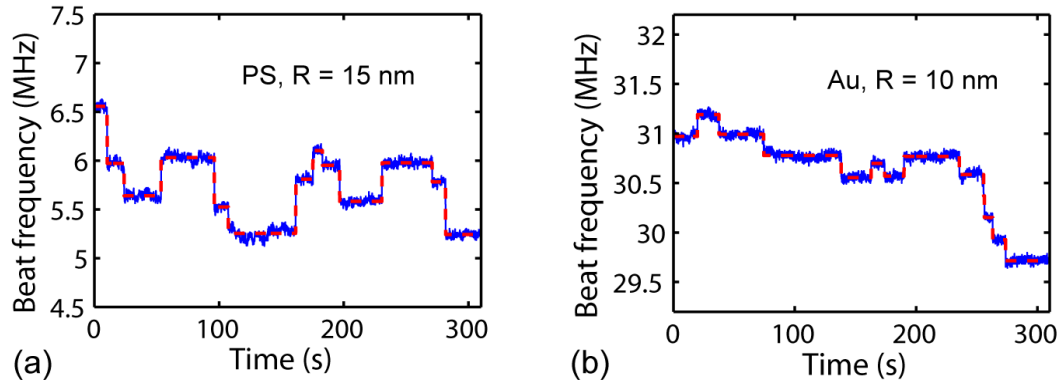


Figure 7.5 Recorded beat frequency with time when PS nanoparticles of radius 15 nm (a) and Au nanoparticles of radius 10 nm (b) are deposited on the microlaser surface continuously. Red lines are drawn at mean of the measured beat frequencies for each binding event. The major diameter of the Er-doped microtoroid is $27\ \mu\text{m}$, and the minor diameter is in the range of $3.5\sim 4\ \mu\text{m}$.

Figure 7.5 presents the measurement results for PS nanoparticles of mean radius $R=15$ nm and Au nanoparticles of $R=10$ nm, indicating the measured detection limit using the proposed sensing scheme. It surpasses the reported detection limit using passive microresonators [13-14].

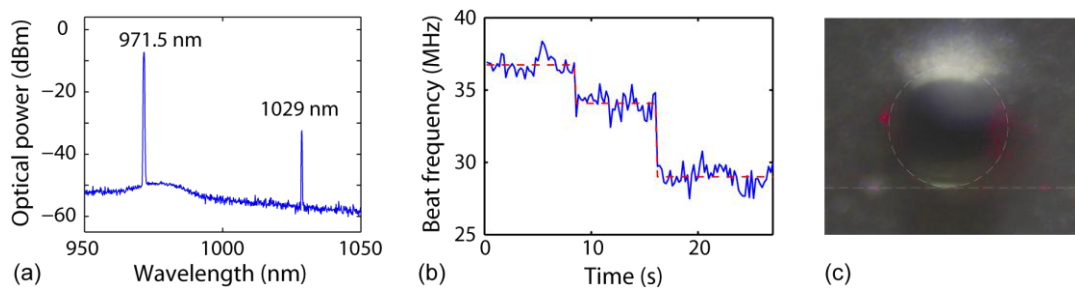


Figure 7.6 Nanoparticle detection in water. (a) Lasing spectrum of an Yb-doped microtoroid laser in water. (b) Changes in beat frequency with time after PS nanoparticle suspension ($R = 30$ nm) is injected into the chamber. The major (minor) diameter of the microlaser is 105 (4.5) μm . (c) Top view of the microlaser in water with a particle attached on its ring. The particle becomes visible due to scattering of red light coupled into the microlaser. The white light at the top is due to the illuminating light from the microscope. The white dotted lines are drawn to denote the boundary of the microlaser and the fiber taper. The red arrows show the direction of light propagation in the fiber taper.

Figure 7.6 shows the detection of PS nanoparticles in water using an Yb-doped microtoroid laser. The laser emission occurs at 1029 nm when pumped at 971.5 nm. We also demonstrated the detection of InfA viruses in water. As shown in Figure 7.7, four binding events are clearly observed from the discrete beat frequency changes. This first demonstration of particle or virus induced frequency splitting in a microlaser placed in water environment completes a crucial step for extending this highly-sensitive technique to sensing in aqueous and biological fluids.

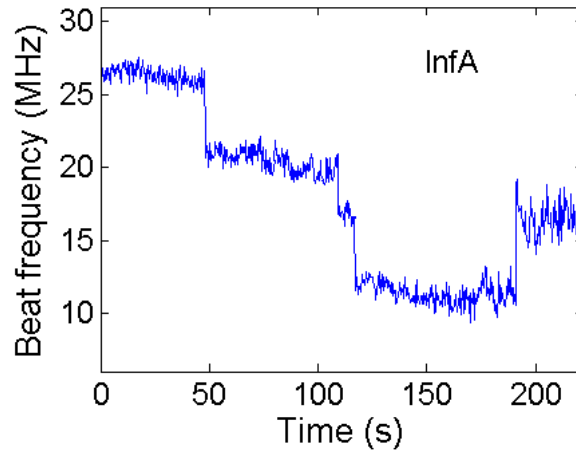


Figure 7.7 Recorded beat frequency with time when InfA virions are injected into the water chamber. The major (minor) diameter of the microlaser is 100 (8) μm .

7.3 Ensemble Measurement of Particle Size

The above detection scheme provides an easy track of laser frequency splitting, which can be used for single nanoparticle detection and counting. However, it is difficult to trace changes in the narrow laser linewidths, preventing the sizing of single nanoparticles. Here, we demonstrate theoretically and experimentally that ensemble measurements can be applied to estimate the particle size.

7.3.1 Theory

In this section, we study theoretically how the particle induced frequency splitting is related to the particle size. In the simulation, we assume particles land on random

locations on the resonator surface which is the case in our experiments. For each arriving particle, the frequency splitting shows discrete jumps with different heights. This is confirmed by numerical simulations in Figure 7.8.

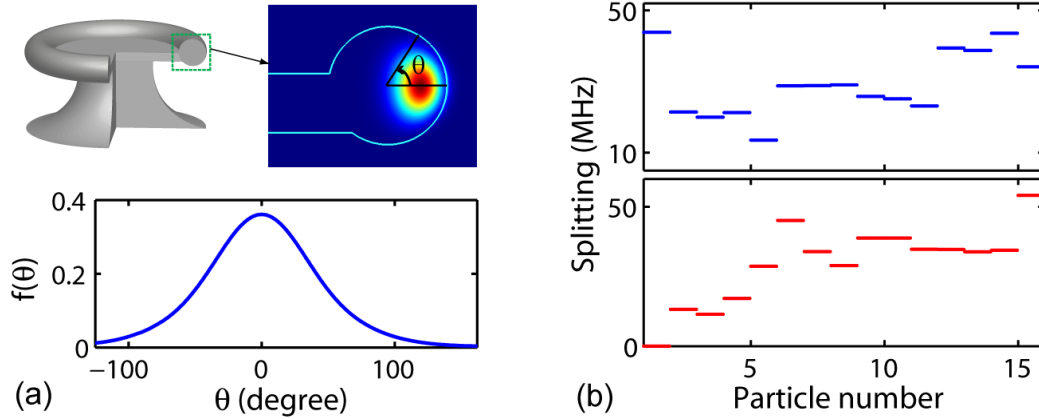


Figure 7.8 (a) Upper panel: Illustration of a microtoroid and cross-sectional electric field distribution of the fundamental WGM. Lower panel: Normalized distribution of the field magnitude f along resonator surface as a function of the polar angle θ . (b) Simulation results from Eq. (5.45) show the frequency splitting as PS nanoparticles are continuously deposited on the microtoroid. The upper and lower panels are obtained for two sets of simulations with nanoparticles placed at random positions on the resonator. Parameters used in simulations are: PS particles with radius $R = 50$ nm and refractive index $n_p = 1.59$, resonance wavelength $\lambda_c = 1550$ nm, surrounding medium with refractive index $n_m = 1.0$, and mode volume $V = 300 \mu\text{m}^3$.

Cross-sectional field distribution of the fundamental WGM in a microtoroid shown in Figure 7.8(a) implies that the optical field along the resonator surface is non-uniform, and thus light-matter interaction strength varies depending on the position of the particle on the resonator. Consequently, a single particle adsorbed on different locations in the mode volume induces different frequency splitting. Figure 7.8(b) depicts the results of Monte-Carlo simulations in which we calculate the frequency splitting of a WGM when individual PS nanoparticles of the same size are deposited onto the resonator one by one. With particles binding to random locations on the resonator surface, the resulting frequency splitting either increases or decreases with different step heights. Figure 7.9 presents the measured frequency splitting with time as gold nanoparticles are deposited onto two microlasers. No consistent trend of frequency splitting is observed with the increasing particle number.

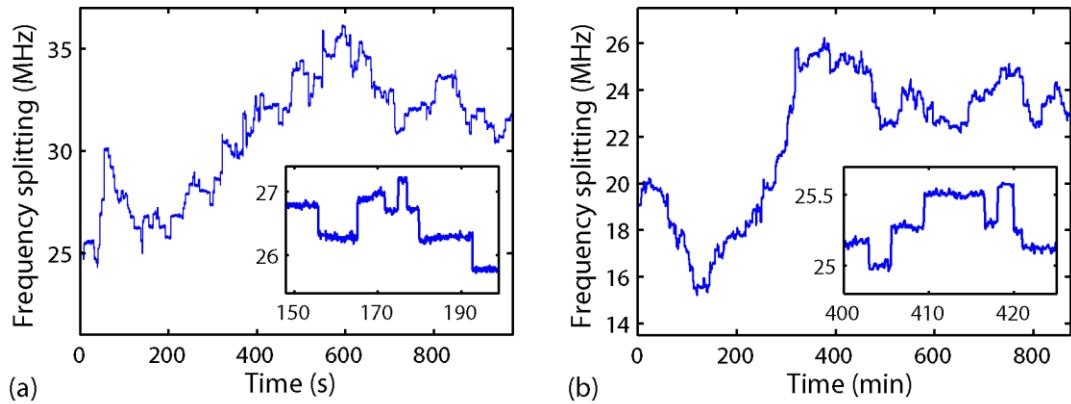


Figure 7.9 Recorded frequency splitting with time as gold nanoparticles of radius 15 nm are continuously deposited onto two microtoroid lasers (a) and (b). There are about 200 particles detected in each plot. Insets of (a) and (b) present close-up plots of frequency splitting in a short time period. Axes of the insets are the same as those of the main plots.

For particle measurement, what is important is the change in frequency splitting in response to each particle attachment, that is, how the frequency splitting of the WGM of interest changes with particle adsorption. We define the change of frequency splitting induced by the binding of the i -th particle as $\Delta S_i = S_i - S_{i-1}$ (Figure 7.10), where S_i can be obtained from Eq. (5.45). We study the distribution of ΔS and its relation to the size and number of the adsorbed particles.

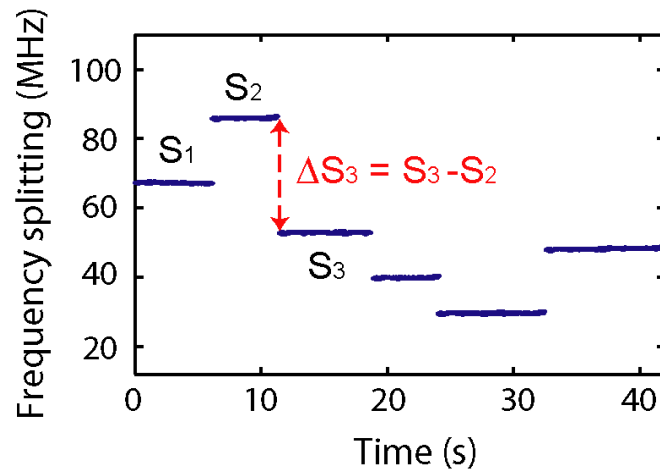


Figure 7.10 Definition of change in frequency splitting corresponding to a particle binding event.

Assuming N identical particles bind on a resonator consecutively, N discrete changes in frequency splitting (ΔS_i , $i = 1 \dots N$) are obtained. Figure 7.11 presents the histograms of

these changes ($\Delta S_1 \sim \Delta S_N$) for different particle number N and radius R . Theoretically, for a large enough number of particle binding events, the histogram of splitting changes is symmetric around 0 as shown in the bottom panel of Figure 7.11(a). We can see that N has a negligible impact on ΔS distribution when N is sufficiently large, and ΔS distribution becomes broader with increasing R . From the simulation results, the maximum possible change in frequency splitting equals to the maximum value of $2g$, i.e., $\Delta S^{\max} = \alpha f_{\max}^2 \omega_c / V$. Standard deviation ΔS^σ of the histogram is proportional to α with the coefficient determined by the distribution of particle positions on the resonator. Relying on their dependence on α , ΔS^σ and ΔS^{\max} can be used to extract the information of particle polarizability and thus particle size.

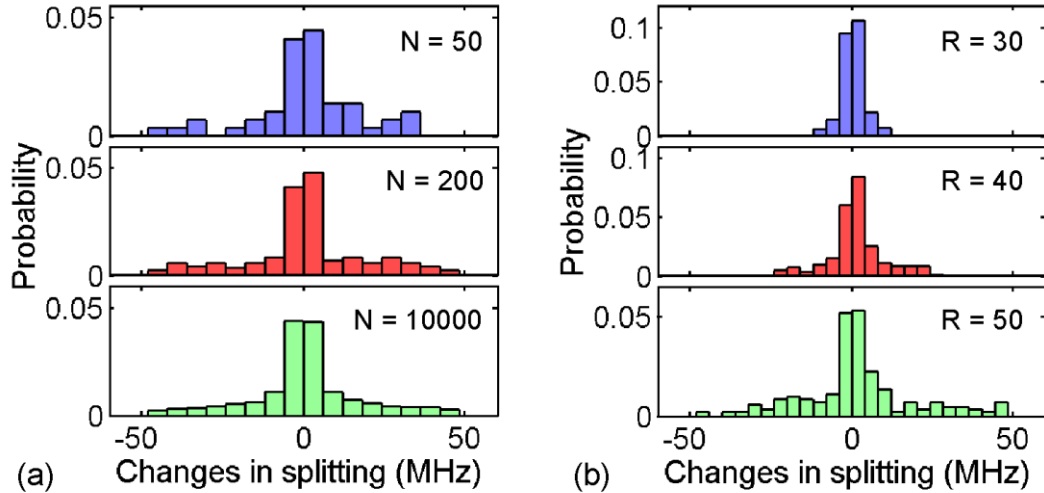


Figure 7.11 Calculated histograms of splitting changes induced by consecutive deposition of PS particles onto a microtoroid. Here $R = 50$ nm in (a) and $N = 200$ in (b). Particle radii labeled in (b) have unit of nanometer. Each histogram corresponds to one set of trial: continuously deposit N particles of radius R on the resonator, record the corresponding changes in frequency splitting, and create the histogram of those changes. Mean and standard deviation of the histograms are listed in the form of mean/deviation with unit of MHz: (a) 0.706/16.795, 0.847/18.243, 0.447/17.407 from top to bottom; (b) 0.242/3.372, 1.091/8.592, 1.659/17.545 from top to bottom.

In each set of particle deposition experiment, ΔS^σ and ΔS^{\max} vary from their expected values due to the uncontrollable particle positions. We conduct numerical simulations to quantitatively study the dependence of their expectations on particle size. The process is described as follows. For N binding particles of radius R , splitting changes $\Delta S_1 \sim \Delta S_N$ are calculated to get ΔS^σ and ΔS^{\max} . This simulation is repeated 10000 times to obtain their

mean values which are plotted as a function of R in Figure 7.12. Linear dependence of the expectations of ΔS^σ and ΔS^{\max} on R^3 is observed from curve fittings. This composes the basic principle for ensemble measurement to obtain the particle size.

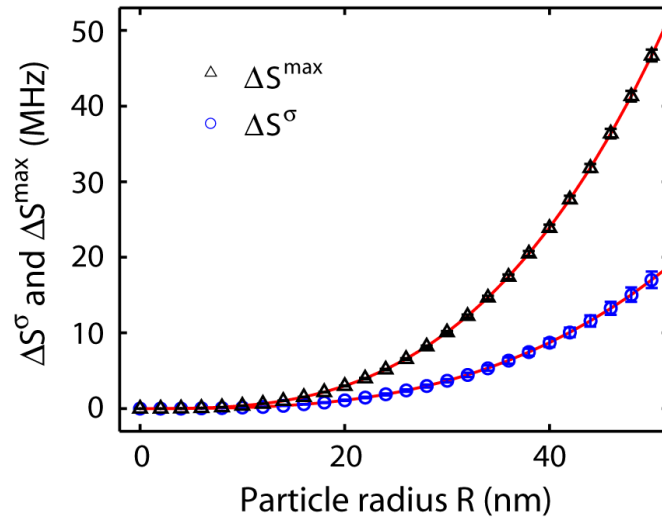


Figure 7.12 Expectations of ΔS^{\max} (black triangles) and ΔS^σ (blue circles) as a function of R for PS nanoparticles. The number of particle binding events is $N=200$. The data points and error bars denote the mean and standard deviation of 10000 times repeated calculations. Red solid curves are polynomial fittings that scale with R^3 .

In real measurement, it is impractical to repeat the detection for 10000 times to get the expectations of ΔS^σ and ΔS^{\max} . Their values from a single set of measurement could be used to approximate the expectations. In this case, the detected particle number N becomes crucial for the measurement accuracy. For a limited N , ΔS^σ and ΔS^{\max} in a single measurement may vary a lot from their expectations, leading to a large measurement error. However, such error can be reduced by increasing N . As demonstrated in Figure 7.13(a) and (b), the fluctuation ranges of ΔS^σ and ΔS^{\max} are smaller for a larger number N . Figure 7.13(c) shows the calculated mean and standard deviation of ΔS^σ and ΔS^{\max} as a function of N . The larger the N , the closer ΔS^σ and ΔS^{\max} of a single measurement would be to their expectations, and therefore more accurate the particle size measurement is.

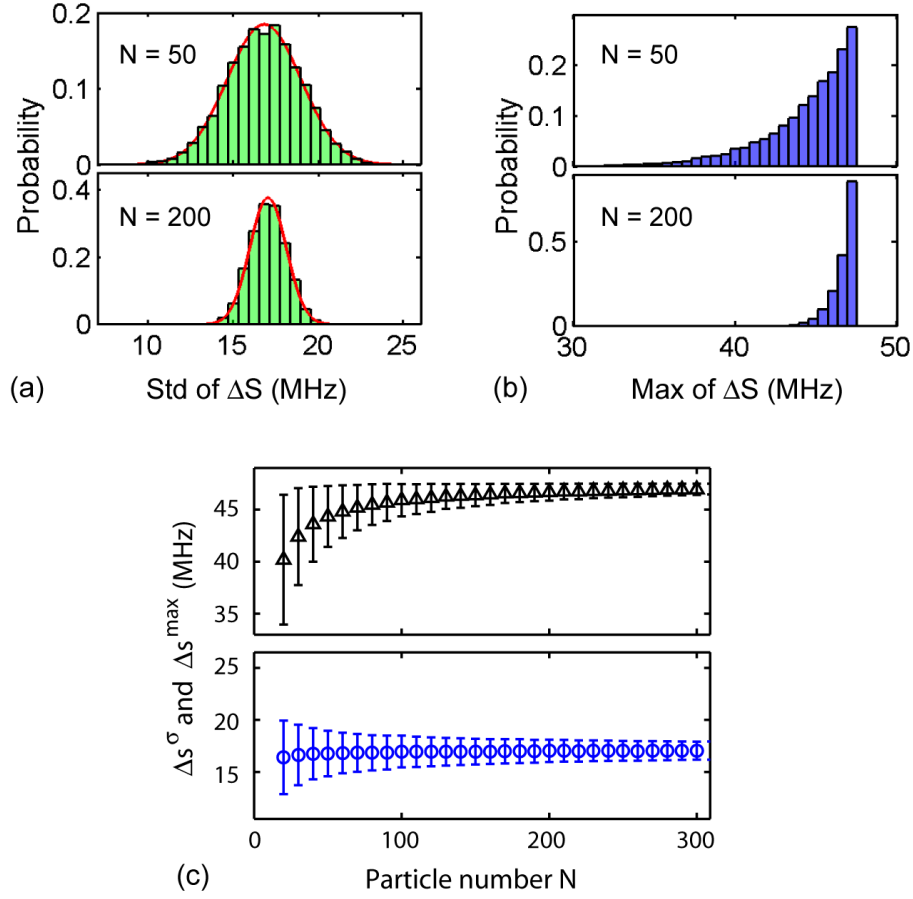


Figure 7.13 Distributions of ΔS^{σ} (a) and ΔS^{\max} (b) from 10000 times repeated simulations for PS particle ($R = 50$ nm) deposition with different N . Solid red lines in (a) are Gaussian fittings. (c) Mean (data points) and standard deviation (error bars) of ΔS^{\max} (black triangles) and ΔS^{σ} (blue circles) as a function of N . The results are obtained from 10000 times repeated simulations.

In the ensemble measurement of particle binding events, by knowing the WGM field distribution f and mode volume V , particle polarizability α can be obtained directly from the expression $\Delta S^{\max} = \alpha f_{\max}^2 \omega_c / V$. However, due to the many supported WGMs in a resonator, it is difficult to determine which the measured mode is. In this case, reference particles can be applied to measure α or R of unknown particles. For example, when two groups of particles of the same material but different sizes are deposited on the same resonator, the ratio of the particle size is indicated by the ratio of ΔS^{σ} or ΔS^{\max} from two particle groups, where the effects of f , V , and particle position are cancelled out.

It should be noted that estimation of α using ΔS^{\max} is a lower limit, since there is the possibility that all the detected splitting changes are smaller than the possible maximum value. On the other hand, ΔS^{\max} is easily to be perturbed by unexpected contaminants or dusts, i.e., any dust or contaminant induced splitting change might shift the maximum jump magnitude to a higher value and thus induce an estimation error. In our measurements, ΔS^{σ} is measured for particle size estimation.

7.3.2 Experiments

We performed experiments with gold particles of $R_1 = 15$ nm and $R_2 = 25$ nm to confirm the size estimation with the above approach. Particles are deposited one by one at random locations on the microlaser surface. Figure 7.14(a) and (b) show the measured beat frequency for the two particle sizes. It is obvious that the change in beat frequency for 25-nm particles is larger than that for 15-nm particles. All measurements are performed using the same microlaser and the same lasing mode to minimize the cavity and mode related effects. The detection of a total number of 816 Au nanoparticles implies that small nanoparticles do not cause significant change in the linewidth of the lasing modes. After collecting statistically significant number of discrete changes in the beat frequency, we constructed the histograms as presented in Figure 7.14(c). The histogram for $R_2 = 25$ nm particles has a wider distribution than that for $R_1 = 15$ nm particles which is consistent with the simulation results. The histograms can be used to extract the polarizability and thus the size of unknown particles by using reference particles.

In the experiments, we can only detect changes in beat frequency that are larger than the noise level, that is, if a particle induced splitting change is less than the noise level, it will go undetected. Thus, binding events which introduce very small splitting changes cannot be detected and the information of such events is lost. This is observed as the gap around 0 in the histograms depicted in Figure 7.14(c). Therefore, we cannot get the size information by simply applying the relation $\Delta S^{\sigma} \propto R^3$. For example, the ratio of

ΔS^σ for 25-nm and 15-nm particles is 3.51, which is very different from the ratio $R_2^3/R_1^3=4.63$.

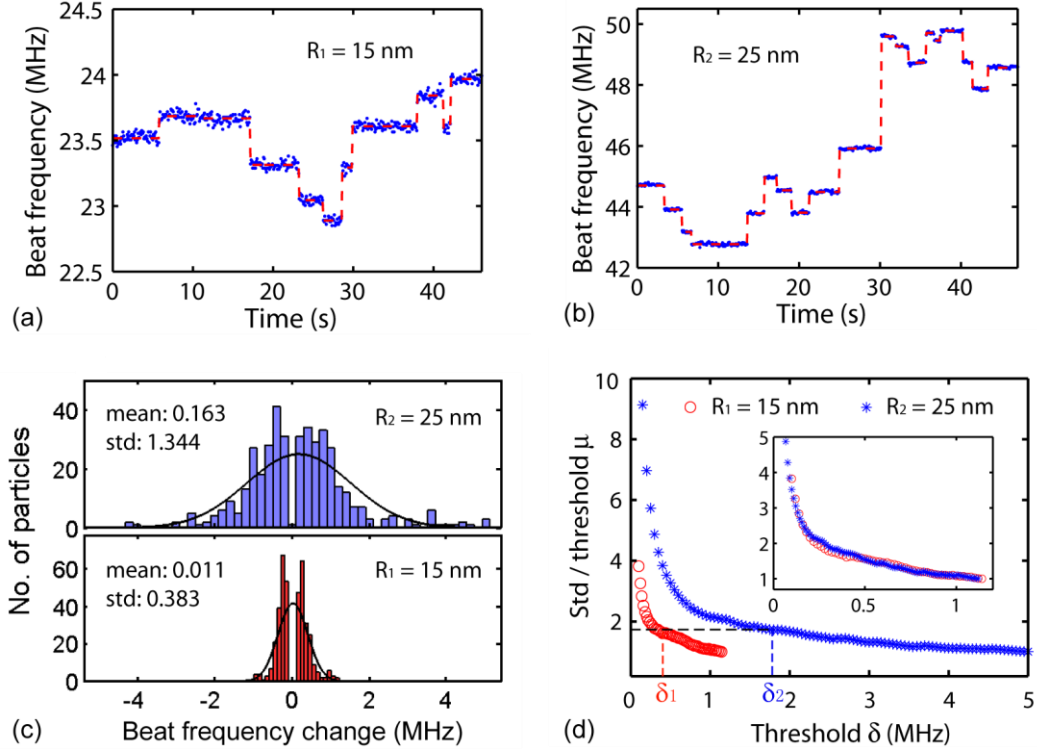


Figure 7.14 Estimating particle size with ensemble measurement. Real time records of beat frequency when Au nanoparticles of radius $R_1 = 15$ nm (a) and $R_2 = 25$ nm (b) are deposited one by one onto a microlaser randomly. Red lines represent mean values of the measured beat frequencies for each binding event. (c) Histograms of the beat frequency changes for two particle sizes. Black solid curves are Gaussian fittings. The total numbers of detected binding events are 397 for R_1 and 419 for R_2 . The mean and standard deviation of the histograms are presented in the plot with unit MHz. (d) Weighted standard deviation μ of splitting changes versus threshold δ for R_1 (red circles) and R_2 (blue stars). Inset: The same curves are plotted after multiplying the x-axis of the curve for R_2 with a correction term $\delta_1/\delta_2 = 0.22$, which is close to the ratio $(R_1/R_2)^3 = 0.23$.

Since the two histograms in Figure 7.14(c) have the same type of distribution, the above issue can be solved by calculating the relative standard deviations. We select a threshold δ , and define ΔS_δ as the standard deviation of the measured steps that are greater than δ . Thus we obtain ΔS_δ as a function of δ . Based on the calculated ΔS_{δ_1} and ΔS_{δ_2} for $R_1 = 15$ nm and $R_2 = 25$ nm particles, we define two dimensionless parameters (weighted standard deviation) $\mu_1 = \Delta S_{\delta_1} / \delta$ and $\mu_2 = \Delta S_{\delta_2} / \delta$, and plot them as a function of δ in Figure 7.14(d). Denoting the threshold which leads to $\mu_1 = \mu_2$ for the two ensembles as

δ_1 and δ_2 , it is easy to obtain the relation $(\delta_1/\delta_2) \propto (R_1/R_2)^3$. Therefore, from the ratio δ_1/δ_2 , we can get the size relation between R_1 and R_2 . Using the ratio δ_1/δ_2 as a correction term (i.e., scale the x-axis of the curve for R_2 with δ_1/δ_2), we replot the μ versus δ curves for two ensembles and depict them in the inset of Figure 7.14(d). There is a good overlap between the two curves after correction.

This analysis suggests that we can calibrate the detection system using the measurement results for reference particles with known refractive index and known size, say R_2 , to estimate the unknown size R_1 of particles with the same refractive index. The same procedure yields a relation between the polarizabilities α of the reference and the unknown ensembles as $(\delta_1/\delta_2) \propto (\alpha_1/\alpha_2)$.

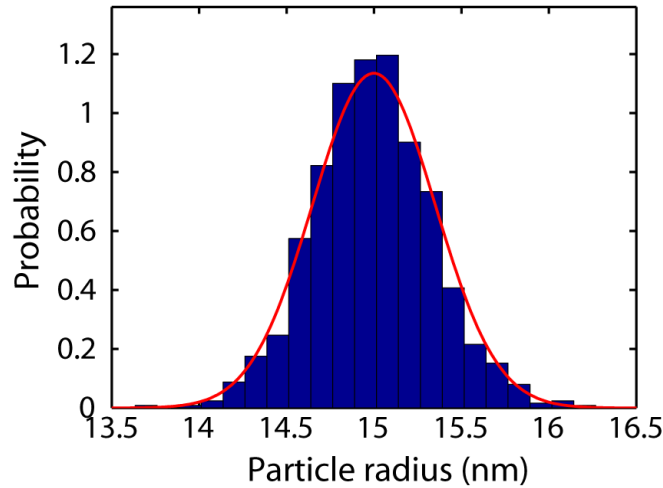


Figure 7.15 Distribution of size estimation using bootstrap method of 1000 resamples. Red curve is a Gaussian fitting with mean value of 14.97 nm.

The approach described above provides a single estimation of the particle size which does not show how accurate it is as an estimate of the true value. To determine the accuracy of the size estimation, we use the bootstrap method to obtain the confidence interval of the estimate [148-149]. Bootstrap approach is to construct a number of resamples from the original measured dataset. Each of the resamples is obtained from random sampling and replacement of the original data points, and has the same length with the original dataset. For each resample, we compute and obtain one particle size

estimation. This resampling process is repeated 1000 times and we are then in possession of a collection of 1000 size estimations. Distribution of these estimations approximates the distribution of the actual particle size. The confidence interval can thus be obtained by using the appropriate upper and lower percentages of the distribution. Using the measured data in Figure 7.14, we obtain the distribution of the size for $R_1 = 15$ nm particles in Figure 7.15 when taking $R_2 = 25$ nm particles as reference.

In the measurements, one can reduce the estimation error by increasing the number of detected particles. Here we use the measured data in Figure 7.14 to verify this statement. To study the effect of detected particle number on size estimation, we take the first N ($N=1\dots397$) data points from the measured results for 15-nm and 25-nm particle groups to estimate the size of 15-nm particles. The estimation results as a function of N are plotted in Figure 7.16. Obviously, the confidence interval decreases with increasing particle number, suggesting a higher accuracy. For particle number of 250, the size estimation is 14.92 nm with confidence interval (13.94 nm, 15.94 nm) which is close to the data provided by the manufacture (mean 15.15 nm, coefficient of variance $<8\%$).

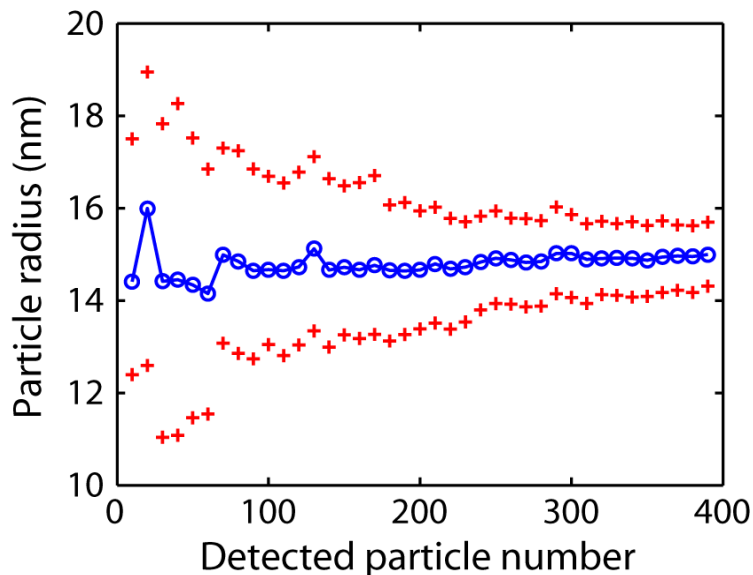


Figure 7.16 Size estimation of Au nanoparticles as a function of detected particle number for reference and measured particles. Blue circles and red crosses are the mean and 95% confidence interval of the size estimation obtained from the bootstrap method of 1000 resampling.

In this section, we have investigated the particle size estimation through ensemble measurements. Due to the uncontrollable particle positions on the resonator, with each particle binding event, the frequency splitting may increase or decrease with random step heights. Collection of changes in the frequency splitting carries information of the particle polarizability and can be used to extract the particle size. The accuracy of the size estimation can be enhanced by increasing the detected particle number. The proposed method for size estimation can also be applied in the resonance shift based detection scheme, in which frequency shift is the sensing signal.

7.4 Detection using Multiple-Wavelength Microlasers

To demonstrate the multi-wavelength detection capability of the proposed scheme, we used a microtoroid laser supporting two lasing modes as seen in Figure 7.17(a). The same pump source was utilized to excite the two lasing modes. In this case, the attached particles interact with both lasing modes. Since particle induced frequency splitting in a WGM is determined by the spatial overlap of the mode with the nanoparticle, each lasing mode produces its own heterodyne beat note. The detected signal from the photodetector becomes a mixture of these beat notes which are revealed by two frequency peaks in the FFT spectrum in Figure 7.17(b).

Figure 7.17(c) depicts the evolution of the two beat frequencies as gold nanoparticles are continuously deposited onto the microlaser surface. From the intensity graph, the magnitudes of beat frequencies for the two lasing modes are different, enabling us to discriminate and track the two beat notes separately. For each binding event, the two lasing modes experience different splitting changes. This can be exploited to decrease the false-negative results (e.g., a particle is adsorbed onto the surface but is not detected) as shown in Figure 7.17(d). Thus, using multiple-wavelength microlasers helps reduce the detection errors induced by the particle position dependence of the frequency

splitting. These results show that the microlaser provides a compact platform to realize simultaneous multi-wavelength detection of nanoscale objects.

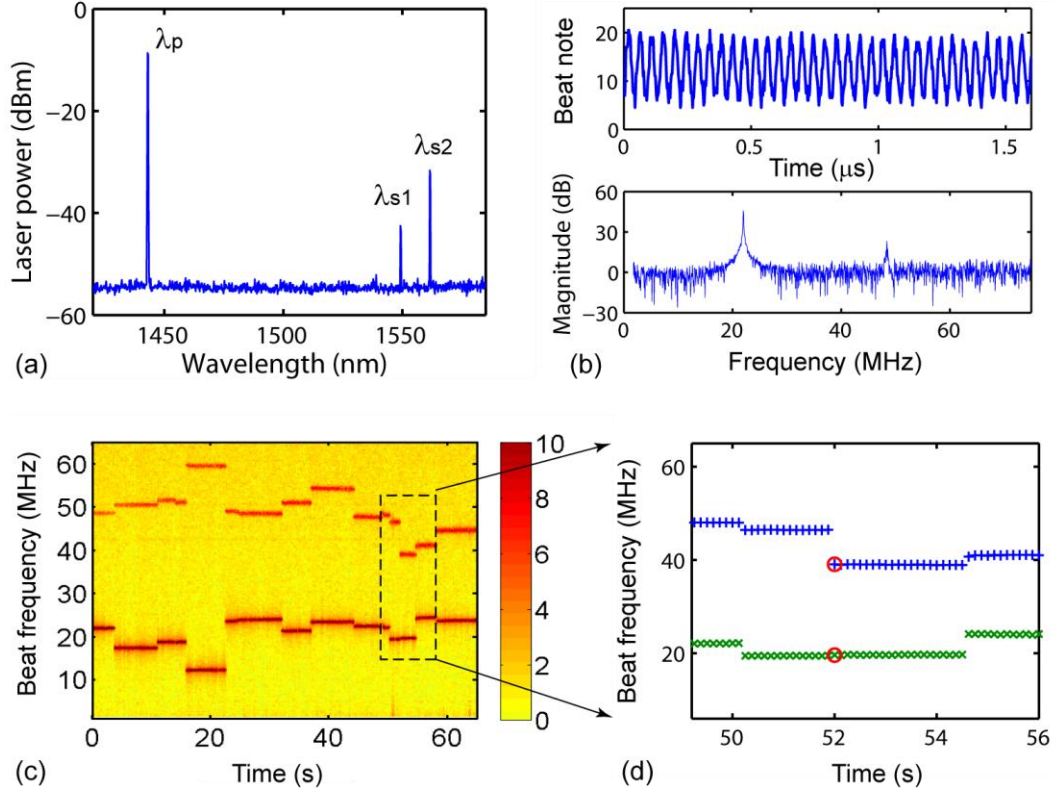


Figure 7.17 Simultaneous multi-wavelength detection of nanoparticles using a single microlaser. (a) Typical spectrum of a two-mode microrotoroid laser. The pump is located at $\lambda_p = 1443$ nm, and the two lasing lines are at $\lambda_{s1} = 1549$ nm and $\lambda_{s2} = 1562$ nm. (b) A typical beat note signal and its FFT spectrum for the two-mode microlaser. The two peaks in the FFT spectrum correspond to frequency splitting of the lasing modes at λ_{s1} and λ_{s2} , separately. (c) Intensity graph of the FFT spectrum when Au particles of $R = 50$ nm are continuously deposited onto the microlaser surface.

The side bar denotes magnitude of the FFT spectrum in dB. For the same particle binding events, the heights of discrete changes in the two beat frequencies are different. (d) Close-up of the black rectangle in (c). Red circles mark the particle binding event that is clearly detected by one laser mode, but undetected by the other mode.

7.5 Maximum Detectable Particle Number

For the microlaser-based particle detection scheme, the maximum detectable particle number using a single microcavity laser is mainly limited by two factors: (i) The bandwidth of the photodetector. This sets the maximum detectable frequency splitting of the lasing mode. (ii) Loss induced by the attached particles. This loss contributes to

the total cavity losses experienced by photons. As more particles bind on the microlaser, the total cavity losses increase leading to broadening of the laser linewidth. The frequency splitting will go undetected when it is smaller than the laser linewidth. On the other hand, when the total cavity losses are greater than the optical gain provided by the active medium, laser emission cannot be generated. In both cases, the attached particles can no longer be detected.

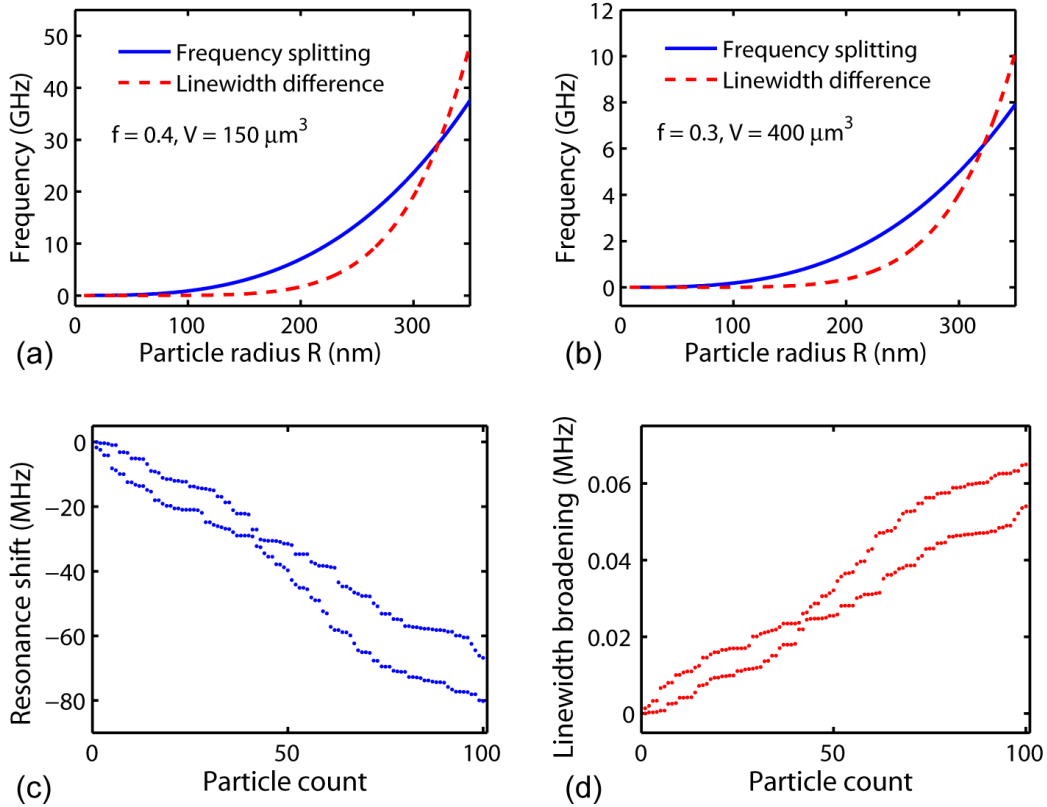


Figure 7.18 Calculation results of the frequency splitting $2g$ (a) and linewidth difference 2Γ (b) induced by a single PS nanoparticle as a function of the particle radius for different WGM parameters: mode volume V and field function f . Simulation results of the resonance frequency shift (c) and linewidth broadening (d) of the two split modes as PS particles of radius 30 nm are consecutively deposited on the resonator randomly. Parameters used in the calculations of (c) and (d) are: maximum field $f = 0.3$, $V = 400 \mu\text{m}^3$, and $\lambda_c = 1550 \text{ nm}$.

We performed numerical simulations to study the dependence of particle induced frequency splitting $2g$ and linewidth broadening 2Γ on the particle size. As seen in Figure 7.18, small particles affect $2g$ more than 2Γ . This can be explained by the R^3 and R^6 dependences of $2g$ and 2Γ on the particle radius R , respectively. Figure 7.18(c) and (d)

show the resonance frequency shift and linewidth broadening of the two split modes as PS particles are deposited consecutively and randomly onto the resonator surface. The red shift in resonance frequency is attributed to the larger refractive index of PS particles than that of air. It is seen that the linewidth broadening of the split modes induced by 30-nm PS particles is much smaller than the induced frequency splitting.

In our experiments, the measured particles are a few tens of nanometers. Therefore, a large number of particles can be detected using a single microlaser without significantly degrading the lasing linewidth. In the experiments, we detected and counted up to 816 Au nanoparticles using a single microlaser.

7.6 Sensitivity and Detection Limit

To enhance the particle detection sensitivity and improve the detection limit, a large frequency splitting $2g$ is preferred. From the expression $2g = -\alpha f^2(\mathbf{r})\omega_c/V$, frequency splitting strongly depends on the field distribution f and the mode volume V , both of which are cavity-related parameters. The greater the f^2/V , the larger the frequency splitting, and hence the higher the detection sensitivity. This is confirmed with the numerical simulation results in Figure 7.19.

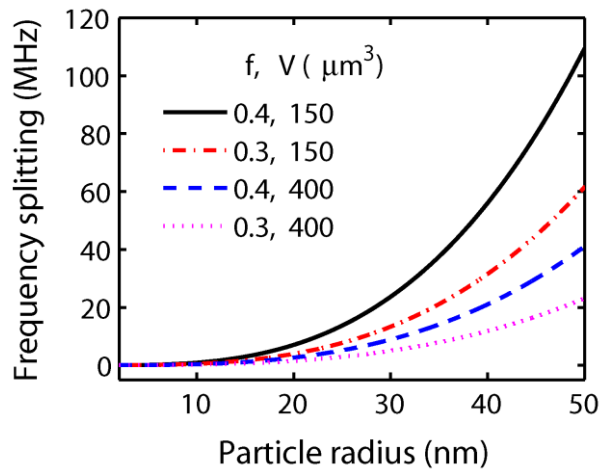


Figure 7.19 Dependence of a single PS nanoparticle induced frequency splitting $2g$ on the particle radius R for various values of normalized field maximum f and mode volume V . Simulations are performed at $\lambda_c = 1550$ nm.

The detection limit depends on both the sensitivity and the minimum detectable change in frequency splitting. The ultimate limit of the latter one is the microlaser linewidth. When particle induced frequency splitting is smaller than the laser linewidth, the splitting cannot be distinguished and the particle will go undetected. However, in practical measurement, the detection limit is determined by the fluctuations of the microlaser beat frequency which is much larger than the laser linewidth. Detailed effects of the cavity size and the beat frequency fluctuations are discussed in this section.

7.6.1 Effects of the Resonator Size on the Detection Sensitivity

Since f and V are functions of physical dimensions of the microcavity, we perform simulations with COMSOL to characterize WGM distributions in a silica microtoroidal resonator and to understand the dependence of f and V on its major and minor diameters.

Field function f is position dependent and its value varies with the radial and polar positions. In Figure 7.20, for simplicity, we consider the maximum field on the outer boundary of the resonator. Figure 7.20(b) and (c) reveal that when the minor diameter is fixed, f is smaller and V is larger for the microtoroid with a larger major diameter, i.e., f decreases whereas V increases with increasing major diameter. On the other hand, for a fixed major diameter, both f and V increase with increasing minor diameter. This can be understood as follows. For a smaller cavity, the spatial confinement is stronger and the optical mode is more compressed in the resonator leading to a smaller mode volume. At the same time, the evanescent field leaking into the surrounding medium is larger resulting in a higher field function f on the resonator surface. Defining $f^2\omega_c/V$ as the splitting coefficient and plotting it as a function of the major diameter in Figure 7.20(d), we see that splitting coefficient decreases with the increasing major diameter of the microtoroid, while the effect of the minor diameter is very small, if not negligible. These

results imply that smaller microtoroids have better sensitivity for nanoparticle detection than bigger ones.

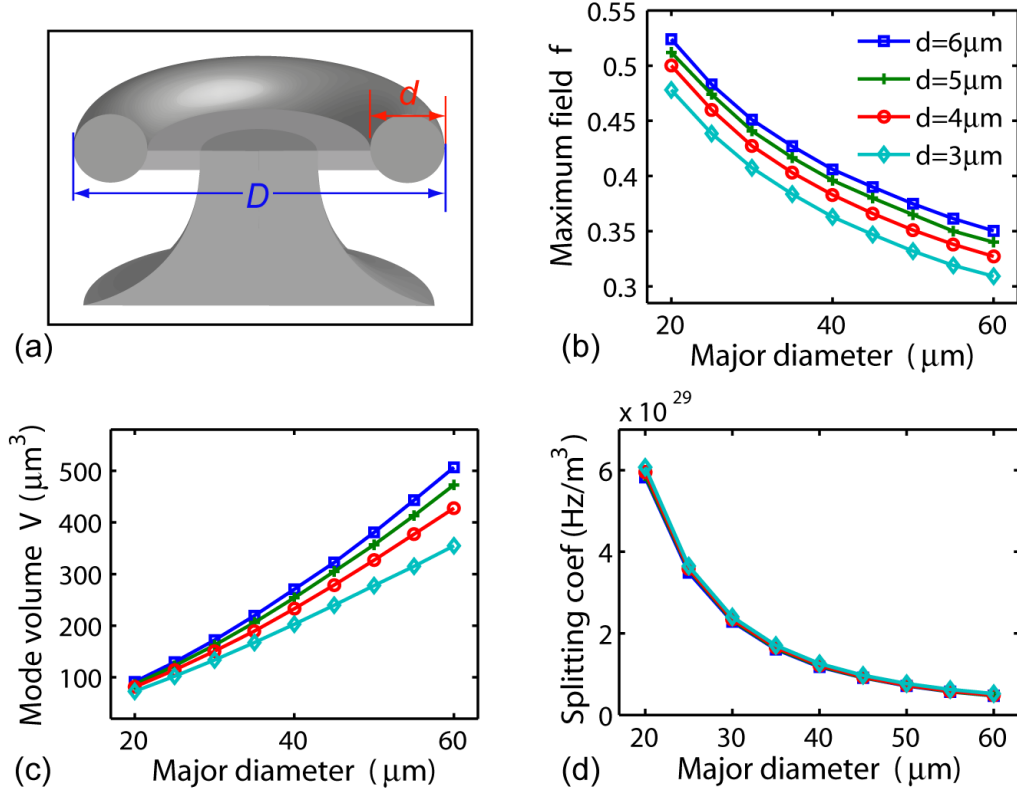


Figure 7.20 (a) Illustration showing the major (D) and minor (d) diameters of a microtoroid. Simulation results of the maximum field f (b), mode volume V (c), and splitting coefficient (d) as a function of D for $d = 6, 5, 4,$ and $3 \mu\text{m}$. The plots are for TE-polarized fundamental WGM. Splitting coefficient in (d) is defined as $f^2 \omega_c / V$ for $\lambda_c = 1550 \text{ nm}$. The data legends in (c) and (d) are the same as those in (b).

To further understand the results in Figure 7.20, we perform simulations to study the field distributions in microtoroids of different sizes. In Figure 7.21, we present two-dimensional mode distributions in the cross section area of the ring for the microtoroid, together with the one-dimensional mode distributions along the polar and radial directions of the ring labeled with red dotted lines in Figure 7.21(a). In a microtoroidal resonator, the WGM is confined near the surface of the ring. The effects of physical dimensions of the microtoroid on the WGM confinement as well as the field distributions are clearly observed in Figure 7.21.

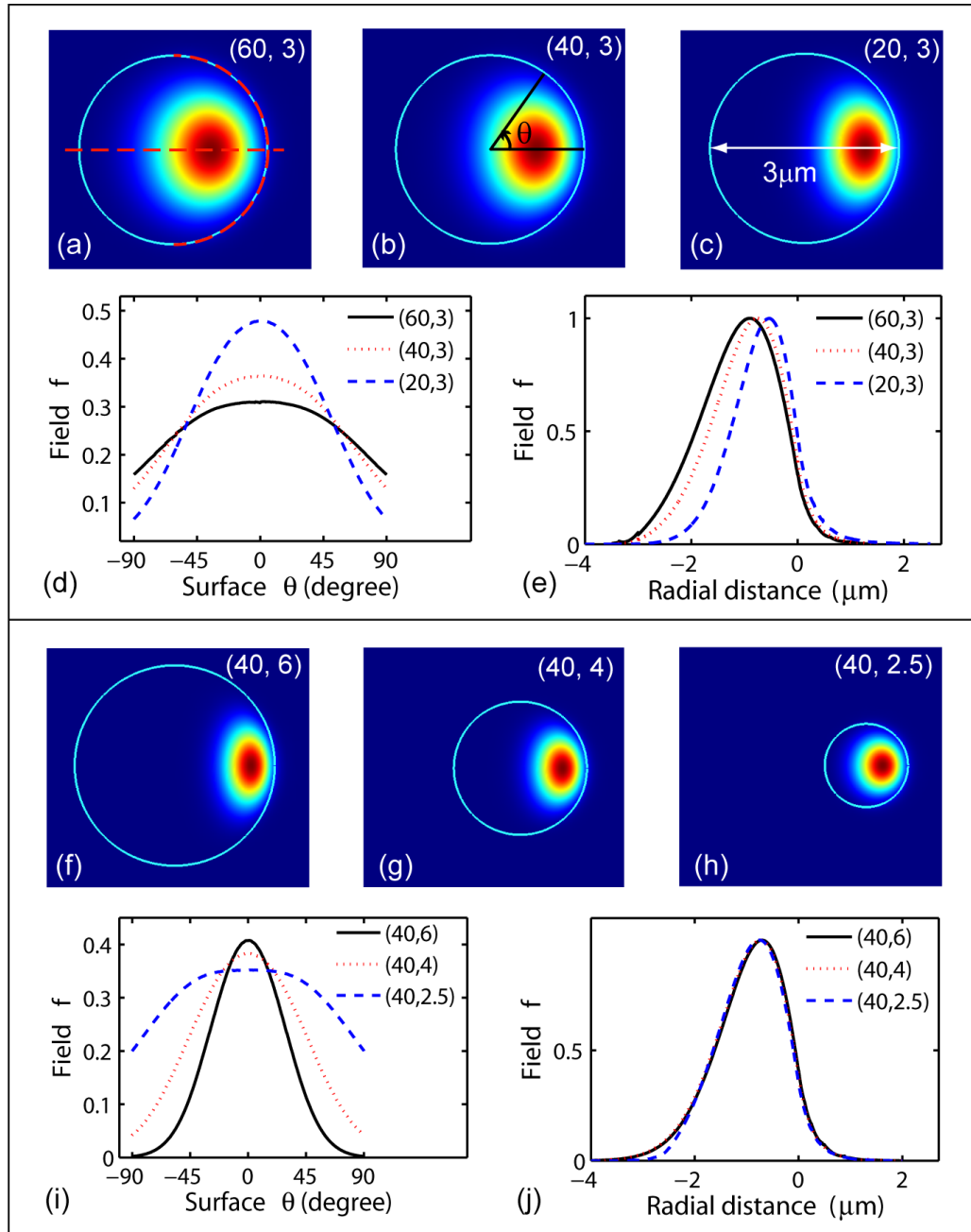


Figure 7.21 Field distributions of TE-polarized fundamental resonant modes in microtoroids of different major and minor diameters. Size of the microtoroid is denoted in a pair of parentheses as (major diameter, minor diameter) with unit of micrometer. (a)-(e) depict the results for different major diameters and the same minor diameter. (f)-(j) show the distributions for the same major diameter and different minor diameters. (a)-(c) and (f)-(h) present the cross-sectional field distributions. (d) and (i) present the normalized field distribution along the outer boundary of the microtoroid. (e) and (j) show the normalized field distribution along the radial direction as marked by the red dotted line in the horizontal direction in (a). In (e) and (j), the point $x = 0$ represents the boundary of the microtoroid.

We performed experiments by depositing PS nanoparticles of radius $R = 50$ nm one by one on two Er-doped toroidal microlasers with different diameters. The histograms of discrete changes in the beat frequency are presented in Figure 7.22. It shows that the standard deviation of the histogram is larger for the smaller microlaser, implying that a smaller cavity is more likely to lead to a larger change in the frequency splitting for the same perturbation, and thus has better detection sensitivity.

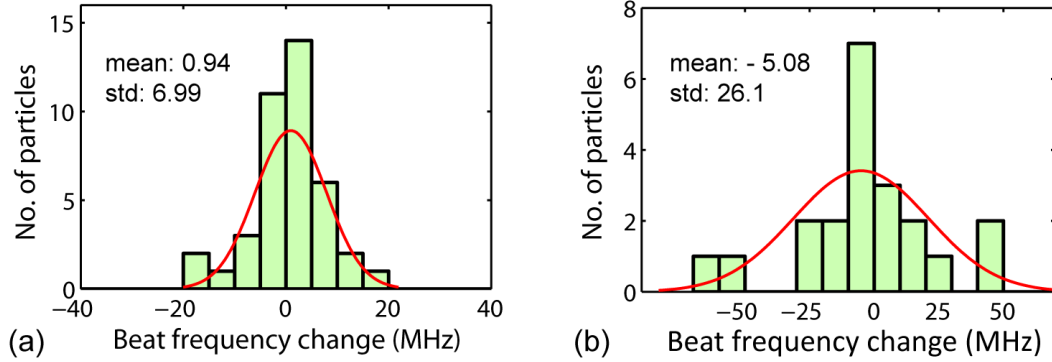


Figure 7.22 Histograms of measured discrete changes in the laser beat frequency as PS nanoparticles of $R = 50$ nm are deposited on Er-doped microroids of diameters $42 \mu\text{m}$ (a) and $30 \mu\text{m}$ (b). The total number of detected particles is 40 in (a) and 21 in (b). Red solid lines are Gaussian fittings. Mean and standard deviation of the histograms are shown in each plot with unit MHz.

7.6.2 Theoretical Detection Limit

The ultimate limit of single nanoparticle detection using mode splitting in a microlaser is determined by the laser linewidth. The fundamental linewidth of a laser $\Delta\nu_{\text{laser}}$, if technical noise is ignored, is given by the Schawlow-Townes formula as [150]

$$\Delta\nu_{\text{laser}} = \frac{\pi h\nu(\Delta\nu)^2}{P_{\text{out}}} \quad (7.67)$$

where $h\nu$ is the photon energy with h representing the Planck's constant and ν denoting the cavity resonance frequency, $\Delta\nu$ is the cold cavity resonance linewidth (i.e., when the gain medium is not excited) that is related to the cold cavity Q through $\Delta\nu = \nu/Q$, and P_{out} is the laser output power. For the Er-doped microroids in our experiments, the cold cavity Q is in the range of $10^6 \sim 10^7$, and the lasing wavelength is

$\lambda = 1550$ nm with the output laser power $P_{\text{out}} = 10$ μW . Then the laser linewidth estimated from Eq. (7.67) is in the range of 15 Hz~1.5 kHz, which is much narrower than that of a passive resonator. Numerical simulation results in Figure 7.23 show the frequency splitting as a function of the PS particle radius. By comparing these results with the laser linewidth, we obtain that the ultimate detection limit using the microlaser based detection scheme varies from less than 1 nm to a few nm.

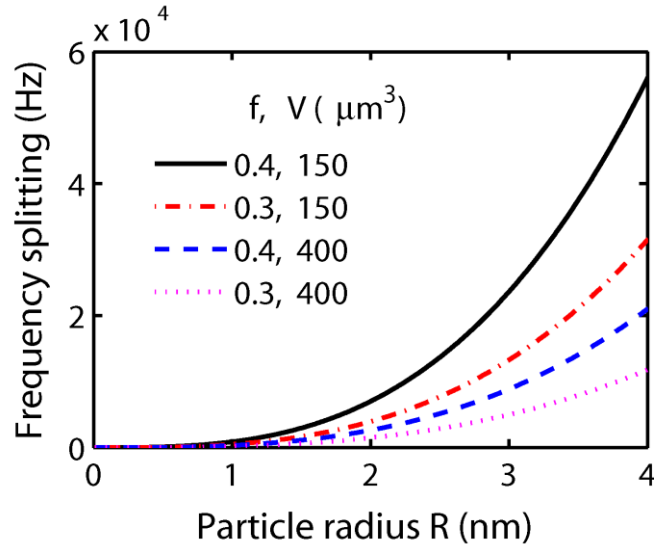


Figure 7.23 Simulation results of a single PS nanoparticle induced frequency splitting as a function of the particle radius R for different f and V at $\lambda_c = 1550$ nm.

7.6.3 Noise Level

In our experiments, the smallest detectable particle size is determined by the fluctuation noise of the laser beat frequency. In order to quantify this noise, we record the beat frequency without introducing any nanoparticles.

Beat Frequency Noise in Air

Figure 7.24(a) shows the detected beat frequency change in air with time. The noise level ± 100 kHz does not change with the number of attached particles. Particle adsorption induced splitting change within this noise level cannot be detected. The beat frequency has a Gaussian distribution as seen from the histogram in Figure 7.24(b). The

noise might be attributed to various factors including (i) pump laser fluctuations, (ii) taper-cavity gap fluctuations, (iii) noise from the photodetector, (iv) data processing noise, and (v) contaminants or Er^{3+} ion clusters inside the microlaser whose polarizabilities fluctuate due to the intracavity thermal fluctuations.

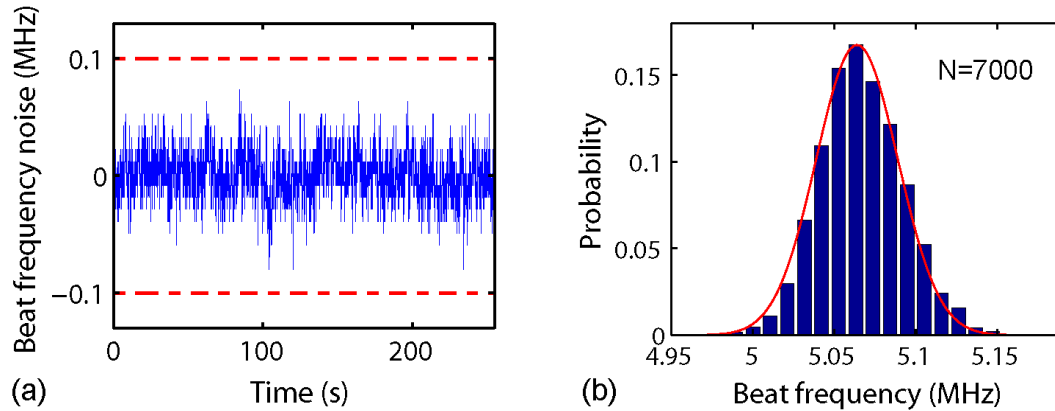


Figure 7.24 (a) Beat frequency fluctuation in air: noise is within ± 100 kHz. This noise level sets the limit for the smallest detectable particle size in our experiments. (b) Histogram showing the beat frequency distribution. The histogram is constructed from a total of 7000 measurement points. Red solid line is a Gaussian fitting with mean 5.06 MHz and standard deviation 25 kHz.

Based on this noise level, the minimum particle size we can detect is 10-nm radius for Au particles and 15-nm radius for PS particles (Figure 7.5). This detection limit was achieved in an operating environment with no stabilization or external reference, and could be further improved by better control and characterization of the spectral properties of the pump laser, by operating the microlaser in a more stable environment, and by employing a better data acquisition system.

Beat Frequency Noise in Water

We measured the fluctuations of the beat frequency from an Yb-doped microtoroid laser when the microlaser and the fiber taper were immersed in a water chamber. The results are shown in Figure 7.25. The noise level is 4 MHz which is much higher than that in air. This is attributed to the flow property of water that forms an unstable cavity surrounding.

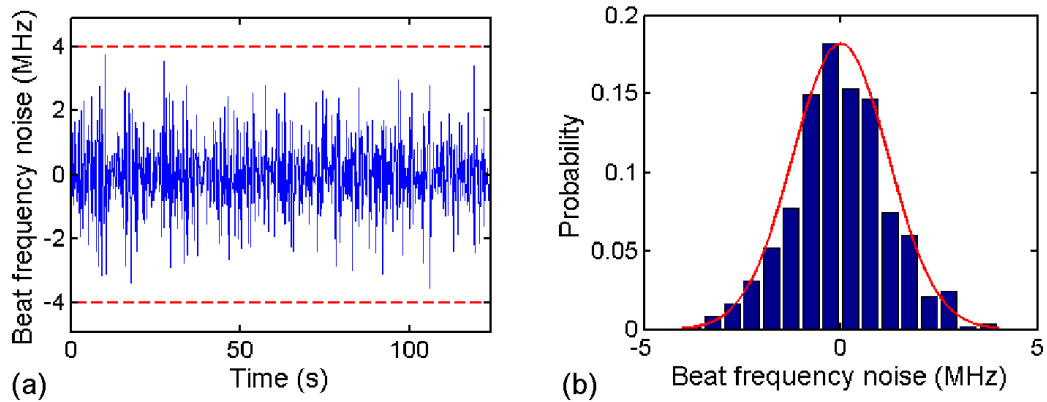


Figure 7.25 (a) Beat frequency fluctuation in water: noise is within ± 4 MHz. (b) Histogram showing the distribution of the beat frequency noise. The histogram is constructed from a total of 621 measurement points. Red solid line is a Gaussian fitting with mean 5.3 kHz and standard deviation 1.2 MHz.

The fluctuations of beat frequency in water vary with the attached particles due to the possible Brownian motion of particles surrounding the microlaser. Depending on the distance of the particle movement around the microlaser, interaction of the particle with the evanescent field varies, leading to different beat frequency fluctuations. This is clearly observed in Figure 7.26. At time 38s, a sudden change occurred and the beat frequency varied between 10 MHz and 60 MHz indicating a strong particle movement. The Brownian motion of particles in the evanescent field of the resonator is beyond the scope of this dissertation and will not be discussed here.

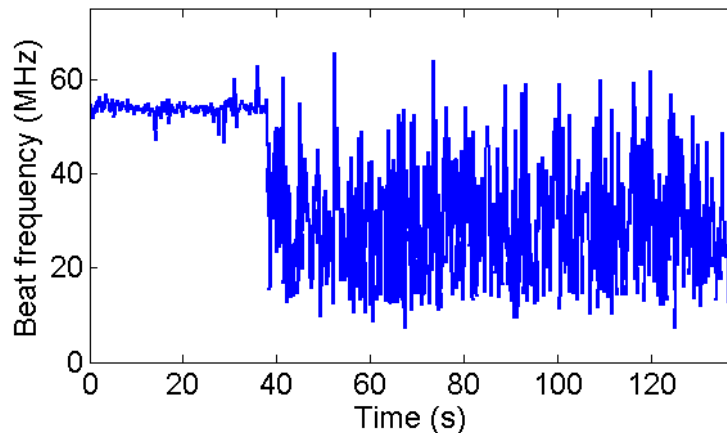


Figure 7.26 Recorded beat frequency with time when PS particles of $R = 100$ nm are injected into the water chamber.

7.7 Conclusions and Outlook

Using frequency splitting in a WGM microlaser, we significantly improved the label-free nanoparticle detection limit without increasing the system complexity. The lower detection limit stems from the ultra-narrow laser linewidth and the self-referencing nature of mode splitting. Hertz level laser linewidths in Er-doped microcavities suggest that lower detection limit less than 1 nm is within reach. In addition to its superior lower detection limit, a microlaser based detection scheme also eliminates the need for a narrow linewidth tunable laser to detect the induced spectral shift or mode splitting. Thus, tunable laser related issues such as slow response time, thermal effects, and tuning noises (e.g., piezo-motion) are avoided.

The proposed scheme could be further improved to allow single-shot size measurement by monitoring changes in both frequencies and linewidths of the split lasing modes. This may be done by employing linewidth measurement techniques [151]. The ultra-low threshold and narrow linewidth microlasers can be integrated with on-chip laser diodes as pump sources enabling a compact measurement platform. Moreover, microlasers with multiple-wavelength emission can be configured to classify nanoparticles. Although we report experiments using microtoroidal cavity lasers, the techniques developed here can be used in many other nano- and micro- lasers, such as photonic crystal cavities and WGM microlasers using microspheres, microrings, etc.

Localized plasmon effect in WGM resonators can further improve the detection resolution by local enhancement of light field which will enhance the light-matter interactions. This has been demonstrated in passive resonators [152-153]. By functionalizing the resonator surface with metal nanoparticles (e.g., gold, silver), resonance shift induced by single particle binding event at a plasmonic hot spot was significantly enhanced. Such effect can be applied to microlasers. The developments of WGM-plasmon hybrid resonators pave the way for label-free detection on single molecule and protein level.

References

- [1] N. Hodgson and H. Weber, *Laser resonators and beam propagation : fundamentals, advanced concepts and applications*. Springer, New York, 2nd edn (2005).
- [2] A. E. Siegman, "Laser beams and resonators: The 1960s," *Ieee J Sel Top Quant* **6**, 1380-1388 (2000).
- [3] A. E. Siegman, "Laser beams and resonators: Beyond the 1960s," *Ieee J Sel Top Quant* **6**, 1389-1399 (2000).
- [4] K. Vahala, *Optical microcavities*. World Scientific, Singapore ; Hackensack, N.J., (2004).
- [5] A. B. Matsko and V. S. Ilchenko, "Optical resonators with whispering-gallery modes - Part I: Basics," *Ieee J Sel Top Quant* **12**, 3-14 (2006).
- [6] V. S. Ilchenko and A. B. Matsko, "Optical resonators with whispering-gallery modes - Part II: Applications," *Ieee J Sel Top Quant* **12**, 15-32 (2006).
- [7] A. Chiasera, Y. Dumeige, P. Feron, M. Ferrari, Y. Jestin, G. N. Conti, S. Pelli, S. Soria and G. C. Righini, "Spherical whispering-gallery-mode microresonators," *Laser Photonics Rev* **4**, 457-482 (2010).
- [8] J. Ward and O. Benson, "WGM microresonators: sensing, lasing and fundamental optics with microspheres," *Laser Photonics Rev* **5**, 553-570 (2011).
- [9] P. Rabiei, W. H. Steier, C. Zhang and L. R. Dalton, "Polymer micro-ring filters and modulators," *J Lightwave Technol* **20**, 1968-1975 (2002).
- [10] H. C. Tapalian, J. P. Laine and P. A. Lane, "Thermo-optical switches using coated microsphere resonators," *Ieee Photonic Tech L* **14**, 1118-1120 (2002).
- [11] Q. Xu and M. Lipson, "All-optical logic based on silicon micro-ring resonators," *Opt Express* **15**, 924-929 (2007).
- [12] L. Yang, T. Carmon, B. Min, S. M. Spillane and K. J. Vahala, "Erbium-doped and Raman microlasers on a silicon chip fabricated by the sol-gel process," *Appl Phys Lett* **86**, 091114 (2005).

- [13] L. He, S. K. Ozdemir, J. Zhu, W. Kim and L. Yang, "Detecting single viruses and nanoparticles using whispering gallery microlasers," *Nature Nanotech* **6**, 428-432 (2011).
- [14] J. Zhu, S. K. Ozdemir, Y. F. Xiao, L. Li, L. He, D. R. Chen and L. Yang, "On-chip single nanoparticle detection and sizing by mode splitting in an ultrahigh-Q microresonator," *Nature Photon* **4**, 46-49 (2010).
- [15] J. P. Reithmaier *et al.*, "Strong coupling in a single quantum dot-semiconductor microcavity system," *Nature* **432**, 197-200 (2004).
- [16] L. Rayleigh, "The problem of the whispering gallery," *Phil. Mag.* **20**, 1001-1004 (1910).
- [17] C. G. B. Garrett, W. Kaiser and W. L. Bond, "Stimulated emission into optical whispering modes of spheres," *Phys Rev* **124**, 1807-1809 (1961).
- [18] K. J. Vahala, "Optical microcavities," *Nature* **424**, 839-846 (2003).
- [19] A. Ashkin and J. M. Dziedzic, "Observation of resonances in the radiation pressure on dielectric spheres," *Phys Rev Lett* **38**, 1351-1354 (1977).
- [20] A. Kiraz, A. Kurt, M. A. Dundar and A. L. Demirel, "Simple largely tunable optical microcavity," *Appl Phys Lett* **89**, 081118 (2006).
- [21] V. B. Braginsky, M. L. Gorodetsky and V. S. Ilchenko, "Quality-factor and nonlinear properties of optical whispering-gallery modes," *Phys Lett A* **137**, 393-397 (1989).
- [22] M. Borselli, K. Srinivasan, P. E. Barclay and O. Painter, "Rayleigh scattering, mode coupling, and optical loss in silicon microdisks," *Appl Phys Lett* **85**, 3693-3695 (2004).
- [23] C. Y. Chao and L. J. Guo, "Polymer microring resonators fabricated by nanoimprint technique," *J Vac Sci Technol B* **20**, 2862-2866 (2002).
- [24] I. S. Grudinin, A. B. Matsko, A. A. Savchenkov, D. Strekalov, V. S. Ilchenko and L. Maleki, "Ultra high Q crystalline microcavities," *Opt Commun* **265**, 33-38 (2006).
- [25] M. L. Gorodetsky, A. A. Savchenkov and V. S. Ilchenko, "Ultimate Q of optical microsphere resonators," *Opt Lett* **21**, 453-455 (1996).
- [26] M. Soltani, S. Yegnanarayanan and A. Adibi, "Ultra-high Q planar silicon microdisk resonators for chip-scale silicon photonics," *Opt Express* **15**, 4694-4704 (2007).

- [27] D. K. Armani, T. J. Kippenberg, S. M. Spillane and K. J. Vahala, "Ultra-high-Q toroid microcavity on a chip," *Nature* **421**, 925-928 (2003).
- [28] T. A. Birks, J. C. Knight and T. E. Dimmick, "High-resolution measurement of the fiber diameter variations using whispering gallery modes and no optical alignment," *Ieee Photonic Tech L* **12**, 182-183 (2000).
- [29] I. M. White, H. Oveys and X. D. Fan, "Liquid-core optical ring-resonator sensors," *Opt Lett* **31**, 1319-1321 (2006).
- [30] G. S. Murugan, J. S. Wilkinson and M. N. Zervas, "Optical excitation and probing of whispering gallery modes in bottle microresonators: potential for all-fiber add-drop filters," *Opt Lett* **35**, 1893-1895 (2010).
- [31] M. Pollinger, D. O'Shea, F. Warken and A. Rauschenbeutel, "Ultrahigh-Q tunable whispering-gallery-mode microresonator," *Phys Rev Lett* **103**, 053901 (2009).
- [32] B. E. Little *et al.*, "Very high-order microring resonator filters for WDM applications," *Ieee Photonic Tech L* **16**, 2263-2265 (2004).
- [33] S. Berneschi, D. Farnesi, F. Cosi, G. N. Conti, S. Pelli, G. C. Righini and S. Soria, "High Q silica microbubble resonators fabricated by arc discharge," *Opt Lett* **36**, 3521-3523 (2011).
- [34] C. Junge, S. Nickel, D. O'Shea and A. Rauschenbeutel, "Bottle microresonator with actively stabilized evanescent coupling," *Opt Lett* **36**, 3488-3490 (2011).
- [35] A. L. Martin, D. K. Armani, L. Yang and K. J. Vahala, "Replica-molded high-Q polymer microresonators," *Opt Lett* **29**, 533-535 (2004).
- [36] T. Grossmann, S. Schleede, M. Hauser, T. Beck, M. Thiel, G. von Freymann, T. Mappes and H. Kalt, "Direct laser writing for active and passive high-Q polymer microdisks on silicon," *Opt Express* **19**, 11451-11456 (2011).
- [37] J. R. Schwesyg, T. Beckmann, A. S. Zimmermann, K. Buse and D. Haertle, "Fabrication and characterization of whispering-gallery-mode resonators made of polymers," *Opt Express* **17**, 2573-2578 (2009).
- [38] C.-H. Dong, L. He, Y.-F. Xiao, V. R. Gaddam, S. K. Ozdemir, Z.-F. Han, G.-C. Guo and L. Yang, "Fabrication of high-Q polydimethylsiloxane optical microspheres for thermal sensing," *Appl Phys Lett* **94**, 231119 (2009).

- [39] M. L. Gorodetsky and V. S. Ilchenko, "Optical microsphere resonators: optimal coupling to high-Q whispering-gallery modes," *J Opt Soc Am B* **16**, 147-154 (1999).
- [40] J. C. Knight, G. Cheung, F. Jacques and T. A. Birks, "Phase-matched excitation of whispering-gallery-mode resonances by a fiber taper," *Opt Lett* **22**, 1129-1131 (1997).
- [41] M. L. Gorodetsky and V. S. Ilchenko, "High-Q Optical Whispering-Gallery Microresonators - Precession Approach for Spherical Mode Analysis and Emission Patterns with Prism Couplers," *Opt Commun* **113**, 133-143 (1994).
- [42] M. K. Chin and S. T. Ho, "Design and modeling of waveguide-coupled single-mode microring resonators," *J Lightwave Technol* **16**, 1433-1446 (1998).
- [43] B. E. Little, J. P. Laine and H. A. Haus, "Analytic theory of coupling from tapered fibers and half-blocks into microsphere resonators," *J Lightwave Technol* **17**, 704-715 (1999).
- [44] V. S. Ilchenko, X. S. Yao and L. Maleki, "Pigtailling the high-Q microsphere cavity: a simple fiber coupler for optical whispering-gallery modes," *Opt Lett* **24**, 723-725 (1999).
- [45] M. Cai, O. Painter and K. J. Vahala, "Observation of critical coupling in a fiber taper to a silica-microsphere whispering-gallery mode system," *Phys Rev Lett* **85**, 74-77 (2000).
- [46] M. L. Gorodetsky, A. D. Pryamikov and V. S. Ilchenko, "Rayleigh scattering in high-Q microspheres," *J Opt Soc Am B* **17**, 1051-1057 (2000).
- [47] S. M. Spillane, T. J. Kippenberg, K. J. Vahala, K. W. Goh, E. Wilcut and H. J. Kimble, "Ultrahigh-Q toroidal microresonators for cavity quantum electrodynamics," *Phys Rev A* **71**, 013817 (2005).
- [48] K. Srinivasan, M. Borselli and O. Painter, "Cavity Q, mode volume, and lasing threshold in small diameter AlGaAs microdisks with embedded quantum dots," *Opt Express* **14**, 1094-1105 (2006).
- [49] H. A. Haus, *Waves and fields in optoelectronics*. Prentice-Hall, Englewood Cliffs, NJ, (1984).
- [50] A. M. Armani, A. Srinivasan and K. J. Vahala, "Soft lithographic fabrication of high Q polymer microcavity arrays," *Nano Lett* **7**, 1823-1826 (2007).

- [51] T. Grossmann, M. Hauser, T. Beck, C. Gohn-Kreuz, M. Karl, H. Kalt, C. Vannahme and T. Mappes, "High-Q conical polymeric microcavities," *Appl Phys Lett* **96**, 013303 (2010).
- [52] H. S. Choi, X. M. Zhang and A. M. Armani, "Hybrid silica-polymer ultra-high-Q microresonators," *Opt Lett* **35**, 459-461 (2010).
- [53] J. R. Anderson, D. T. Chiu, R. J. Jackman, O. Cherniavskaya, J. C. McDonald, H. K. Wu, S. H. Whitesides and G. M. Whitesides, "Fabrication of topologically complex three-dimensional microfluidic systems in PDMS by rapid prototyping," *Analytical Chemistry* **72**, 3158-3164 (2000).
- [54] D. Erickson and D. Q. Li, "Integrated microfluidic devices," *Analytica Chimica Acta* **507**, 11-26 (2004).
- [55] C. Monat, P. Domachuk and B. J. Eggleton, "Integrated optofluidics: A new river of light," *Nature Photon* **1**, 106-114 (2007).
- [56] L. He, Y.-F. Xiao, C.-H. Dong, J. Zhu, V. Gaddam and L. Yang, "Compensation of thermal refraction effect in high-Q toroidal microresonator by polydimethylsiloxane coating," *Appl Phys Lett* **93**, 201102 (2008).
- [57] L. He, Y.-F. Xiao, J. Zhu, S. K. Ozdemir and L. Yang, "Oscillatory thermal dynamics in high-Q PDMS-coated silica toroidal microresonators," *Opt Express* **17**, 9571-9581 (2009).
- [58] T. J. Kippenberg, S. M. Spillane and K. J. Vahala, "Kerr-nonlinearity optical parametric oscillation in an ultrahigh-Q toroid microcavity," *Phys Rev Lett* **93**, 083904 (2004).
- [59] T. Carmon, L. Yang and K. J. Vahala, "Dynamical thermal behavior and thermal self-stability of microcavities," *Opt Express* **12**, 4742-4750 (2004).
- [60] M. Han and A. Wang, "Temperature compensation of optical microresonators using a surface layer with negative thermo-optic coefficient," *Opt Lett* **32**, 1800-1802 (2007).
- [61] J. D. Suter, I. M. White, H. Y. Zhu and X. D. Fan, "Thermal characterization of liquid core optical ring resonator sensors," *Appl Optics* **46**, 389-396 (2007).
- [62] D. B. Hall, P. Underhill and J. M. Torkelson, "Spin coating of thin and ultrathin polymer films," *Polym Eng Sci* **38**, 2039-2045 (1998).
- [63] H. W. Fang, K. Y. Li, T. L. Su, T. C. K. Yang, J. S. Chang, P. L. Lin and W. C. Chang, "Dip coating assisted polylactic acid deposition on steel surface: Film thickness affected by drag force and gravity," *Mater Lett* **62**, 3739-3741 (2008).

- [64] S. F. Burlatsky, G. Oshanin, A. M. Cazabat, M. Moreau and W. P. Reinhardt, "Spreading of a thin wetting film: Microscopic approach," *Phys Rev E* **54**, 3832-3845 (1996).
- [65] H. Y. Zhu, I. M. White, J. D. Suter, P. S. Dale and X. D. Fan, "Analysis of biomolecule detection with optofluidic ring resonator sensors," *Opt Express* **15**, 9139-9146 (2007).
- [66] M. Cai, O. Painter, K. J. Vahala and P. C. Sercel, "Fiber-coupled microsphere laser," *Opt Lett* **25**, 1430-1432 (2000).
- [67] F. Treussart, V. S. Ilchenko, J. F. Roch, J. Hare, V. Lefevre-Seguin, J. M. Raimond and S. Haroche, "Evidence for intrinsic Kerr bistability of high-Q microsphere resonators in superfluid helium," *Eur Phys J D* **1**, 235-238 (1998).
- [68] H. Rokhsari and K. J. Vahala, "Observation of Kerr nonlinearity in microcavities at room temperature," *Opt Lett* **30**, 427-429 (2005).
- [69] V. S. Ilchenko and M. L. Gorodetskii, "Thermal Nonlinear Effects in Optical Whispering Gallery Microresonators," *Laser Phys* **2**, 1004-1009 (1992).
- [70] A. E. Fomin, M. L. Gorodetsky, I. S. Grudinin and V. S. Ilchenko, "Nonstationary nonlinear effects in optical microspheres," *J Opt Soc Am B* **22**, 459-465 (2005).
- [71] C. Schmidt, A. Chipouline, T. Pertsch, A. Tunnermann, O. Egorov, F. Lederer and L. Deych, "Nonlinear thermal effects in optical microspheres at different wavelength sweeping speeds," *Opt Express* **16**, 6285-6301 (2008).
- [72] Y. S. Park and H. L. Wang, "Regenerative pulsation in silica microspheres," *Opt Lett* **32**, 3104-3106 (2007).
- [73] T. J. Johnson, M. Borselli and O. Painter, "Self-induced optical modulation of the transmission through a high-Q silicon microdisk resonator," *Opt Express* **14**, 817-831 (2006).
- [74] O. Gaathon, J. Culic-Viskota, M. Mihnev, I. Teraoka and S. Arnold, "Enhancing sensitivity of a whispering gallery mode biosensor by subwavelength confinement," *Appl Phys Lett* **89**, 223901 (2006).
- [75] C. Manolatou, M. J. Khan, S. H. Fan, P. R. Villeneuve, H. A. Haus and J. D. Joannopoulos, "Coupling of modes analysis of resonant channel add-drop filters," *Ieee J Quantum Elect* **35**, 1322-1331 (1999).

- [76] C. Y. Chao, W. Fung and L. J. Guo, "Polymer microring resonators for biochemical sensing applications," *Ieee J Sel Top Quant* **12**, 134-142 (2006).
- [77] I. Teraoka and S. Arnold, "Whispering-gallery modes in a microsphere coated with a high-refractive index layer: polarization-dependent sensitivity enhancement of the resonance-shift and TE-TM resonance matching," *J Opt Soc Am B* **24**, 653-659 (2007).
- [78] S. Schmid, S. Kuhne and C. Hierold, "Influence of air humidity on polymeric microresonators," *J Micromech Microeng* **19**, 065018 (2009).
- [79] T. Ling, S. L. Chen and L. J. Guo, "Fabrication and characterization of high Q polymer micro-ring resonator and its application as a sensitive ultrasonic detector," *Opt Express* **19**, 861-869 (2011).
- [80] T. Ioppolo, M. I. Kozhevnikov, V. Stepaniuk, M. V. Otugen and V. Sheverev, "Micro-optical force sensor concept based on whispering gallery mode resonators," *Appl Optics* **47**, 3009-3014 (2008).
- [81] Y. F. Xiao, L. He, J. Zhu and L. Yang, "Electromagnetically induced transparency-like effect in a single polydimethylsiloxane-coated silica microtoroid," *Appl Phys Lett* **94**, 231115 (2009).
- [82] T. H. Maiman, "Stimulated Optical Radiation in Ruby," *Nature* **187**, 493-494 (1960).
- [83] H. J. Kimble, "Strong interactions of single atoms and photons in cavity QED," *Phys Scripta* **T76**, 127-137 (1998).
- [84] S. K. Ozdemir, J. Zhu, L. He and L. Yang, "Estimation of Purcell factor from mode-splitting spectra in an optical microcavity," *Phys Rev A* **83**, 033817 (2011).
- [85] L. He, S. K. Ozdemir, J. Zhu and L. Yang, "Self-pulsation in fiber-coupled, on-chip microcavity lasers," *Opt Lett* **35**, 256-258 (2010).
- [86] V. Sandoghdar, F. Treussart, J. Hare, V. LefevreSeguin, J. M. Raimond and S. Haroche, "Very low threshold whispering-gallery-mode microsphere laser," *Phys Rev A* **54**, R1777-R1780 (1996).
- [87] S. I. Shopova, G. Farca, A. T. Rosenberger, W. M. S. Wickramanayake and N. A. Kotov, "Microsphere whispering-gallery-mode laser using HgTe quantum dots," *Appl Phys Lett* **85**, 6101-6103 (2004).
- [88] H. S. Rong, S. B. Xu, Y. H. Kuo, V. Sih, O. Cohen, O. Raday and M. Paniccia, "Low-threshold continuous-wave Raman silicon laser," *Nature Photon* **1**, 232-237 (2007).

- [89] S. M. Spillane, T. J. Kippenberg and K. J. Vahala, "Ultralow-threshold Raman laser using a spherical dielectric microcavity," *Nature* **415**, 621-623 (2002).
- [90] L. He, S. K. Ozdemir and L. Yang, "Whispering gallery microcavity lasers," *Laser & Photon. Rev.* (2012), DOI: 10.1002/lpor.201100032.
- [91] H. M. Tzeng, K. F. Wall, M. B. Long and R. K. Chang, "Laser emission from individual droplets at wavelengths corresponding to morphology-dependent resonances," *Opt Lett* **9**, 499-501 (1984).
- [92] M. Tanyeri, R. Perron and I. M. Kennedy, "Lasing droplets in a microfabricated channel," *Opt Lett* **32**, 2529-2531 (2007).
- [93] H. Cao, J. Y. Xu, W. H. Xiang, Y. Ma, S.-H. Chang, S. T. Ho and G. S. Solomon, "Optically pumped InAs quantum dot microdisk lasers," *Appl Phys Lett* **76**, 3519-3521 (2000).
- [94] T. Grossmann *et al.*, "Low-threshold conical microcavity dye lasers," *Appl Phys Lett* **97**, 063304 (2010).
- [95] E. Snitzer, "Glass Lasers," *Appl Opt* **5**, 1487-1499 (1966).
- [96] L. Yang and K. J. Vahala, "Gain functionalization of silica microresonators," *Opt Lett* **28**, 592-594 (2003).
- [97] J. Kalkman, A. Polman, T. J. Kippenberg, K. J. Vahala and M. L. Brongersma, "Erbium-implanted silica microsphere laser," *Nucl Instrum Meth B* **242**, 182-185 (2006).
- [98] R. Roy, "Ceramics by the Solution-Sol-Gel Route," *Science* **238**, 1664-1669 (1987).
- [99] L. L. Hench and J. K. West, "The Sol-Gel Process," *Chem Rev* **90**, 33-72 (1990).
- [100] L. Yang, T. Lu, T. Carmon, B. Min and K. J. Vahala, "A 4-Hz Fundamental Linewidth On-Chip Microlaser," *CLEO2007, CMR2* (2007).
- [101] F. Sanchez, P. Leboudec, P. L. Francois and G. Stephan, "Effects of ion pairs on the dynamics of erbium-doped fiber lasers," *Phys Rev A* **48**, 2220-2229 (1993).
- [102] F. Sanchez and G. Stephan, "General analysis of instabilities in erbium-doped fiber lasers," *Phys Rev E* **53**, 2110-2122 (1996).

- [103] E. Delevaque, T. Georges, M. Monerie, P. Lamouler and J. F. Bayon, "Modeling of Pair-Induced Quenching in Erbium-Doped Silicate Fibers," *Ieee Photonic Tech L* **5**, 73-75 (1993).
- [104] S. Colin, E. Contesse, P. LeBoudec, G. Stephan and F. Sanchez, "Evidence of a saturable-absorption effect in heavily erbium-doped fibers," *Opt Lett* **21**, 1987-1989 (1996).
- [105] L. He, S. K. Ozdemir, J. Zhu and L. Yang, "Ultrasensitive detection of mode splitting in active optical microcavities," *Phys Rev A* **82**, 053810 (2010).
- [106] A. Mazzei, S. Gotzinger, S. Menezes Lde, G. Zumofen, O. Benson and V. Sandoghdar, "Controlled coupling of counterpropagating whispering-gallery modes by a single Rayleigh scatterer: a classical problem in a quantum optical light," *Phys Rev Lett* **99**, 173603 (2007).
- [107] J. Zhu, S. K. Ozdemir, L. He, D. R. Chen and L. Yang, "Single virus and nanoparticle size spectrometry by whispering-gallery-mode microcavities," *Opt Express* **19**, 16195-16206 (2011).
- [108] T. J. Kippenberg, H. Rokhsari, T. Carmon, A. Scherer and K. J. Vahala, "Analysis of radiation-pressure induced mechanical oscillation of an optical microcavity," *Phys Rev Lett* **95**, 033901 (2005).
- [109] H. Rokhsari, T. J. Kippenberg, T. Carmon and K. J. Vahala, "Theoretical and experimental study of radiation pressure-induced mechanical oscillations (parametric instability) in optical microcavities," *Ieee J Sel Top Quant* **12**, 96-107 (2006).
- [110] A. E. Siegman, *Lasers*. University Science Books, Sausalito, CA, (1986).
- [111] B. Min, T. J. Kippenberg, L. Yang, K. J. Vahala, J. Kalkman and A. Polman, "Erbium-implanted high-Q silica toroidal microcavity laser on a silicon chip," *Phys Rev A* **70**, 033803 (2004).
- [112] W. Koechner, *Solid-state laser engineering*. Springer, New York, NY, 6th rev. and updated edn (2006).
- [113] A. Polman, B. Min, J. Kalkman, T. J. Kippenberg and K. J. Vahala, "Ultralow-threshold erbium-implanted toroidal microlaser on silicon," *Appl Phys Lett* **84**, 1037-1039 (2004).
- [114] Z. Y. Zhang, L. Yang, V. Liu, T. Hong, K. Vahala and A. Scherer, "Visible submicron microdisk lasers," *Appl Phys Lett* **90**, 111119 (2007).

- [115] Y. H. Chen, Y. K. Wu and L. J. Guo, "Photonic crystal microdisk lasers," *Appl Phys Lett* **98**, 131109 (2011).
- [116] M. P. Nezhad, A. Simic, O. Bondarenko, B. Slutsky, A. Mizrahi, L. A. Feng, V. Lomakin and Y. Fainman, "Room-temperature subwavelength metallo-dielectric lasers," *Nature Photon* **4**, 395-399 (2010).
- [117] M. W. Kim and P. C. Ku, "Semiconductor nanoring lasers," *Appl Phys Lett* **98**, 201105 (2011).
- [118] T. J. Whitley, C. A. Millar, R. Wyatt, M. C. Brierley and D. Szebesta, "Upconversion pumped green lasing in erbium doped fluorozirconate fibre," *Electron Lett* **27**, 1785-1786 (1991).
- [119] F. Song, G. Y. Zhang, M. R. Shang, H. Tan, J. Yang and F. Z. Meng, "Three-photon phenomena in the upconversion luminescence of erbium-ytterbium-codoped phosphate glass," *Appl Phys Lett* **79**, 1748-1750 (2001).
- [120] S. Arahira, K. Watanabe, K. Shinozaki and Y. Ogawa, "Successive excited-state absorption through a multistep process in highly Er^{3+} -doped fiber pumped by a 1.48-microm laser diode," *Opt Lett* **17**, 1679-1681 (1992).
- [121] J. Y. Allain, M. Monerie and H. Poignant, "Tunable green upconversion erbium fibre laser," *Electron Lett* **28**, 111-113 (1992).
- [122] T. Lu, L. Yang, R. V. A. van Loon, A. Polman and K. J. Vahala, "On-chip green silica upconversion microlaser," *Opt Lett* **34**, 482-484 (2009).
- [123] R. Paschotta, J. Nilsson, A. C. Tropper and D. C. Hanna, "Ytterbium-doped fiber amplifiers," *Ieee J Quantum Elect* **33**, 1049-1056 (1997).
- [124] R. Koch, W. A. Clarkson, D. C. Hanna, S. Jiang, M. J. Myers, D. Rhonehouse, S. J. Hamlin, U. Griebner and H. Schonngel, "Efficient room temperature cw Yb:glass laser pumped by a 946 nm Nd:YAG laser," *Opt Commun* **134**, 175-178 (1997).
- [125] E. P. Ostby, L. Yang and K. J. Vahalal, "Ultralow-threshold Yb^{3+} : SiO_2 glass laser fabricated by the sol-gel process," *Opt Lett* **32**, 2650-2652 (2007).
- [126] E. P. Ostby and K. J. Vahala, "Yb-doped glass microcavity laser operation in water," *Opt Lett* **34**, 1153-1155 (2009).
- [127] P. H. Hoet, I. Bruske-Hohlfeld and O. V. Salata, "Nanoparticles - known and unknown health risks," *J Nanobiotechnology* **2**, 12 (2004).

- [128] A. K. Naik, M. S. Hanay, W. K. Hiebert, X. L. Feng and M. L. Roukes, "Towards single-molecule nanomechanical mass spectrometry," *Nature Nanotech* **4**, 445-450 (2009).
- [129] S. P. Wang, X. N. Shan, U. Patel, X. P. Huang, J. Lu, J. H. Li and N. J. Tao, "Label-free imaging, detection, and mass measurement of single viruses by surface plasmon resonance," *P Natl Acad Sci USA* **107**, 16028-16032 (2010).
- [130] A. Mitra, B. Deutsch, F. Ignatovich, C. Dykes and L. Novotny, "Nano-optofluidic detection of single viruses and nanoparticles," *Acc Nano* **4**, 1305-1312 (2010).
- [131] F. Vollmer and S. Arnold, "Whispering-gallery-mode biosensing: label-free detection down to single molecules," *Nature Methods* **5**, 591-596 (2008).
- [132] S. I. Shopova, R. Rajmangal, Y. Nishida and S. Arnold, "Ultrasensitive nanoparticle detection using a portable whispering gallery mode biosensor driven by a periodically poled lithium-niobate frequency doubled distributed feedback laser," *Rev Sci Instrum* **81**, 103110 (2010).
- [133] L. He, S. K. Ozdemir, J. Zhu and L. Yang, "Scatterer induced mode splitting in poly(dimethylsiloxane) coated microresonators," *Appl Phys Lett* **96**, 221101 (2010).
- [134] D. S. Weiss, V. Sandoghdar, J. Hare, V. Lefevreseguin, J. M. Raimond and S. Haroche, "Splitting of High-Q Mie Modes Induced by Light Backscattering in Silica Microspheres," *Opt Lett* **20**, 1835-1837 (1995).
- [135] K. Srinivasan and O. Painter, "Mode coupling and cavity-quantum-dot interactions in a fiber-coupled microdisk cavity," *Phys Rev A* **75**, 023814 (2007).
- [136] T. J. Kippenberg, A. L. Tchebotareva, J. Kalkman, A. Polman and K. J. Vahala, "Purcell-factor-enhanced scattering from Si nanocrystals in an optical microcavity," *Phys Rev Lett* **103**, 027406 (2009).
- [137] J. Zhu, S. K. Ozdemir, L. He and L. Yang, "Controlled manipulation of mode splitting in an optical microcavity by two Rayleigh scatterers," *Opt Express* **18**, 23535-23543 (2010).
- [138] L. Chantada, N. I. Nikolaev, A. L. Ivanov, P. Borri and W. Langbein, "Optical resonances in microcylinders: response to perturbations for biosensing," *J Opt Soc Am B* **25**, 1312-1321 (2008).
- [139] X. Yi, Y.-F. Xiao, Y.-C. Liu, B.-B. Li, Y.-L. Chen, Y. Li and Q.-H. Gong, "Multiple-Rayleigh-scatterer-induced mode splitting in a high-Q whispering-gallery-mode microresonator," *Phys Rev A* **83**, 023803 (2011).

- [140] L. He, S. K. Ozdemir, Y.-F. Xiao and L. Yang, "Gain-Induced Evolution of Mode Splitting Spectra in a High-Q Active Microresonator," *Ieee J Quantum Elect* **46**, 1626-1633 (2010).
- [141] A. Yariv, "Universal relations for coupling of optical power between microresonators and dielectric waveguides," *Electron Lett* **36**, 321-322 (2000).
- [142] Y. Dumeige, S. Trebaol, L. Ghisa, T. K. N. Nguyen, H. Tavernier and P. Feron, "Determination of coupling regime of high-Q resonators and optical gain of highly selective amplifiers," *J Opt Soc Am B* **25**, 2073-2080 (2008).
- [143] R. J. C. Spreeuw, R. C. Neelen, N. J. Vandruten, E. R. Eliel and J. P. Woerdman, "Mode coupling in a He-Ne ring laser with backscattering," *Phys Rev A* **42**, 4315-4324 (1990).
- [144] R. C. Neelen, R. J. C. Spreeuw, E. R. Eliel and J. P. Woerdman, "Frequency splitting of the longitudinal modes of a ring dye laser due to backscattering," *J Opt Soc Am B* **8**, 959-969 (1991).
- [145] T. Lu, L. Yang, T. Carmon and B. Min, "A Narrow-Linewidth On-Chip Toroid Raman Laser," *Ieee J Quantum Elect* **47**, 320-326 (2011).
- [146] W. Kim, S. K. Ozdemir, J. Zhu, L. He and L. Yang, "Demonstration of mode splitting in an optical microcavity in aqueous environment," *Appl Phys Lett* **97**, 071111 (2010).
- [147] W. Kim, S. K. Ozdemir, J. G. Zhu and L. Yang, "Observation and characterization of mode splitting in microsphere resonators in aquatic environment," *Appl Phys Lett* **98**, 141106 (2011).
- [148] J. Felsenstein, "Confidence-Limits on Phylogenies - an Approach Using the Bootstrap," *Evolution* **39**, 783-791 (1985).
- [149] B. Efron and R. Tibshirani, "Bootstrap Methods for Standard Errors, Confidence Intervals, and Other Measures of Statistical Accuracy," *Statist. Sci.* **1**, 54-75 (1986).
- [150] A. L. Schawlow and C. H. Townes, "Infrared and Optical Masers," *Phys Rev* **112**, 1940-1949 (1958).
- [151] L. E. Richter, H. I. Mandelberg, M. S. Kruger and P. A. Mcgrath, "Linewidth Determination from Self-Heterodyne Measurements with Subcoherence Delay Times," *Ieee J Quantum Elect* **22**, 2070-2074 (1986).

- [152] S. I. Shopova, R. Rajmangal, S. Holler and S. Arnold, "Plasmonic enhancement of a whispering-gallery-mode biosensor for single nanoparticle detection," *Appl Phys Lett* **98**, 243104 (2011).
- [153] M. A. Santiago-Cordoba, S.V. Boriskina, F. Vollmer and M. C. Demirel, "Nanoparticle-based protein detection by optical shift of a resonant microcavity," *Appl Phys Lett* **99**, 073701 (2011).

Vita

Lina He

- Date of Birth** January 02, 1985
- Place of Birth** Yuncheng, Shanxi, P.R.China
- Degrees** Ph.D. Electrical Engineering,
Washington University in St. Louis, May 2012
M.S. Electronic Engineering,
Tsinghua University, Beijing ,China, July 2007
B.S. Electronic Engineering,
Tsinghua University, Beijing ,China, July 2005
- Professional Societies** Institute of Electrical and Electronics Engineers
Optical Society of America
American Physical Society
- Publications**
- [1] L. He, S. K. Ozdemir and L. Yang, "Whispering gallery microcavity lasers," *Laser & Photon. Rev.* (2012), DOI: 10.1002/lpor.201100032.
 - [2] L. He, S. K. Ozdemir, J. Zhu, W. Kim and L. Yang, "Detecting single viruses and nanoparticles using whispering gallery microlasers," *Nature Nanotech.* 6, 428-432 (2011).
 - [3] J. Zhu, S. K. Ozdemir, L. He and L. Yang, "Optothermal spectroscopy of whispering gallery microresonators," *Appl. Phys. Lett.* 99, 171101 (2011).
 - [4] S. K. Ozdemir, J. Zhu, L. He and L. Yang, "Estimation of Purcell factor from mode-splitting spectra in an optical microcavity," *Phys. Rev. A* 83, 033817 (2011).
 - [5] J. Zhu, S. K. Ozdemir, L. He, D.-R. Chen and L. Yang, "Single virus and nanoparticle size spectrometry by whispering-gallery-mode microcavities," *Opt. Express* 19, 16195-16206 (2011).
 - [6] L. He, S. K. Ozdemir, J. Zhu and L. Yang, "Ultrasensitive detection of mode splitting in active optical microcavities,"

- Phys. Rev. A* 82, 053810 (2010).
- [7] L. He, S. K. Ozdemir, Y.-F. Xiao and L. Yang, "Gain-Induced Evolution of Mode Splitting Spectra in a High-Q Active Microresonator," *IEEE J. Quantum Electron.* 46, 1626-1633 (2010).
 - [8] L. He, S. K. Ozdemir, J. Zhu and L. Yang, "Scatterer induced mode splitting in poly(dimethylsiloxane) coated microresonators," *Appl. Phys. Lett.* 96, 221101 (2010).
 - [9] L. He, S. K. Ozdemir, J. Zhu and L. Yang, "Self-pulsation in fiber-coupled, on-chip microcavity lasers," *Opt. Lett.* 35, 256-258 (2010).
 - [10] J. Zhu, S. K. Ozdemir, L. He and L. Yang, "Controlled manipulation of mode splitting in an optical microcavity by two Rayleigh scatterers," *Opt. Express* 18, 23535-23543 (2010).
 - [11] W. Kim, S. K. Ozdemir, J. Zhu, L. He and L. Yang, "Demonstration of mode splitting in an optical microcavity in aqueous environment," *Appl. Phys. Lett.* 97, 071111 (2010).
 - [12] J. Zhu, S. K. Ozdemir, Y.-F. Xiao, L. Li, L. He, D.-R. Chen and L. Yang, "On-chip single nanoparticle detection and sizing by mode splitting in an ultrahigh-Q microresonator," *Nature Photon.* 4, 46-49 (2010).
 - [13] L. He, Y.-F. Xiao, J. Zhu, S. K. Ozdemir and L. Yang, "Oscillatory thermal dynamics in high-Q PDMS-coated silica toroidal microresonators," *Opt. Express* 17, 9571-9581 (2009).
 - [14] Y.-F. Xiao, L. He, J. Zhu and L. Yang, "Electromagnetically induced transparency-like effect in a single polydimethylsiloxane-coated silica microtoroid," *Appl. Phys. Lett.* 94, 231115 (2009).
 - [15] C.-H. Dong, L. He, Y.-F. Xiao, V. R. Gaddam, S. K. Ozdemir, Z.-F. Han, G.-C. Guo and L. Yang, "Fabrication of high-Q polydimethylsiloxane optical microspheres for thermal sensing," *Appl. Phys. Lett.* 94, 231119 (2009).
 - [16] L. He, Y.-F. Xiao, C.-H. Dong, J. Zhu, V. Gaddam and L. Yang, "Compensation of thermal refraction effect in high-Q toroidal microresonator by polydimethylsiloxane coating," *Appl. Phys. Lett.* 93, 201102 (2008).

May 2012

WGM Microresonators for Lasing and Sensing,

He, Ph.D. 2012